Toward the geological significance of hydrated silica detected by near infrared spectroscopy on Mars based on terrestrial reference samples

M. Pineau, L. Le Deit, B. Chauviré, J. Carter, B. Rondeau, N. Mangold

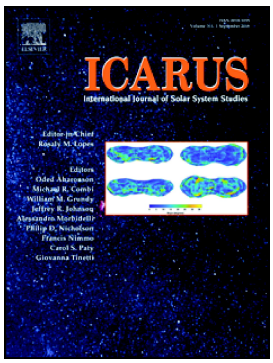

Toward the geological significance of hydrated silica detected by near infrared spectroscopy on Mars based on terrestrial reference samples

M. Pineau, L. Le Deit, B. Chauviré, J. Carter, B. Rondeau, N. Mangold

PII: S0019-1035(20)30097-X

DOI: https://doi.org/10.1016/j.icarus.2020.113706

Reference: YICAR 113706

To appear in: *Icarus*

Received date: 15 May 2019

Revised date: 7 February 2020

Accepted date: 14 February 2020

Please cite this article as: M. Pineau, L. Le Deit, B. Chauviré, et al., Toward the geological significance of hydrated silica detected by near infrared spectroscopy on Mars based on terrestrial reference samples, *Icarus*(2020), https://doi.org/10.1016/j.icarus.2020.113706

Toward the geological significance of hydrated silica detected by near infrared spectroscopy on Mars based on terrestrial reference samples

M. Pineau[a,]*, L. Le Deit[a], B. Chauviré[b], J. Carter[c], B. Rondeau[a] and N. Mangold[a]

[a] *Laboratoire de Planétologie et Géodynamique, CNRS UMR 6112, Université de Nantes, Université d'Angers, Nantes, France*

[b] *Univ. Grenoble Alpes, Univ. Savoie Mont Blanc, CNRS, IRD, IFSTTAR, ISTerre, Grenoble, France*

[c] *Institut d'Astrophysique Spatiale, CNRS UMR 8617, Université Paris-Sud, Orsay, France*

Declarations of interest: none

* Corresponding author. E-mail address: maxime.pineau@univ-nantes.fr

Keywords: Spectroscopy - Mars, Surface – Mineralogy – Geological Processes

Highlights

- Geological origin of hydrated silica on Mars is investigated.
- Spectral criteria developed on terrestrial silica minerals are applied to CRISM data.
- CRISM spectral results are consistent with the geomorphologic distinction between hydrated silica-bearing bedrock and aeolian deposits
- Discrimination between weathering and hydrothermal processes on Mars is discussed.

Abstract

Hydrated silica detected on the martian surface, from both orbital and *in-situ* data, is an indicator of past aqueous conditions. On Earth, several near infrared (NIR) spectral criteria can be used to discriminate silica phases (e.g. opal-A, opal-CT and chalcedony) and their formation processes. We have applied these spectral criteria to Compact Reconnaissance Imaging Spectrometer for Mars (CRISM) data in order to investigate the geological origin of hydrated silica on Mars. We used two spectral criteria: (i) the crystallinity spectral criteria on the 1.4- and 1.9 µm absorption bands to distinguish between amorphous (opal-A and hydrated glasses) and more crystalline (opal-CT and chalcedony) varieties of silica, and (ii) the Concavity-Ratio-Criterion (CRC) to differentiate opals of hydrothermal origin from weathering origin. We first adapted the CRC measurements on terrestrial samples to make them comparable to CRISM measurements on Mars: we resampled our terrestrial spectra down to the CRISM resolution, and tested the martian pressure effect on spectral signatures. Then, we selected several areas over nine sites where hydrated silica has been detected on Mars, on the basis of good quality detections. Our results show that two main types of spectra can be distinguished, and these are consistent with two distinct geomorphological contexts proposed by Sun and Milliken (2018): amorphous and/or dehydrated silica-bearing bedrock deposits, and more crystalline and/or hydrated silica-bearing aeolian deposits. The concavity criterion also indicates silica origins that are in agreement with most of the hypothesized geological origins proposed in the literature. Although these results need further strengthening,

they are promising for the use of NIR signatures as means of investigating the processes of hydrated silica on Mars.

1. Introduction

Over the last decade, orbital studies of the martian surface have shown abundant mineralogical evidence of water-rock interactions using the visible-near infrared spectrometers Observatoire pour la Minéralogie, l'Eau, et l'Activité (OMEGA, Mars Express) and Compact Reconnaissance Imaging Spectrometer for Mars (CRISM, Mars Reconnaissance Orbiter) (Bibring et al., 2005, 2006 ; Mustard et al., 2008; Murchie et al., 2009). The identified hydrated minerals consist mostly of Fe/Mg/Al-phyllosilicates, hydrated silica, sulfates, zeolites and fewer occurrences of chlorides and carbonates (e.g. Carter et al., 2013; Ehlmann and Edwards, 2014). These detections, associated with landforms indicating aqueous processes (e.g., fan-shaped deposits), are spread over geological units from different periods. This distribution of hydrated phases has led authors to specify a relative chronology of the various aqueous alteration phases present in the martian crust. Ferromagnesian phyllosilicates, characteristic of an intense aqueous alteration, are mostly observed in the heavily cratered Noachian units (older than -3.7 Gyr). The formation of these Fe/Mg clays could be associated either with hydrothermal processes (possibly maintained by major volcanic events or post-impact hydrothermal systems) or weathering processes at the surface (under a warmer and wetter climate than the present one; e.g. Ehlmann et al., 2011; Carter et al., 2013). Significant run-off produced the formation of valley networks that indicate large amounts of liquid water at the surface at this time (e.g. Sharp and Malin, 1975; Fassett and Head, 2008). Around 3.7 Gyr, the transition between Noachian and Hesperian periods is marked by a drastic climate change at the planetary scale. The Hesperian period shows a progressive evolution of the atmospheric conditions that became more and more arid and cold. This climatic upheaval implies that aqueous alteration occurred under drier and more acidic climatic conditions (e.g. Bibring et al., 2006). During this period, subsurface aqueous activity was mainly punctuated by diagenetic or hydrothermal episodes resulting from meteoritic impacts and/or volcanic activity (e.g. Mangold et al., 2012; Hauber et al., 2013). Hydrated Hesperian minerals detected from orbit are mainly sulfates, aluminous phyllosilicates and hydrated silica. This decreasing aqueous activity started in the Hesperian period and extended into all the Amazonian period that began ca. 3.2 Gyr ago. Subsequently, water-related processes are almost non-existent. Short-term aqueous processes such as outflow channels and only sporadic alteration events have led to the local formation of clays and sulfates (Mangold et al., 2010a; Weitz et al., 2011; Thollot et al., 2012; Milliken et al., 2014), or opaline silica associated with Fe/Mg-phyllosilicates, such as those observed on a few fresh alluvial fans (Carter et al., 2012; Hauber et al., 2013).

Although this chronology is widely presented in the literature, there are only a few constraints on the physico-chemical conditions of the climate prevailing during early Mars. In particular, relative contributions of hydrothermal alteration and surface weathering are still uncertain. Generally, the formation processes of the hydrated minerals are deduced from the geological context and mineral paragenesis, information that is not sufficient to consider precise conditions of formation. For example, in Nili Fossae and Mawrth Vallis, bottom-to-top stratigraphy of Fe/Mg-smectites, kaolinite, sulfates, and hydrated silica can be interpreted as extensive pedogenic profiles (Loizeau et al., 2007, 2012; McKeown et al., 2009; Gaudin et al., 2011; Carter et al., 2015). In this case, the bedrock that undergoes alteration can initially be poor in aluminum, and formation of Al-bearing phyllosilicates above Fe/Mg-clays is the result of an intense leaching of cations by the percolation of meteoric fluids through a mafic substrate. Such weathering profiles argue for an open system with atmosphere-surface interactions and thus, of a warmer and wetter climate in the martian past. Similar vertical mineralogical successions could also have formed by prolonged periods of superficial alteration under a less humid and moderate climate. On the other hand, other studies hypothesized that similar mineral types in other geological contexts can be the result of subsurface alteration (Mangold et al., 2007; Ehlmann et al., 2009, 2013). In that case, hydrothermal processes promoted by impacts and/or volcanic activity seem to be necessary and would not require the presence of an open system with surface-atmosphere interactions in the past. No interpretation on the past climate can be deciphered from the observation of mineral phases formed under these hydrothermal processes.

Several mineralogical species can form either at low temperature by surface weathering or at higher temperatures by hydrothermal alteration, and hydrated silica is one of them (Chauviré et al., 2017a and references therein). Previous studies showed that its near-infrared (NIR) signature could give important clues and information about its crystallinity (hydrated glass vs. opal-A vs. opal-CT/C vs. chalcedony) and hydration states (dehydrated vs. hydrated) (Langer and Florke, 1974; Rice et al., 2013; Sun, 2017; Sun and Milliken, 2018). In addition, experimental investigations on terrestrial samples suggest that hydrothermal processes may transform siloxane into silanol groups, which then changes the shape of its absorption bands (Boboň et al., 2011; Christy, 2011). Starting from this observation, Chauviré et al. (2017a) developed a spectral criterion, the Concavity-Ratio-Criterion (CRC), based on the NIR signature of hydrated silica distinguishing opals formed at low temperature by surface weathering from opals formed by hydrothermal activity at higher temperatures (> 50°C, Pirajno, 2009), regardless of their structure (opal-A or opal-CT). Moreover, one of the results from Rice et al. (2013) is that the ratio between the 2.2 and 1.9 µm band depths can be used to distinguish opal-A sinters formed under high-temperature from those formed at low-temperature.

Considering that opaline silica has been detected across several regions at the martian surface, in different geological contexts and in various geochronological units, we decided to investigate the NIR signature of hydrated silica on Mars. First, we carried out infrared analyses in reflectance on terrestrial samples of several types of hydrated silica with the specific spectral criterion developed by Chauviré et al. (2017a) on transmission measurements. This step was necessary to ensure the validity of the method for CRISM reflectance spectra interpretation. NIR spectral acquisitions of terrestrial hydrated silica were carried out at terrestrial ambient and at Mars-relevant atmospheric pressures to investigate the effect of the current martian atmospheric pressure on the spectral criteria. Second, we have investigated CRISM data, in the light of terrestrial results, in order to use spectral signatures for ascribing martian hydrated silica to surface weathering or hydrothermal activity. The final aim is to contribute to the reconstruction of past climate on Mars based on spectral interpretations of hydrated silica.

2. Background

We first present in Section 2.1 a description of the range of hydrated silica varieties and formation environments on Earth. This provides background for the hydrated silica occurrences on Mars that are summarized in Section 2.2. Sections 2.3 and 2.4 then present the NIR spectral signature of hydrated silica and the previous work done on it.

2.1. Hydrated silica: varieties and formations

The term “hydrated silica” includes a wide range of minerals, from amorphous (like opals and obsidian) to more crystalline species (chalcedony). Hydrated silica is a common product formed during the alteration of silicate that releases silica in the form of orthosilicic acid $Si(OH)_4$. Silica then polymerizes and precipitates by oversaturation induced by physico-chemical modifications in the released fluids. Hydrated silica may also form during the quenching of silicate liquid during volcanic processes, in the form of obsidian or volcanic glass (e.g. Friedman and Long, 1984). Volcanic hydrated glasses are mainly observed within volcaniclastic deposits or meteoritic impact complexes (e.g. Greshake et al., 2010; Kelloway et al., 2010; Giachetti et al., 2015).

Opals include different varieties of amorphous hydrated silica ($SiO_2.nH_2O$) with a water content that can reach up to ~ 15 wt.% (Langer and Flörke, 1974; Adams et al., 1991; Day and Jones, 2008; Thomas et al., 2013). Opals can be separated into two main groups according to their structure and crystallinity: opal-A (for amorphous) and opal-CT/C (for cristobalite and tridymite that are mixed within the amorphous structure) (Jones and Segnit, 1971). Hereafter, we will consider opal-C and opal-CT as a continuous series as shown by Elzea and Rice (1996), and use the general term opal-CT. Chalcedony is a crystalline silica variety composed of

quartz microfibers (Miehe et al., 1984; Flörke et al., 1991). Both opals and chalcedony can be found in various geological settings including deep-sea or lacustrine diatomaceous sediments (Murata and Randall, 1975; Hein et al., 1978; Stamatakis, 1989; Botz and Bohrmann, 1991; Elmas and Bentli, 2013), deep-sea hydrothermal vents (Lalou et al., 1984; Herzig et al., 1988; Bohrmann et al., 1998), hot-springs and geysers as silica sinters and geyserites (e.g. Guidry and Chafetz, 2003; Jones and Renaut, 2003; Goryniuk et al., 2004; Rodgers et al., 2004; Tobler et al., 2008), weathering profiles (Thiry and Millot, 1987; Thiry and Milnes, 1991; Thiry et al., 2006; Rondeau et al., 2012; Rey, 2013; Chauviré et al., 2017b, 2019), and volcanic rocks (e.g. Nagase and Akizuki, 1997; Banerjee and Wenzel, 1999). Amorphous silica has also been reported in fumarolic alteration context and volcanic exhalations environments where acid-sulfate leaching produces silica residue mixed with Fe-Ti coatings (Chemtob et al., 2010; Minitti et al., 2007; Seelos et al., 2010). Hallet (1975) and Rutledge et al. (2018) have also observed and described Si-rich rock coatings in proglacial environments. Interestingly, cryogenic opals that form at freezing temperatures have been reported in Yellowstone and Geysir hot-springs when the atmospheric temperatures are below 0°C (Channing and Butler, 2007; Jones and Renaut, 2010; Fox-powell et al., 2018).

Although opal and chalcedony are found in various geological settings, the geological process involved in their formation can be classified into three categories: surface weathering, hydrothermal alteration, and through biological precipitation by micro-organisms like diatoms, radiolaria or extremophile bacteria that collect silica dissolved in the water to develop various types of shell (e.g. Wetherbee et al., 2005); this biogenic origin is not considered in this work. The surface weathering (or pedogenesis) refers to all alteration processes taking place at the surface, or at shallow depth, at ambient temperatures (thus < 50°C, according to Pirajno, 2009). It is generally initiated by the presence of meteoric water, its percolation and its run-off. Conversely, hydrothermal alteration refers to fluids at higher temperatures than ambient temperature (> 50°C, according to Pirajno, 2009). Fluids may have an internal origin (magmatic or metamorphic) or an external origin (meteoric or seawater). Hydrothermal activity can occur at depth or at the surface, for which typical manifestations include geysers and hot-springs that produce silica sinter deposits and geyserites (e.g. Guidry and Chafetz, 2003; Jones and Renaut, 2003; Goryniuk et al., 2004; Rodgers et al., 2004; Tobler et al., 2008).

On Earth, hydrated silica can also undergo diagenetic transformations whereby opal-A can be converted into opal-CT, then to chalcedony or cryptocrystalline quartz, and eventually to microcrystalline quartz (e.g. Williams and Crerar, 1985). These transformations take place via dissolution-reprecipitation processes that can be promoted by circulation of fluids and heating (Kano, 1983; Williams and Crerar, 1985; Thiry and Millot, 1987; Jones and Renaut, 2007; Jones et al., 2007; Geilert et al., 2016). Because diagenetic transformations produce changes in the crystallinity of opal, it will affect its spectral signature (e.g. Boboň et al., 2011; Sun, 2017; Sun and

Milliken, 2018). It has been suggested that diagenesis could modify the spectral signature of hydrated silica and complicate the interpretation of the origin of the initial silica, but these effects on spectral criteria developed in order to determine the origin of the silica have not been verified (Chauviré et al., 2017a). On Mars, it has been estimated that amorphous silica, if in contact with water at ambient temperature (e.g. 0°C) could be completely transformed into quartz in 300 to 400 Myr (Tosca and Knoll, 2009).

2.2. Hydrated silica on Mars

Hydrated silica is a very common hydrated mineral on Mars as it has been detected at the surface in many locations, by both *in-situ* and orbital measurements. On the western rim of the Noachian-aged Endeavour crater, at Matijevic Hill, the Mars Exploration Rover *Opportunity* (MER-B) discovered minor amounts of silica (possibly hydrated) in mixture with Al-rich smectites at the outcrop named Esperance in a set of "boxwork" light-toned fractures. This occurrence of possible minor amounts of hydrated silica associated with Al-rich smectites (montmorillonite) suggests that some acidic diagenesis occurred at the Esperance outcrop (Arvidson et al., 2014; Clark et al., 2016). At Gusev crater, and more precisely at Home Plate, the Mars Exploration Rover *Spirit* (MER-A) detected strong signatures of SiO_2 within rocks and soils with SiO_2 contents up to 90 wt% (Squyres et al., 2008). Opaline silica, possibly occurring as sinter deposits, is the best matching phase for these materials that likely formed by hydrothermal activity (Squyres et al., 2008; Ruff et al., 2011). Recently, Ruff and Farmer (2016) suggested that sinters within the active hot spring field of El Tatio in Chile could be a good terrestrial analog for the silica deposits encountered by *Spirit* at Gusev crater. El Tatio sinters located in discharge channels with halite (NaCl) exhibit strong biosignatures of microstromatolites. These authors suggested that, because the silica deposits of Home Plate and El Tatio have similar structures and infrared spectra, it is possible that the Home Plate silica deposits could have formed by both abiotic and biotic processes. Within Gale crater, at Marias Pass (Murray Formation), the Mars Science Laboratory *Curiosity* rover has highlighted several enrichments of Si-rich materials. Detrital tridymite (a SiO_2 high-temperature and low-pressure polymorph) was detected in a sample of a laminated mudstone and ascribed to silicic volcanism origin (Morris et al., 2016). Located in the vicinity of this detrital silica enrichment, amorphous silica has been detected in fracture-associated halos crossing younger sandstone layers. This has been interpreted as diagenetic amorphous silica, indicative of late-stage groundwater activity at Gale crater (Frydenvang et al., 2017; Rapin et al., 2018).

From orbit, high-silica deposits have been detected by the Mars Global Surveyor's (MGS) Thermal Emission Spectrometer (TES) (Bandfield, 2008) and hydrated silica has been detected by the Mars Express' OMEGA and the Mars Reconnaissance Orbiter's (MRO) CRISM imaging spectrometers (Milliken et al., 2008).

Because it has been detected in various places all over the martian surface, hydrated silica appears to have been formed in various geological settings and throughout Mars' aqueous history, from the Noachian period until more recently during the Amazonian acidic period (e.g. Carter et al., 2013a; Ehlmann and Edwards, 2014). "Opaline silica" was first detected by CRISM on the plateaus surrounding Valles Marineris, in association with layered deposits dominated by hydrated sulfate signatures (Milliken et al., 2008). Following this detection, several authors studied the Valles Marineris' hydrated silica and showed that it is also associated with Al-phyllosilicates such as montmorillonite or kaolin-group minerals (e.g. Bishop et al., 2009; Weitz et al., 2010; Wendt et al., 2011; Le Deit et al., 2010). Many authors also reported detections of "opaline silica" in Mawrth Vallis in intimate mixtures with Al-phyllosilicates (e.g. Bishop et al., 2008; McKeown et al., 2009; Noe Dobrea et al., 2010; McKeown et al., 2011; Loizeau et al., 2012), in Toro crater with prehnite (Marzo et al., 2010), at Elorza crater (Quantin et al., 2012; Sun and Milliken, 2015, 2018; Hopkins et al., 2017), in many craters around the Antoniadi crater region with zeolites (e.g. Ehlmann et al., 2009; Smith and Bandfield, 2012), at the base of the Nili Tholus cone, in the Nili Patera caldera (Skok et al., 2010; Fawdon et al., 2015), in Noctis Labyrinthus with Al-phyllosilicates, Fe/Mg-smectites and sulfates (e.g. Thollot et al., 2012; Weitz et al., 2013), within Hellas Planitia (e.g. Bandfield et al., 2013), and in alluvial fans and fan deltas contexts (Carter et al., 2012; Hauber et al., 2013; Pan et al., 2019; Tarnas et al., 2019). Moreover, Sun and Milliken (2015) also reported detections of hydrated silica in several dozens of craters across Mars. All these detections have shown that hydrated silica could have formed in association with several mineral families: Fe/Mg-smectites (e.g. nontronite or saponite), Al-phyllosilicates (e.g. montmorillonite, kaolinite or halloysite), sulfates (like jarosite, gypsum, etc), zeolites (e.g. analcime or clinoptilolite) or with low-grade metamorphic minerals like prehnite and/or chlorite. These diverse observations in various settings (coatings, in layered deposits, in aeolian dunes, in distal parts of alluvial fan and fan delta, in sinter-like or fumarolic deposits, etc.) show that hydrated silica on Mars could potentially have formed in diverse geological conditions: acidic or alkaline, at low-temperature or high-temperature, in volcanic, hydrothermal, or sedimentary contexts.

2.3. Near-infrared spectra of hydrated silica

The NIR spectral signature of hydrated silica is dominated by water-related absorption bands. Water occurs in silica in the form of water molecules incorporated and trapped in the structure, and silanol groups Si-OH (hydroxyl groups bonded to silicon atoms). These two main species are present in hydrated silica in various configurations. Molecular water can be bonded to silanol groups and to itself thanks to hydrogen bonds, but it can also occur as free molecular water in non-bonded configurations. Likewise, silanol groups can be isolated (without hydrogen bonding), hydrogen-bonded with water molecules or with neighboring silanol groups. Silanol groups can be geminal (bonded to an adjacent silanol group sharing the same silicon atom) or vicinal (bonded to

an adjacent silanol group that is bonded to another silicon atom). All of these configurations of "water" contribute separately to the NIR signal of hydrated silica (Anderson and Wickersheim, 1964; Langer and Flörke, 1974; Christy, 2010, 2011).

Fundamental NIR absorptions of molecular water and silanol groups are found between 2.7 and 3.2 µm (~ 3200-3700 cm^{-1}) in the form of a broad and intense asymmetric absorption. Several contributions of each species and their configurations are difficult to decompose in this range making it challenging to use for the investigation of hydrated silica on both Mars and Earth. However, these absorptions have various harmonic and combination bands in the following locations (Jones and Segnit, 1969, 1971; Langer and Flörke, 1974; Graetsch et al., 1985; Figure 1; Table 1) :

- 1.4 µm (7000 cm^{-1}): it consists of an overtone of O-H stretching modes in both molecular water and silanol groups. It can be decomposed into two main contributions: at ~ 1.41 µm for O-H stretching in both isolated and bonded silanols and at ~ 1.46 µm for O-H stretching in bonded water molecules.
- 1.9 µm (5200 cm^{-1}): result of the combination of the different OH-modes (stretching and bending) in the molecular water. It can be decomposed into two main contributions: at ~ 1.91 µm for free molecular water and at ~ 1.96 µm for hydrogen-bonded molecular water.
- 2.2 µm (4500 cm^{-1}): combination of silanol groups (Si-OH) and siloxane vibrations (Si-O-Si). This absorption can be decomposed into two main contributions. The first contribution located at ~ 2.21 µm is attributed to free silanols, while the second one, located at ~ 2.26 µm is attributed to hydrogen-bonded silanols.

The two decompositions into two main contributions for the 2.2- and 1.9 µm absorption bands are equivalent to the types A and B first discussed by Langer and Flörke (1974).

Figure 1 (single column size). NIR reflectance spectra (continuum removed ; Section 3.5) of different terrestrial varieties of hydrated silica used in this work. Chosen examples: sample 1040 for weathering opal-A, sample 85.27 for hydrothermal opal-A, sample WT86 for weathering opal-CT, sample 24.349 for hydrothermal opal-CT, sample Gi526 for chalcedony, sample Obs_3 for obsidian and WD3 for volcanic glass. The main absorptions bands of hydrated silica are labeled as vertical lines with their causal molecules. More information on vibrational modes is given in Table 1.

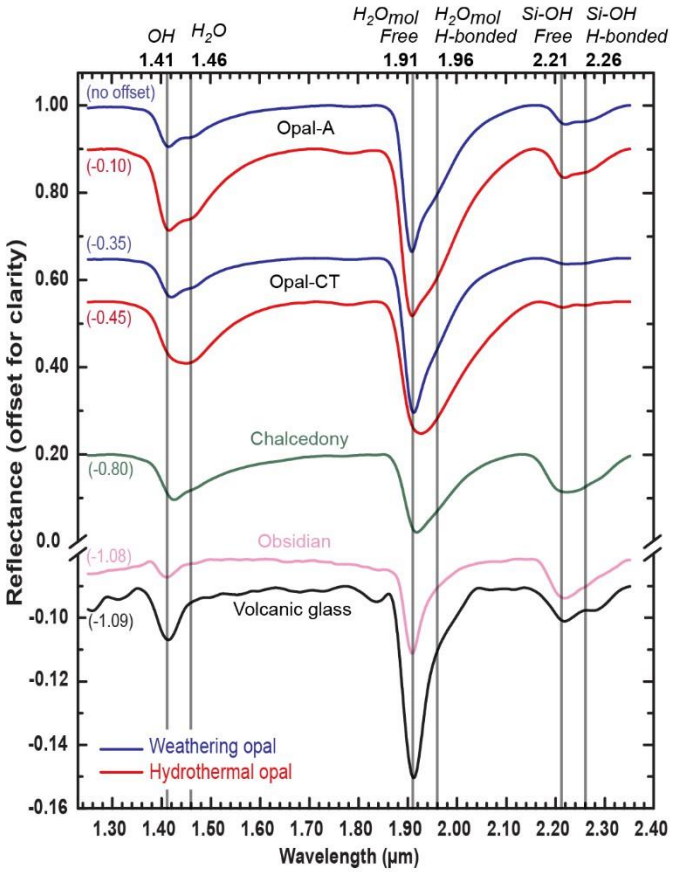

Table 1 (single column size). Main NIR absorption bands of molecular water (H_2O_{mol}), silanol complexes (Si-OH) and hydroxyl groups (OH) in amorphous hydrated silica (after Anderson and Wickersheim, 1964; Langer and Flörke, 1974; Graetsch et al., 1994; Christy, 2010, 2011; Boboň et al., 2011; Rice et al., 2013; Smith et al., 2013; Chauviré et al., 2017a). Vibration modes: δ = Si-OH bending in place; ν_{OH} = OH-stretching; ν_2 = symmetrical bending; ν_3 = anti-symmetrical stretching.

Band position in µm (*cm^{-1} equivalent*)	Band attribution	Vibration mode
1.38 *(7250 cm-1)*	OH (isolated, free of hydrogen bonding)	$2\nu_{OH}$
1.41 (*7090 cm^{-1}*)	OH (H-bonded)	$2\nu_{OH}$
1.46 (*6850 cm^{-1}*)	H_2O (H-bonded)	$2\nu_2 + \nu_3$
1.91 (*5250 cm^{-1}*)	H_2O_{mol} (isolated, free of hydrogen bonding)	$\nu_2 + \nu_3$
1.96 (*5100 cm^{-1}*)	H_2O_{mol} (H-bonded)	$\nu_2 + \nu_3$
2.21 (*4500 cm^{-1}*)	Si-OH (isolated, free of hydrogen bonding) + siloxane bending (Si-O-Si)	$\delta + \nu_{OH}$
2.26 (*4420 cm^{-1}*)	Si-OH (H-bonded) + siloxane bending (Si-O-Si)	$\delta + \nu_{OH}$

2.4. Overview of previous NIR studies of hydrated silica

Previous studies have shown that the NIR spectral signatures of hydrated silica are useful to characterize its structure and its geological origin. Langer and Florke (1974) have shown that the positions of the reflectance minima of the 1.4- and 1.9 µm absorption features may be used to distinguish opal-A from opal-CT (opal-CT having positions of their reflectance minima at longer wavelengths than opal-A). This has been subsequently confirmed by others (Rice et al., 2013; Chauviré et al., 2017a; Sun, 2017; Sun and Milliken, 2018). Rice et al. (2013)investigated NIR spectra of several hydrated silica-rich materials, including hydrated glasses, opals (mostly as geyserites and sinters) and chalcedony. They have shown that it is possible to discern between all of these hydrated minerals by using the position of the 1.4 µm minimum absorption band coupled with the symmetry of the 1.9 µm absorption band (ratio between the two constituting components). They also state that the ratio of the 2.2- and 1.9 µm band depths, coupled with the symmetry of the 1.4 µm absorption feature can be used to discern, although not unambiguously, opal-A and opal-CT. The structure, or crystallinity, of hydrated silica and/or opals plays an important role in the water incorporation and its speciation. Indeed, opal-CT would have more hydrogen-bonded (H-bonded) molecular water than opal-A because of its more crystalline structure (Langer and Flörke, 1974; Boboň et al., 2011; Chauviré et al., 2017a; Sun, 2017; Sun and Milliken, 2018).

The two spectral criteria (position of the 1.4 µm absorption band coupled with the symmetry of the 1.9 µm absorption feature), introduced by Rice et al. (2013), have been tested on CRISM data as "Crystallinity indices" by Smith et al. (2013) that they considered as a proxy of the amount of alteration that formed martian opaline silica. They observed that the most crystalline martian hydrated silica is co-located with ferromagnesian phyllosilicates (and zeolites), whereas moderate to low crystallinities are associated with Al-phyllosilicates and sulfates respectively. They interpreted this observation as evidence of aqueous activity decrease from Noachian to Hesperian, and to the Amazonian. Similarly, after investigations on terrestrial opal samples, Sun and Milliken (2018) used the position of the 1.4 µm minimum absorption band and the symmetry of the 2.2 µm absorption band to evaluate the hydration and maturity of hydrated silica. They applied these specific criteria to CRISM data and distinguished different geomorphological settings where opaline silica is detected: hydrated and/or crystalline silica in aeolian sediments and dehydrated and/or amorphous silica in bedrock exposures.

However, none of these studies has developed spectral criteria for the differentiation of opals formed at high temperature by hydrothermal activity from opals formed at low temperature by surface weathering. Chauviré et al. (2017a) observed that, regardless of their structure (opal-A or –CT), hydrothermal opals (high T) show more convex bands at 1.4 and 1.9 µm than weathering opals (low T). Based on this observation, they developed a band shape criterion adapted to the NIR spectral signature of opals to quantify the concavity of their absorption features. This spectral criterion, named the CRC for Concavity-Ratio-Criterion, was applied to the 1.4 and 1.9 µm bands on transmission spectra and allowed the differentiation of weathering opals from hydrothermal opals, irrespective of the structure. Based on Christy (2011) who demonstrated that a hydrothermal treatment of silica gel increased the proportion of silanol groups, they also proposed that hydrothermal alteration is a potential process to increase the relative proportions of bonded water, responsible for the 1.46 and 1.96 µm contributions, and then explained how hydrothermal opals show more convex bands than weathering opals.

Also, Rice et al. (2013) performed dehydration of an opal-A sinter under martian atmospheric pressure. Opal-A dehydration drastically changes its NIR spectral signature. For example, the minimum of the 1.4 µm band shifts towards shorter wavelengths, while the intensity of the 1.9 µm decreases, and the 2.2 µm absorption feature becomes predominant as molecular water is lost. This leads silanol groups to become more and more prevalent. Similar results have been obtained by Sun and Milliken (2018): spectral signatures of terrestrial opal spectra, measured in the laboratory at ambient temperature (25°C) and at Mars-relevant pressure/temperature/relative humidity conditions, were compared to CRISM spectra. Their results showed that hydrated silica samples dehydrate under martian atmospheric conditions. These spectral changes induced by the thin CO_2 atmosphere of Mars are important to keep in mind when investigating martian hydrated silica

as its spectral signature may not be the same as terrestrial opals because of post-depositional effects. All of these studies point to the fact that hydrated silica must be used with caution as an indicator of paleo-environments on Mars.

3. Material and methods

3.1. Terrestrial samples

The best analogs for the comparison between terrestrial samples and martian data would be natural, unprepared samples of various surface textures. However, we chose to investigate samples of polished thin sections of opal, in order to first characterize and understand the spectral features of hydrated silica independent of other factors. We investigated the influence of texture by comparing thin sections and powders for some samples.

This study is based on forty-five terrestrial samples (Table 2). Among them, thirty-four were selected among the thirty-eight used in Chauviré et al. (2017a), the four remaining being discarded because they showed mixing between several phases. We also used two additional geyserite opal-A samples (sample 85.27 from White Terrace, New Zealand) and opal-CT (sample 24.349 from Reykjanes, Iceland). Nine additional samples are volcanic glasses: Gi1900 and Obs_3 (Mexico), Obs_2 (Iceland), Obs_1 (unknown provenance), WD3 (dacitic glass, Milos, Greece), SO100-86DS and SO100-91DS and SO100-92DS (andesitic glasses from the Pacific-Antarctic Ridge, for more information see Maia et al., 2001 and Freund et al., 2013 studies) and Shosho (highly alkaline felsic glass of the shoshonitic series, Argentina; for more information on shoshonitic rock associations see Morrison, 1980 paper). Chemical analyses are available in Annex 1, for samples Obs_3, SO100-86DS, SO100-91DS, SO100-92DS, and Shosho.

As detailed in the next section, eight samples were selected for spectral measurement at Mars-relevant atmospheric pressure to investigate the potential dehydration of hydrated silica on Mars. The type of opal was determined using the position of the main silica Raman band at about ~ 325-370 cm^{-1} for opal-CT and about ~ 400-420 cm^{-1} for opal-A (Smallwood et al., 1997; Ostrooumov et al., 1999).

Thirty-three samples are of well-determined geological origin, either volcanic, hydrothermal, or continental weathering. The remaining twelve samples are of uncertain origin. They were kept in the sample set because three of them were used for the low-pressure experiments. All three chalcedony samples are of uncertain geologic origin, but are still of interest because chalcedony, or microcrystalline quartz, has been proposed to occur on Mars (Smith and Bandfield, 2012; Smith et al., 2013). These and the remaining six samples

of uncertain origin were kept in order to increase the number of measurements aimed at studying how crystallinity of the silica influences the spectral features.

Thirty samples were prepared as thin sections polished on both sides with a mean thickness ranging from ~ 150 to ~ 350 µm. Ten samples were prepared as powders crushed by hand using an agate mortar. Five samples were prepared as both a thin section and a powder in order to evaluate potential effects of the preparation type on the spectra.

Table 2 (double column size). Details of the terrestrial samples used in this study. For more information about suggested geological origins of the samples, the reader is referred to the paper of Chauviré et al. (2017a).

Geological origin	Silica variety	Geographic origin	Sample ID	Type of sample
Weathering (T < 50°C)	Opal-A	Coober Pedy (SA)	1040 [1,*]	Thin section + Powders
		Mintabie (SA)	1039 [1]	Thin section
			MTB01 [1]	Thin section
			MTB02 [1]	Thin section
	Opal-CT	Wegel Tena (ETH)	FT1111 [1,*]	Thin section
			VTB [1,*]	Thin section
			WT86 [1]	Thin section
			208 [1]	Thin section
Hydrothermal (T > 50-100°C)	Opal-A	White Terrace (NZ)	104.258 [1]	Thin section
			85.27	Powders
		Geysir (ICL)	46.170 [1]	Powders
	Opal-CT	Magdalena (MEX)	493 [1]	Thin section
		San Martin (MEX)	1543a [1]	Thin section
			1543b [1,*]	Thin section
			1543c [1]	Thin section
			1543d [1]	Thin section
		Guadalupa (MEX)	1552a [1]	Thin section
			1552b [1]	Thin section
			1552c [1]	Thin section
			1552d [1]	Thin section
		Mezezo (ETH)	521 [1]	Thin section
			1551 [1,*]	Thin section
			YM12 [1]	Thin section
		Reykjanes (ICL)	24.349	Powders
Volcanic (very-high temperature)	Obsidian	Mexico	Gi1900	Powders
			Obs_3	Powders
		Unknown	Obs_1	Thin section + Powders
		Iceland	Obs_2	Powders
	Glass	Milos (GRE)	WD3	Thin section
		Pacific-Antarctic Ridge	SO100-86DS [2]	Powders
			SO100-91DS [2]	Powders
			SO100-92DS [2]	Powders
		Argentina	Shosho	Powders
Uncertain or Unclear	Chalcedony	Agia-Marina (CYP)	Gi526 [1]	Thin section + Powders
		Unknown	1542 [1]	Thin section
		Mt Davies (USA)	1553 [1]	Thin section
	Opal-A	Honduras	785 [1,*]	Thin section + Powders
		Kashau (SLO)	86.2 [1,*]	Thin section
		Piaui (BRZ)	766 [1]	Thin section
		Brazil	BR08 [1]	Thin section

	Mali	928 [1]	Thin section
	Argentina	1085 [1]	Thin section + Powders
Opal-CT	Poland	Gi848 [1]	Thin section
	Peru	1547 [1]	Thin section
	Fougères (FR)	1548 [1,*]	Thin section

[1] for more information see Chauviré et al., 2017a

[2] for more information see Maia et al. (2001), Freund et al. (2013) and Annex 1

* samples used for FTIR measurements at Mars-relevant atmospheric pressure

3.2. Infrared acquisition

Reflectance NIR spectra were acquired using a Thermo-Nicolet FTIR 5700 spectrometer coupled with a Thermo-Nicolet Continuμm microscope at the Laboratoire de Planétologie et Géodynamique, in Nantes (France), using a halogen lamp as source, a CaF2 beam splitter and an InSb detector. Each spectrum was an accumulation of several hundreds of scans with a spectral resolution of ~ 0.02 to 1.0 nm (~ 0.00002 to 0.0010 μm; ~ 0.5 to 4 cm^{-1}) and a beam size of 300x300 μm. Reflectance infrared spectra were acquired in the ~ 1.0 to ~ 5.0 μm range (2100 to 10 000 cm^{-1}), but we will only focus on the ~ 1.1 - 2.6 μm NIR spectral range (~ 3800 to 9100 cm^{-1}).

For NIR measurements at Mars-relevant atmospheric pressure, the eight samples described above were placed into a vacuum cell (with sapphire windows) where the atmospheric pressure was lowered to a pressure ranging from 7.21 to 8.25 mbar, close to the average atmospheric pressure of the current martian surface (Haberle et al., 2017). For each sample, NIR spectra were acquired using a Brucker Vertex 70 coupled with a Hyperion 3000 microscope at the Institut de Planétologie et d'Astrophysique de Grenoble (France), with a InGaAs detector, a Si/Ca beam splitter and a standard halogen NIR source. Each spectrum consists of hundred scans with a spectral resolution of ~ 2.0 nm (~ 0.002 μm; ~ 4 cm^{-1}) and a beam size of 300x300 μm. Acquisitions were first made at ambient atmospheric conditions lasting a few minutes. Then, the air was pumped to reach an atmospheric pressure of about 7.25 mbar. Spectral acquisitions lasted three to fifteen hours. We did not sustain the low pressure over time in cases where the sample did not show any spectral evolution after three hours because reacting-samples showed dehydration immediately after low pressure applied. Spectrum acquisition was set up every two to ten minutes to monitor spectral evolutions.

In order to enable comparison of our data with CRISM spectra, all NIR spectra of terrestrial hydrated silica samples were resampled at the CRISM spectral resolution of about 6.55 nm (0.00655 µm; ~ 15 cm^{-1}) in the 1.1-2.6 µm spectral range using the "Spectral Resampling" tool in the ENVI® image analysis software.

Raman spectra were acquired using a Bruker Fourier Transform Raman spectrometer using a 1064 nm Nd-YAG laser excitation to avoid fluorescence, with a power of 1 W, and a LN-Ge diode as detector. Each measured spectrum is an accumulation of scans with a resolution of ~ 4 cm^{-1}.

3.3. CRISM cubes parameters and processing

CRISM is a hyperspectral imaging spectrometer that operates in the visible to near-infrared ranging from 0.36 to 3.92 µm using 544 spectral channels (spectels) with a spectral resolution of ~ 6.55 nm (Murchie et al., 2007, 2009). We used CRISM hyperspectral data in the targeted mode that are of two types: Full Resolution Targeted (FRT, with a spatial resolution of ~ 18 m/pixel) and Half Resolution Targeted (HRL, with a spatial resolution of ~ 36 m/pixel and a spatial coverage two times larger than the FRT images) (Murchie et al., 2007, 2009). CRISM data cubes used in this study were derived from the TRR3 calibration version in which destriping and denoising processes over the previous TRR2 products were performed (Seelos et al., 2011). "I/F" CRISM data available on the Planetary Data System (PDS) node calibrated in radiance and divided by a solar radiance spectrum are converted to surface reflectance by processing photometric effects and atmospheric gas absorptions. Atmospheric contributions, mostly affected by the CO_2-dominated martian atmosphere in the 1.4-2.8 µm range, are removed using the empirical volcano-scan algorithm method provided by McGuire et al. (2009).

For this study, we focused on the NIR range of the CRISM spectra between 1.1 and 2.6 µm where the most diagnostic absorption features of hydrated minerals, such as hydrated silica, are observed. These absorption features are due to water trapped in the mineral structure. They include a combination of fundamental bending and stretching vibrations of H_2O and OH, overtones of structural OH stretching vibrations, and several vibrations between different cations bonded to hydroxyl groups (e.g. Si-OH, Al-OH, Fe-OH, S-OH etc.) (e.g. Hunt and Salisbury, 1970; Hunt, 1977).

Detection and extraction of hydrated silica-like spectra were processed by the automated pipelines and algorithms described in Carter et al. (2013b) where hydrated signatures are highlighted by subtracting a mean neutral spectral contribution to hydrous mineral exposures over each observation (with such algorithms of extraction, spectrally neutral mineralogy produces flat reflectance spectra close to a value of zero). This method of detection and extraction of hydrous mineral spectra has the advantage of not including arbitrary ratios of spectra of interest by spectra of neutral mineralogy, a process generally carried out by the user, and so, in an

arbitrary manner. After spatial detection and localization of hydrated silica exposures by adapted spectral parameters related to specific absorption features (Carter et al., 2013b), we calculated averaged spectra of regions of interest encompassing as many pixels as possible (up to several tens) to reduce the stochastic noise in the resulting spectra.

In order to understand the geomorphologic context where martian hydrated silica is present and the variety of silica, spectral parameters that allow us to detect hydrated silica exposures were mapped, ortho-rectified and combined with High Resolution Imaging Science Experiment (HiRISE) and Context Camera (CTX) images in the ESRI-GIS software ArcGIS®. Both HiRISE and CTX are imaging cameras onboard MRO. CTX images have a spatial resolution of about ~ 5-6 m/pixel and provide a nearly full coverage of the CRISM hyperspectral data images (Malin et al., 2007). We used two types of HiRISE products: RED (monochromatic) and IRB (false color RGB using near infrared - 0.80 to 1.00 µm – red - 0.57 to 0.83 µm - and blue-green - 0.40 to 0.60 µm) images that both have high spatial resolution up to ~ 30 cm/pixel. IRB images are helpful to qualitatively estimate the grain size and cohesion of the materials at the surface, but they cover a smaller surface area than the HiRISE RED images. In IRB images, dusty surfaces generally appear in yellowish or reddish hues; materials with a larger grain size appear in a dark blue color; and whereas lithified bedrock exposures appear in light blue or turquoise colors (McEwen et al., 2007).

3.4. Selection of martian sites

We selected several martian sites where hydrated silica is detected (Figure 2) (Table 3). The selection of these sites was constrained by the quality of CRISM spectral cubes and with the occurrence of “spectrally pure” hydrated silica from previously reported silica-bearing locations on Mars in the literature. Each detection was manually inspected before being retained in the database. Systematically, the quality of the CO_2 atmospheric correction from McGuire et al., (2009) was inspected in a detailed and careful way. The atmospheric CO_2 has three major absorptions in the 1.9-2.1 µm wavelength region: at 1.96, 2.01 and 2.06 µm (e.g. Courtoy, 1957; Buback et al., 2015). For each spectrum, if the absorption located at 2.01 µm (which is the most intense for gaseous CO_2) is dominant, the 1.96 µm absorption of the atmospheric CO_2 was then assumed to be dominant over the 1.96 µm absorption of hydrated silica; thus the spectrum was rejected from the 1.9 µm absorption band spectral criteria calculations.

Finally, each detection was categorized according to the geomorphological context where it is located: alluvial fan and/or fan delta (Figure 3), aeolian deposits in impact craters (like aeolian dunes or megaripples around central peaks) (Figure 4), light-toned outcrop deposits within the Nili Patera volcanic caldera (Figure 5), and undifferentiated bedrock deposits (including various bedrocks in impact craters, plateau deposits, or

indurated deposits without specific morphologies) (Figure 6). Some spectra are plotted as examples in Figure 7 for each region in accordance with their geomorphologic context.

Figure 2 (single column size). Location of the martian sites selected for this study. CRISM cubes used for each site are listed in Table 3.

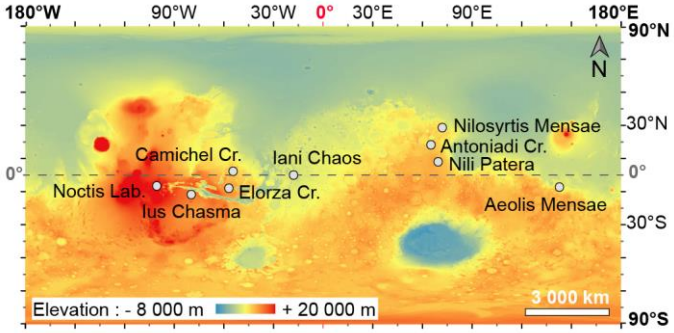

Table 3 (double column size). Details of martian hydrated silica detections.

Region	ID CRISM	CRISM Center Lat/Long	ROI n°	ROI locations (north pointing down)	Geomorphological context
Aeolis Mensae	HRL_C549	-6.53°N, 141.18°E	1	X = 280 ; Y = 302	Alluvial and/or fan delta deposits
			2	X = 290 ; Y = 292	Alluvial and/or fan delta deposits
			3	X = 297 ; Y = 285	Alluvial and/or fan delta deposits
	FRT_86B7	-12.74° N, 157.54°E	1 [a]	X = 164 ; Y = 238	Alluvial and/or fan delta deposits
			2 [b]	X = 138 ; Y = 263	Alluvial and/or fan delta deposits
			3 [c]	X = 128 ; Y = 289	Alluvial and/or fan delta deposits
			4	X = 240 ; Y = 439	Undifferentiated bedrock
Camichel crater	HRL_985E	2.71°N, -51.66°E	1	X = 66 ; Y = 60	Alluvial and/or fan delta deposits
			2	X = 57 ; Y = 82	Alluvial and/or fan delta deposits
			3	X = 60 ; Y = 152	Alluvial and/or fan delta deposits
			4	X = 55 ; Y = 175	Alluvial and/or fan delta deposits
			5	X = 48 ; Y = 205	Alluvial and/or fan delta deposits
Ius Chasma	HRL_7F68	-10.84°N, -78.25°E	1	X = 49 ; Y = 139	Undifferentiated bedrock
			2	X = 90 ; Y = 166	Undifferentiated bedrock
			3	X = 109 ; Y = 239	Undifferentiated bedrock
			4	X = 113 ; Y = 262	Undifferentiated bedrock
	HRL_44AC	-11.09°N, -78.01°E	1	X = 213 ; Y = 113	Undifferentiated bedrock
			2	X = 417 ; Y = 26	Undifferentiated bedrock
			3	X = 220 ; Y = 254	Undifferentiated bedrock
			4	X = 320 ; Y = 118	Undifferentiated bedrock
Nilosyrtis Mensae	FRT_D452	27.82°N, 46.55°E	1 [d]	X = 203 ; Y = 36	Undifferentiated bedrock
			2	X = 187; Y = 32	Undifferentiated bedrock
			3	X = 172 ; Y = 49	Undifferentiated bedrock
Antoniadi crater	FRT_A2B3	18.50°N, 65.07°E	1	X = 120 ; Y = 24	Intra-crater aeolian materials
			2	X = 362 ; Y = 50	Intra-crater aeolian materials
			3	X = 415 ; Y = 89	Intra-crater aeolian materials
	FRT_7CBB	20.43°N, 62.99°E	1	X = 374 ; Y = 541	Intra-crater aeolian materials
			2	X = 377 ; Y = 441	Intra-crater aeolian materials
			3	X = 370 ; Y = 485	Intra-crater aeolian materials
	FRT_9BCE	18.52°N, 65.14°E	1	X = 103 ; Y = 58	Intra-crater aeolian materials
			2	X = 127 ; Y = 76	Intra-crater aeolian materials
			3	X = 462 ; Y = 144	Intra-crater aeolian materials
	FRT_9312	19.92°N, 65.86°E	1	X = 140 ; Y = 36	Intra-crater aeolian materials
			2	X = 415 ; Y = 125	Intra-crater aeolian materials
			3	X = 213 ; Y = 480	Intra-crater aeolian materials
			4	X = 157 ; Y = 497	Intra-crater aeolian materials
			5	X = 121 ; Y = 517	Intra-crater aeolian materials
			6	X = 103 ; Y = 361	Intra-crater aeolian materials
			7	X = 46 ; Y = 465	Intra-crater aeolian materials
Elorza crater	FRT_8236	-8.75°N, -55.21°E	1	X = 21 ; Y = 255	Intra-crater aeolian materials
			2	X = 72 ; Y = 223	Intra-crater aeolian materials
			3	X = 44 ; Y = 141	Intra-crater aeolian materials
			4	X = 43 ; Y = 79	Intra-crater aeolian materials
			5	X = 161 ; Y = 37	Undifferentiated bedrock
			6	X = 204 ; Y = 313	Intra-crater aeolian materials
Nili Patera	FRT_10628	9.17°N, 67.35°E	1	X = 51 ; Y = 320	Intra-caldera light-toned deposits
			2	X = 69 ; Y = 271	Intra-caldera light-toned deposits
			3	X = 131 ; Y = 160	Intra-caldera light-toned deposits

			4	X = 80 ; Y = 117	Intra-caldera light-toned deposits
	FRT_4185	8.75°N, 67.34°E	1	X = 124 ; Y = 335	Intra-caldera light-toned deposits
			2	X = 131 ; Y = 406	Intra-caldera light-toned deposits
			3	X = 162 ; Y = 503	Intra-caldera light-toned deposits
	FRT_82EE	8.91°N, 67.28°E	1	X = 331 ; Y = 133	Intra-caldera light-toned deposits
			2	X = 359 ; Y = 226	Intra-caldera light-toned deposits
			3	X = 368 ; Y = 224	Intra-caldera light-toned deposits
			4	X = 379 ; Y = 239	Intra-caldera light-toned deposits
Noctis Labyrinthus	FRT_96EE	-10.44°N, -98.45°E	1	X = 142 ; Y = 129	Undifferentiated bedrock
			2	X = 143 ; Y = 101	Undifferentiated bedrock
			3	X = 171 ; Y = 72	Undifferentiated bedrock
			4	X = 196 ; Y = 66	Undifferentiated bedrock
			5	X = 269 ; Y = 62	Undifferentiated bedrock
			6	X = 335 ; Y = 156	Undifferentiated bedrock
			7	X = 362 ; Y = 220	Undifferentiated bedrock
	FRT_7E28	-7.16°N, -99.11°N	1	X = 53 ; Y = 565	Undifferentiated bedrock
			2	X = 71 ; Y = 581	Undifferentiated bedrock
			3	X = 72 ; Y = 567	Undifferentiated bedrock
			4	X = 38 ; Y = 535	Undifferentiated bedrock
Iani Chaos	FRT_134D2	-0.61°N, -18.03°E	1	X = 91 ; Y = 135	Intra-crater aeolian materials
			2	X = 180 ; Y = 221	Intra-crater aeolian materials
			3	X = 247 ; Y = 161	Intra-crater aeolian materials
			4	X = 233 ; Y = 14	Intra-crater aeolian materials

For the following spectra, several spectels in the 2.2 µm absorption band were subject to spectral artifacts. These spectels were deleted and then re-interpolated using spline-cubic interpolation on several points:

[a] for this spectrum (Aeolis Mensae, FRT_86B7, first spectrum), seven spectels were deleted (at 2.1855, 2.1922, 2.1988, 2.2054, 2.2120, 2.2186 and 2.2252 µm) and were re-interpolated on the Origin software using a spline-cubic interpolation on seven points.

[b] for this spectrum (Aeolis Mensae, FRT_86B7, second spectrum), six spectels were deleted (at 2.1855, 2.1922, 2.1988, 2.2054, 2.2120 and 2.2186 µm) and were re-interpolated on the Origin software using a spline-cubic interpolation on six points.

[c] for this spectrum (Aeolis Mensae, FRT_86B7, third spectrum), five spectels were deleted (at 2.1922, 2.1988, 2.2054, 2.2120 and 2.2186 µm) and were re-interpolated on the Origin software using a spline-cubic interpolation on five points.

[d] for this spectrum (Nilosyrtis Mensae, FRT_D452, first spectrum), five spectels were deleted (at 2.1922, 2.1988, 2.2054, 2.2120 and 2.2186 µm) and were re-interpolated on the Origin software using a spline-cubic interpolation on five points.

At the Aeolis Mensae and Camichel crater sites, hydrated silica detections are localized within deposits that appear to be generally lighter and to have a smoother texture than the surrounding bedrock (Figure 3). In some places, hydrated silica-bearing deposits exhibit stratified layers. They are mainly detected within the distal parts of intra-crater fan delta or alluvial fans, but can also cover almost the entire geomorphologic features (Carter et al., 2012; Hauber et al., 2013). These detections are then categorized as “alluvial fan and/or fan delta deposits”.

Figure 3 (double column size). Geomorphology of hydrated silica-bearing alluvial fans and/or fan delta. Hydrated silica exposures are mapped in cyan color in the top images (a,c,e). The white circles indicate the regions of interest from which the spectra of hydrated silica were extracted (first number is the number of the ROI and second is the CRISM cube ID) **a.** Portion of CTX image P22_009729_1735_XI_06S218W in Aeolis Mensae (CRISM observation HRL0000C549). **b.** CTX image P22_009729_1735_XI_06S218W close-up view of the hydrated silica-bearing materials. **c.** Portion of HiRISE RED image ESP_014159_1670 in Aeolis Mensae (CRISM observation FRT000086B7). **d.** HiRISE RED image ESP_014159_1670 close-up view of the hydrated silica-bearing materials. **e.** Portion of CTX image P06_003539_1825_XI_02N051W in Camichel crater (CRISM observation HRL0000985E). **f.** HiRISE RED and COLOR images PSP_007732_1825 close-up of the hydrated silica-bearing materials.

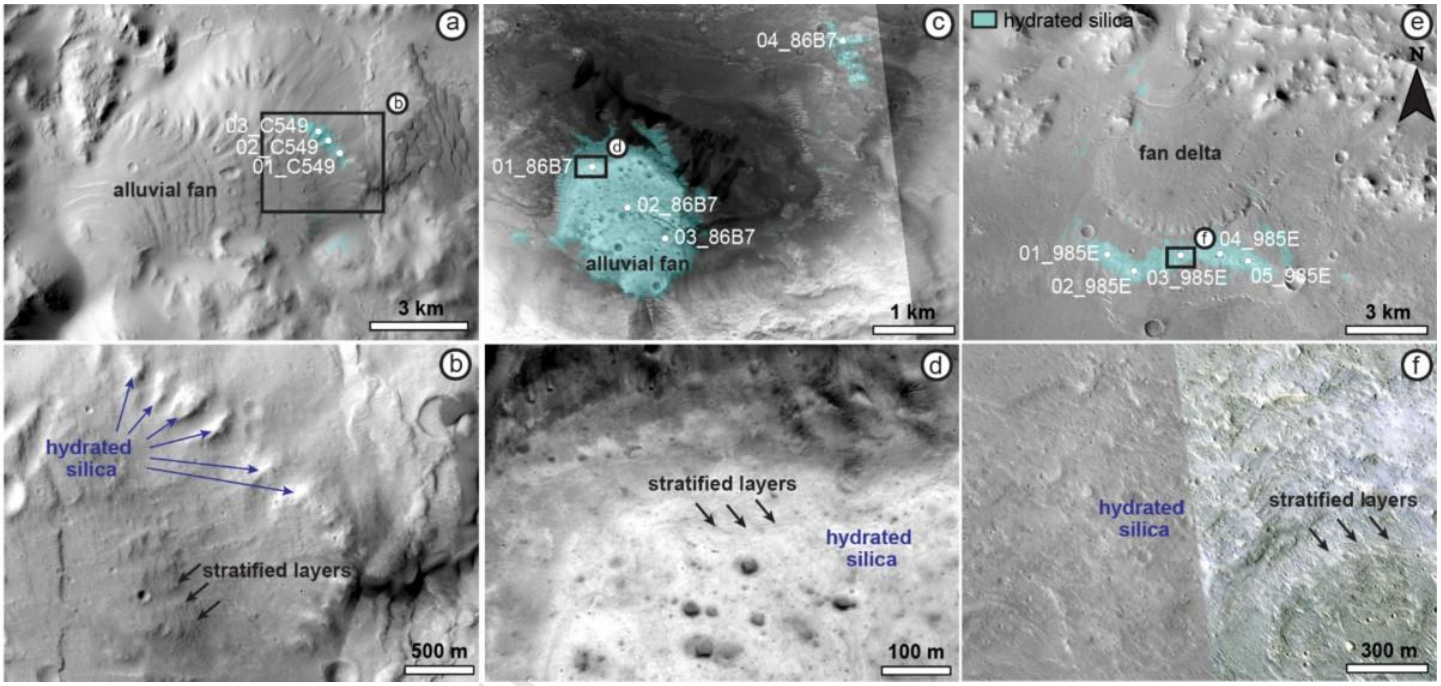

South of the Antoniadi crater area, many exposures of hydrated silica are detected within widespread light-toned aeolian megaripples and dune fields, localized around central peaks of impact craters (Ehlmann et al., 2009; Smith and Bandfield, 2012) (Figure 4a,b). In the Elorza crater central uplift, hydrated silica is detected in light-toned aeolian deposits and/or poorly indurated materials (Quantin et al., 2012; Sun and Milliken, 2015, 2018; Hopkins et al., 2017) (Figure 4c,d,e,f). The Iani Chaos site in the Margaritifer Terra region has hydrated silica within light-toned aeolian dunes around the central peak of an impact crater (Thomas et al., 2017) (Figure 4g,h). These detections all indicate hydrated silica in aeolian dune fields or poorly indurated materials localized around central peaks of impacts craters. Thus, we categorize them as “intra-crater aeolian deposits”.

Figure 4 (double column size). Geomorphology of hydrated silica-bearing aeolian deposits. Hydrated silica exposures are mapped in cyan color in the top images (a,c,g). The white circles indicate the regions of interest from which the spectra of hydrated silica were extracted (first number is the number of the ROI and second is the CRISM cube ID) **a.** Portion of CTX image P07_003706_2000_XI_20N294W in Antoniadi crater (CRISM observation FRT00009312). **b.** HiRISE RED and COLOR images PSP_003205_2000 close-up of the hydrated silica-bearing materials. **c.** Portion of CTX image P12_005649_1696_XI_10S055W in Elorza crater (CRISM observation FRT00008236). **d.** HiRISE COLOR image ESP_025652_1710 close-up of the hydrated silica-bearing materials. **e.** Portion of HiRISE COLOR image ESP_045643_1710 close up of the hydrated silica-bearing materials. **f.** HiRISE RED image ESP_021551_1710 close-up of the hydrated silica-bearing materials. **g.** Portion of CTX image P02_001995_1794_XN_00S018W in Iani Chaos (CRISM observation FRT000134D2). **h.** HiRISE RED and COLOR images SP_022710_1795 close up of the hydrated silica-bearing materials.

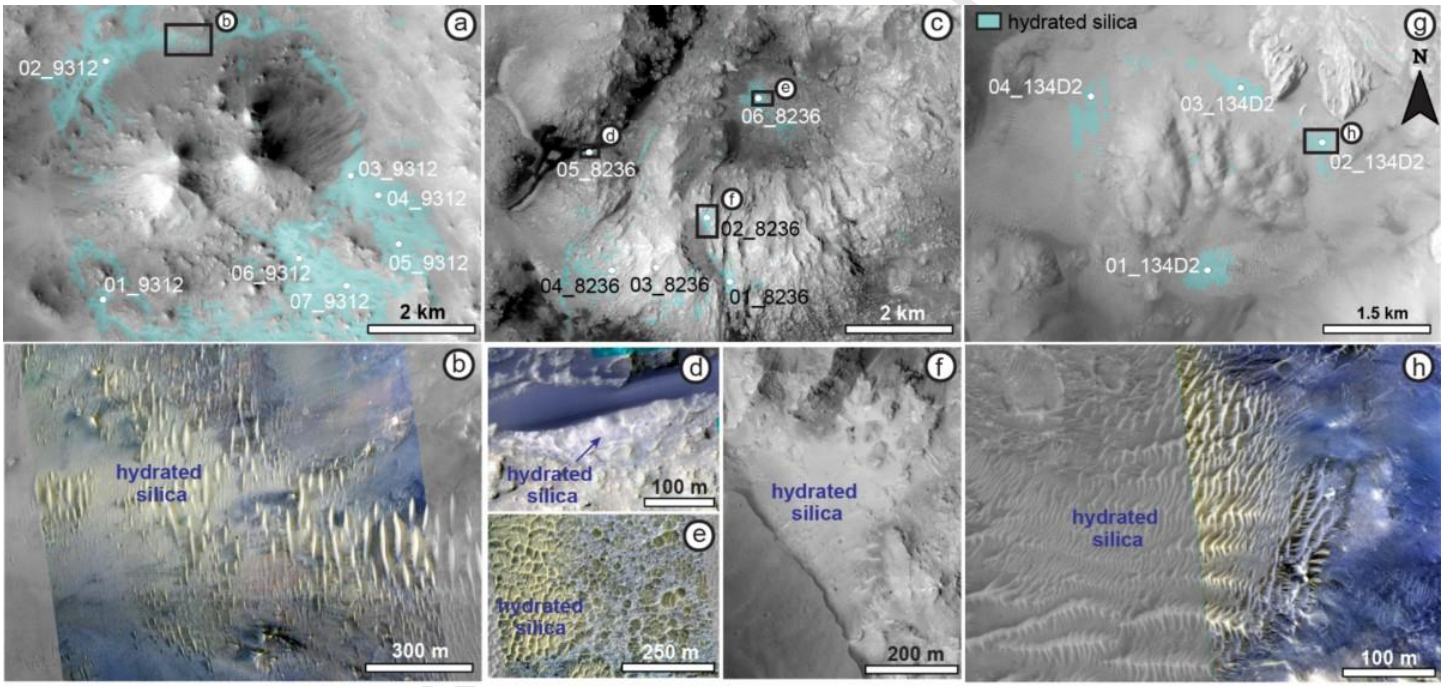

In the Nili Patera caldera, hydrated silica is detected within semi-circular light-toned mound outcrop deposits, that are localized immediately around the Nili Tholus cone, in two locations southwest of the volcanic cone and within a field of dark-toned mafic dunes where light-toned mound outcrop deposits exhibiting hydrated silica signatures are also present (Skok et al., 2010; Wray et al., 2013; Sun et al., 2016; Sun and Milliken, 2018) (Figure 5). The hydrated silica occurrences of Sun et al. (2016) and Sun and Milliken (2018) were not included in the dataset because of the restricted spatial distribution that did not permit us to extract enough pixels to get spectra of sufficient quality. These detections are categorized as “intra-caldera light-toned deposits”.

Figure 5 (double column size). Geomorphology of hydrated silica-bearing light-toned deposits in Nili Patera. Hydrated silica exposures are mapped in cyan color in the top CRISM images (a,c,e). The white circles indicate the regions of interest from which the spectra of hydrated silica were extracted (first number is the number of the ROI and second is the CRISM cube ID) **a.** Portion of CTX image B05_011459_1891_XI_09N292W around Nili Tholus (CRISM observation FRT00010628). **b.** HiRISE COLOR image ESP_020940_1895 close-up of the hydrated silica-bearing materials. **c.** Portion of CTX image P18_008255_1888_XN_08N292W (CRISM observation FRT000082EE). **d.** HiRISE RED image PSP_005684_1890 close-up of the hydrated silica-bearing materials. **e.** Portion of CTX image P18_008255_1888_XN_08N292W (CRISM observation FRT00004185). **f.** HiRISE COLOR image ESP_030843_1890 close-up of the hydrated silica-bearing materials.

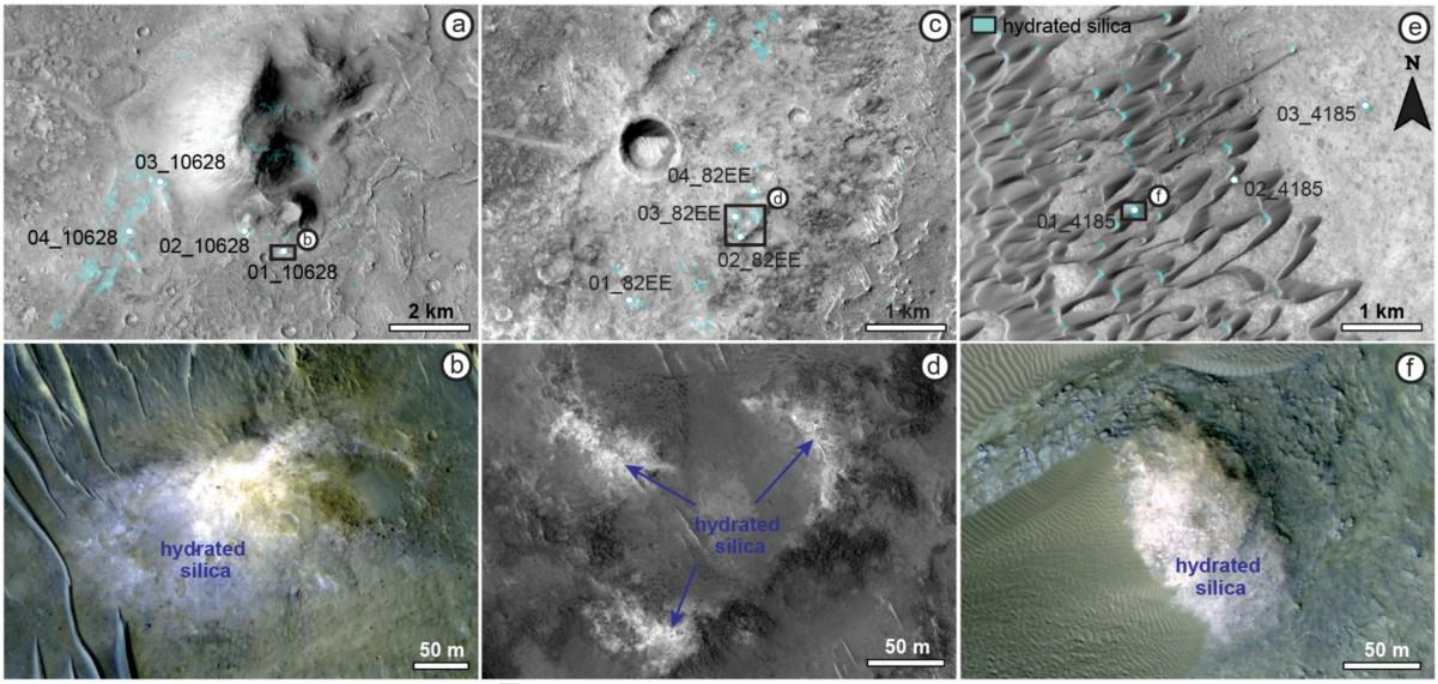

In the Nilosyrtis Mensae region, hydrated silica is present at the base of a stratified sedimentary profile at the outlet of a valley near the hemispheric dichotomy boundary (Amador and Bandfield, 2016) (Figure 6a,b). At the Ius Chasma site, hydrated silica is detected within dark-toned outcrops, on top of layered deposits that are part of the Valles Marineris plateau deposits in association with Al-phyllosilicates and sulfates (Milliken et al., 2008; Roach et al., 2010; Weitz et al., 2010; Le Deit et al., 2010, 2012; Wendt et al., 2011; Carter et al., 2015; Weitz and Bishop, 2016) (Figure 6c,d). East of the volcanic Tharsis region, hydrated silica is detected within several troughs of the Noctis Labyrinthus area where it is part of stratified sequences where Al-phyllosilicates and sulfates have also been detected (Milliken et al., 2008; Weitz et al., 2010, 2011, 2013; Thollot et al., 2012) (Figure 6e,f). Because the hydrated silica is detected in indurated and, locally, stratified deposits that are not part of alluvial fans and/or fan deltas, these detections are grouped as “undifferentiated bedrock deposits”. We also include in this category one detection of the Aeolis Mensae’s hydrated silica where it is detected to the east of an alluvial fan in an impact crater within light-toned deposits associated with the ejecta of a neighboring

crater (Figure 3c). We also include here one detection of the Elorza crater central uplift where hydrated silica is detected in uplifted bedrock (Quantin et al., 2012; Sun and Milliken, 2015, 2018; Hopkins et al., 2017) (Figure 4c,d).

Figure 6 (double column size). Geomorphology of hydrated silica-bearing undifferentiated bedrock. Hydrated silica exposures are mapped in cyan color in the top images (a,c,e). The white circles indicate the regions of interest from which the spectra of hydrated silica were extracted (first number is the number of the ROI and second is the CRISM cube ID) **a.** Portion of CTX image G18_025225_2058_XN_25N283W in Nilosyrtis Mensae (CRISM observation FRT0000D452). **b.** HiRISE RED image ESP_030381_2080 close-up of the hydrated silica-bearing materials. **c.** Portion of CTX RED image P05_003118_1692_XI_10S078W in Ius Chasma (CRISM observation FRT000044AC). **d.** HiRISE RED image PSP_003118_1690 close-up of the hydrated silica-bearing materials. **e.** Portion of CTX image P15_006890_1717_XN_08S098W in Noctis Labyrinthus (CRISM observation FRT000096EE). **f.** HiRISE RED image ESP_016898_1695 close-up of the hydrated silica-bearing materials.

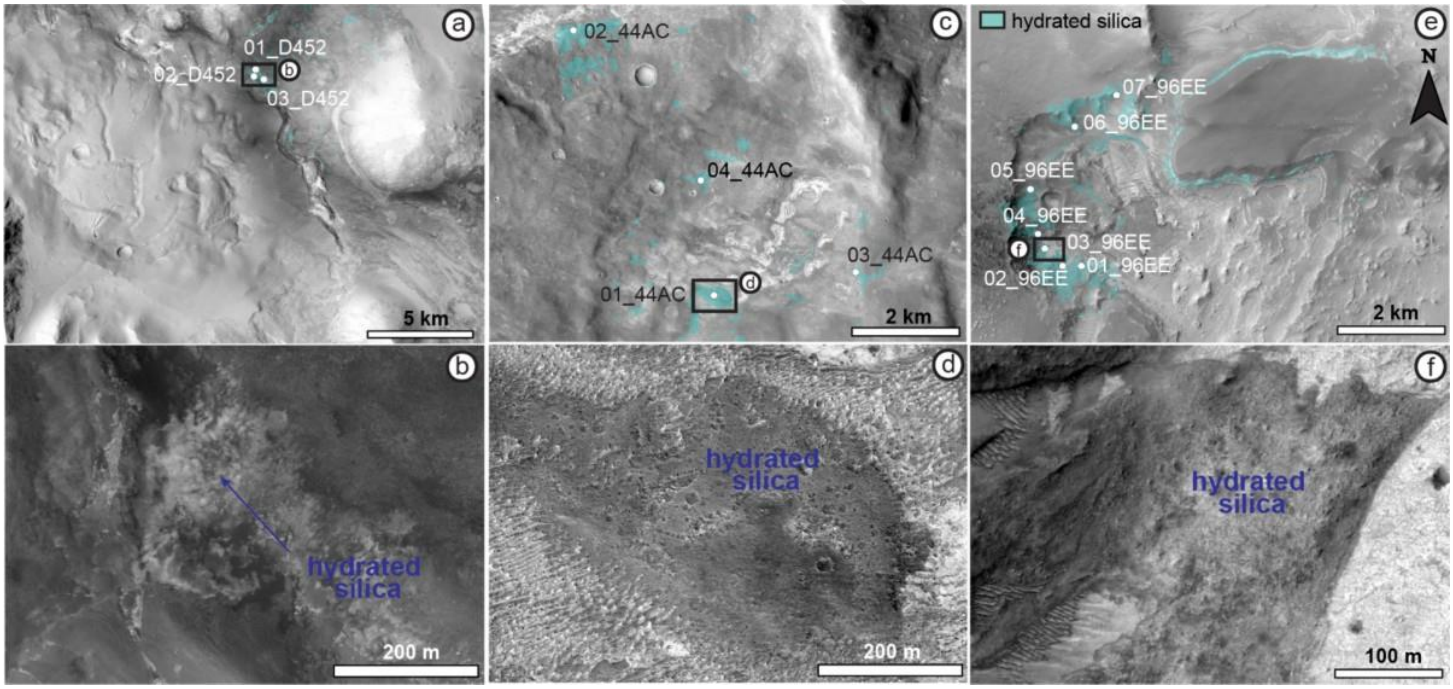

Figure 7 (1.5 column size). Examples of smoothed ratioed spectra of martian hydrated silica detections. Locations and corresponding ROI number and CRISM cube IDs are also provided. The colors of the spectra correspond to the geomorphological contexts where (de)hydrated silica is detected. Hydrated silica-bearing bedrock deposits correspond to dehydrated and/or amorphous silica: band minima shifted to shorter wavelengths on the 1.4 and 1.9 µm absorption features, and 2.2 µm absorption band that is dominant relative to the two other absorptions at 1.4 and 1.9 µm. Hydrated silica-bearing aeolian deposits correspond to hydrated and/or more crystalline silica: band minima shifted to longer wavelengths on the 1.4 and 1.9 µm absorptions features, and 2.2 µm absorption that is not so prevalent compared to other absorption bands at 1.4 and 1.9 µm. Gaps in the spectra are for artifact masking.

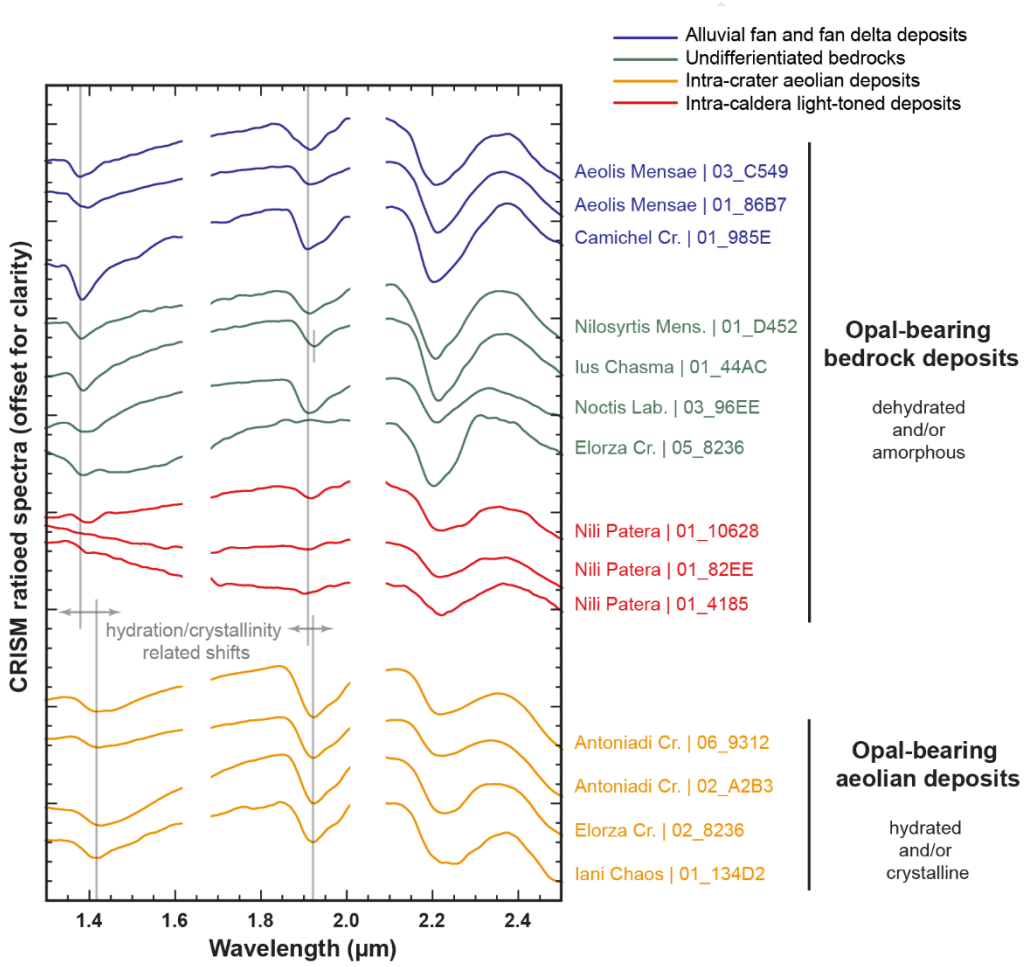

3.5. Spectral feature measurements

Before any calculation of spectral criteria, all spectra were processed by several steps (i.e. Savitzky-Golay smoothing, continuum removal using the Segmented Upper-Hull Method, and gaussian deconvolution) that are explained in Annex 2.

We use several criteria to interpret our spectra. Band minimum position is the most obvious, and corresponds to the position of minimum of reflectance. The area of each band is measured as the sum of the

areas of the gaussian functions contained in each of them (Figure 8). These areas are then converted into relative areas where the area of a single absorption band is normalized to the sum of the areas of all absorption bands (1.4-, 1.9- and 2.2 µm absorption features) in the spectra. This normalization of the areas of the absorption features is mandatory to compare the different contributions of the absorption bands in the terrestrial and martian spectra, because the raw areas of the absorption features of the martian spectra are much smaller than the terrestrial spectra. These relative area contributions are given in percent. Finally, we calculate the Concavity Ratio Criterion (CRC) on the basis of Chauviré et al. (2017a). This geometrical criterion is a quantification of the shape (concavity) of the long wavelength side of each absorption band. The CRC calculation was initially proposed by Chauviré et al. (2017a) on transmission spectra of opals. In this study, we adapt it to reflectance measurements (Figure 9). For each absorption band, two anchor points *S* (λ_S, R_S) and *L* (λ_L, R_L) are fixed; they are the same used for the truncation of the absorption feature (Table 4). The position of the minimum *min* of the band is noted λ_{min} with a reflectance value of R_{min}. The long-wavelength component of the absorption band is noted λ_C (at 1.46, 1.96 and 2.26 µm for the three main absorption features of hydrated silica spectra at 1.4, 1.9 and 2.2 µm) with a reflectance value of R_C. The CRC_c (equation 1) is calculated as the ratio between the true band-depth of the long-wavelength side BD_{c*} (equations 2 and 3) and the virtual band-depth BD_{c**} (equations 4 and 5) that is interpolated into a linear continuum connected to the reflectance minimum *min* (*λmin, Rmin*) and the long-wavelength anchor point noted *L* (λ_L, R_L). According to the equation *(1)*, the more convex thelong-wavelength side is, the higher the CRC value is. Errors bars for each parameter (band minimum, CRC and relative areas), of each sample, are represented as twice the standard error of the mean (SEM) relative to the population to which each sample belongs (e.g. a weathering opal-A relative to all weathering opal-A, a CRISM detection relative to all CRISM detections within the same cube, etc).

(1) $$\mathbf{CRC_C} = \frac{\mathbf{BD_{C*}}}{\mathbf{BD_{C**}}}$$

(2) $$\mathrm{BD_{C*}} = 1 - \frac{\mathrm{R_C}}{\mathrm{R_{C*}}}$$

(3) $$with \quad \mathrm{R_{C*}} = \mathrm{a}.\mathrm{R_S} + \mathrm{b}.\mathrm{R_L}$$

$$where \quad \mathrm{a} = 1 - \mathrm{b} \quad and \quad \mathrm{b} = \frac{\lambda_\mathrm{C} - \lambda_\mathrm{S}}{\lambda_\mathrm{L} - \lambda_\mathrm{S}}$$

(4) $$\mathrm{BD_{C**}} = 1 - \frac{\mathrm{R_{C**}}}{\mathrm{R_{C*}}}$$

(5) $$with \quad \mathrm{R_{C**}} = \mathrm{a'}.\mathrm{R_{min}} + \mathrm{b'}.\mathrm{R_L}$$

$$where \quad \mathrm{a'} = 1 - \mathrm{b} \quad and \quad b' = \frac{\lambda_\mathrm{C} - \lambda_\mathrm{min}}{\lambda_\mathrm{L} - \lambda_\mathrm{min}}$$

Figure 8 (single column size). Example of summed-Gaussian fits for the 1.4, 1.9 and 2.2 µm absorption features of amorphous hydrated silica. The chosen example is the weathering opal-A sample 1040 spectrum that was resampled at the CRISM resolution. Black curves are the raw spectra smoothed with the Savitzky-Golay algorithm and red curves are summed-Gaussian model fits. Adjusted coefficient of determination R^2 relative to each gaussian deconvolution is noted for each absorption feature. Positions of gaussian function centers are detailed in Annex 2 and positions of anchor points used for truncation and in the calculation of the CRC (S for short-wavelength anchor point, L for long-wavelength anchor point) are provided in Table 4.

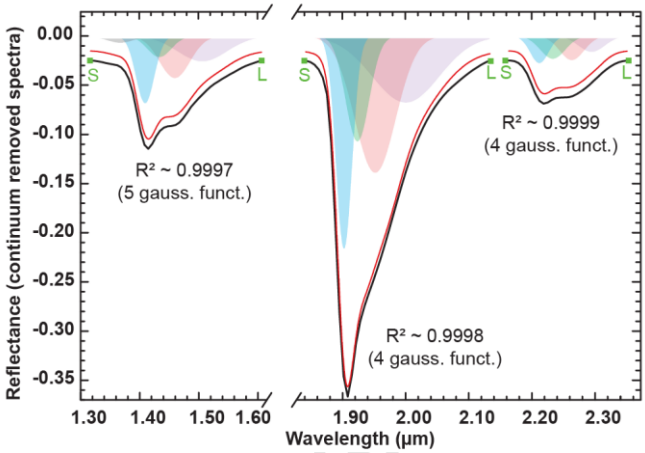

Figure 9 (single column size). Illustration of the concavity-ratio criterion (CRC) calculation for an asymmetric absorption band feature. The CRC quantifies the shape of a multi-peak composite asymmetric absorption band. BD_{C*} is the true band-depth of the long-wavelength side inflection and BD_{C**} is the virtual band-depth of the same point of inflection that is interpolated onto a linear continuum connected to the minimum of reflectance *min* and the long-wavelength anchor point *L*. The CRC_C of the band is calculated as the ratio between BD_{C*} and BD_{C**}. Positions of anchor points (S for short-wavelength anchor point, L for long-wavelength anchor point) are provided in Table 4. More detailed explanations about the CRC calculation are provided in section 3.5.

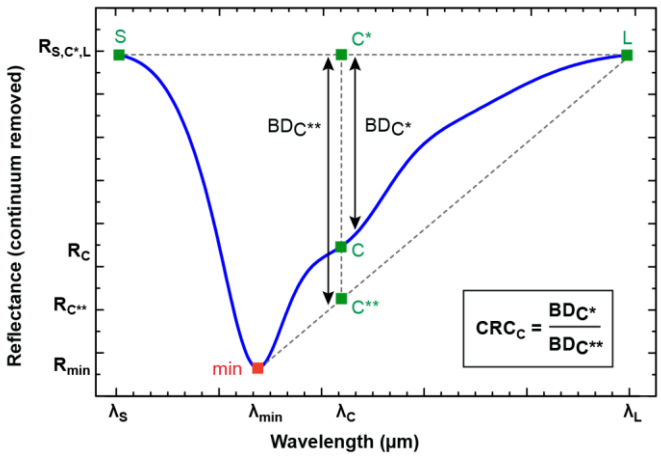

Table 4 (single column size). Positions of the two S and L anchor points (see Figure 9) used for the truncations of each absorption and for the calculation of the concavity-ratio-criterion CRC.

Absorption band	1.4 µm	1.9 µm	2.2 µm
Position of the 1st anchor point S	1.32 µm	1.82 µm	2.13 µm
Position of the 2nd anchor point L	1.60 µm	2.13 µm	2.37 µm

4. Results

4.1. Spectral properties of terrestrial samples at CRISM resolution and ambient atmospheric pressure

The positions of minima of reflectance (in µm), the relative area (in %) and the CRC values of each absorption band are given in Annex 3. Errors are twice the SEM. Whether at laboratory or at CRISM resolutions, results of the spectral criteria applied to the terrestrial samples are very similar in values. Thus, only the results obtained at CRISM resolution are presented in the following parts. Results at the laboratory resolution at ambient atmospheric pressure are available in Annex 4.

4.1.1. Position of the minima of reflectance

At CRISM resolution, the position of the minima of reflectance of the 1.4 µm absorption band ranges from 1.407 to 1.415 µm for opal-A, from 1.414 to 1.453 µm for opal-CT, from 1.423 to 1.425 µm for chalcedony and from 1.405 to 1.413 µm for obsidian and volcanic glass samples (Figure 10a). For the 1.9 µm absorption band, the position of the minima ranges from 1.902 to 1.910 µm for opal-A, from 1.906 to 1.930 µm for opal-CT, from 1.917 to 1.920 µm for chalcedony and from 1.908 to 1.921 µm for all volcanic products (Figure 10b). The minima of the 2.2 µm band range from 2.214 to 2.258 µm for opal-A, from 2.213 to 2.268 µm for opal-CT, from 2.224 to 2.240 µm for chalcedony and from 2.208 to 2.219 µm for all glasses. These results show that the position of the minimum of the 2.2 µm absorption feature does not give any information about the type of hydrated silica as the minima ranges of all materials are overlapping. In contrast, opal-A exhibits position of the minima lower than opal-CT and chalcedony, both on the 1.4- and the 1.9 µm absorption bands. On the 1.4 µm absorption band, it is possible to define a graphical threshold between opal-A and opal-CT. This limit ranges from ~ 1.413-1.414 µm to ~ 1.415-1.416 µm, opal-A having lower band minima. A similar observation can be made on the 1.9 µm absorption band where a threshold ranging from ~ 1.908-1.909 µm to ~ 1.910-1.911 µm is emerging, opal-A having lower band minima as well. In both cases, the range between the lower and upper limits is a zone of uncertainty. Therefore the position of minima at 1.4 and 1.9 µm can discern between

amorphous hydrated silica (volcanic glasses and opal-A) and more crystalline hydrated silica species (opal-CT and chalcedony) (Figure 10a,b) (Langer and Florke, 1974; Rice et al., 2013; Sun, 2017). Volcanic products show a position of minima at 1.4 µm similar to opal-A (below 1.413 µm (Figure 10a), but a wide range of position of minima at 1.9 µm, overlapping those of opal-A and opal-CT (Figure 10b).

Figure 10 (double column size). Diagrams of the band minima positions for each terrestrial hydrated silica variety measured at ambient atmospheric pressure and resampled at the CRISM resolution. **a.** for the 1.4 µm absorption feature (attributed to both OH and H_2O vibrations). **b.** for the 1.9 µm absorption feature (attributed to molecular water). Error bars for the band minima position values are twice the standard error on each calculation. Grayed areas represent the areas of uncertainty separating opal-A and opal-CT thresholds.

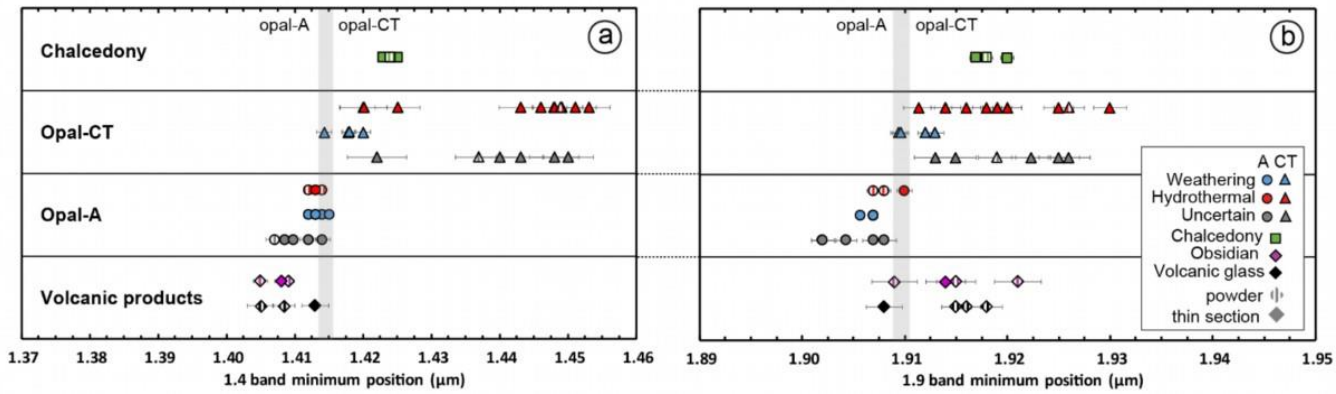

4.1.2. Concavity-Ratio-Criterion calculations

CRC calculated on the 2.2 µm absorption band (hereafter $CRC_{2.2}$) values are widely ranging from 0.04 and 1.34 (Annex 3). Weathering opal $CRC_{2.2}$ values range from 0.99 to 1.21. They are ranging from 1.10 to 1.21 for chalcedony samples and 0.80 to 1.01 for volcanic samples (obsidians and glasses). Hydrothermal opals show the greatest variations in their $CRC_{2.2}$ that vary from 0.42 to 1.21. Hence, clusters of geological origin are overlapping one another. The $CRC_{2.2}$ does not permit separation of either weathering or hydrothermal varieties of hydrated silica nor volcanic products and chalcedony from opals.

The $CRC_{1.4}$ values range from ~ 0.00 to 1.13 (Figure 11a). The volcanic products have the lowest $CRC_{1.4}$ values from ~ 0.00 to 0.36 compared to the weathering/hydrothermal opals and chalcedony for which values vary from 0.66 to 1.13. Weathering opals have $CRC_{1.4}$ values ranging from 0.66 to 0.99. Hydrothermal opals have $CRC_{1.4}$ values slightly but significantly higher, ranging from 0.96 to 1.13. The slight overlap in the values is due to opal-A powders. This overlap is absent when considering only opal-CT samples. Considering this overlap, a threshold to discern weathering and hydrothermal hydrated silica could be placed at $CRC_{1.4}$ values ranging from ~ 0.95-0.96 to ~ 0.99-1.00 (Figure 11a). Chalcedony's $CRC_{1.4}$ values range from 0.89 to 1.01, which are rather intermediate between weathering and hydrothermal $CRC_{1.4}$ values.

Results of the CRC calculations on the 1.9 µm absorption band also enable us to distinguish between weathering and hydrothermal terrestrial opals with higher accuracy. Weathering opals have $CRC_{1.9}$ values ranging from 0.57 to 0.90 and hydrothermal opals from 0.85 to 1.07 (Figure 11b). An overlap is present between the two clusters, but it is due to a single weathering opal-A sample. A threshold can be placed at $CRC_{1.9}$ values ranging from ~ 0.85-0.86 to ~ 0.90-0.91 to discern between weathering and hydrothermal varieties of hydrated silica (Figure 11b). Like the case of the minima thresholds, the range between the lower and upper limits is a zone of uncertainty: i.e, for the samples that have CRC values that are within these two extended limits, the geological origin (weathering or hydrothermal) is ambiguous. As for the 1.4 µm case, volcanic products have the lowest $CRC_{1.9}$ values ranging from 0.15 to 0.52. Contrary to the 1.4 µm case, chalcedony samples have $CRC_{1.9}$ values that are closer to hydrothermal opals with a range from 0.81 to 0.89.

Figure 11 (double column size). Diagrams of the CRC calculations for each terrestrial hydrated silica variety measured at ambient atmospheric pressure and resampled at the CRISM resolution. **a.** for the 1.4 µm absorption feature (attributed to both OH and H_2O vibrations). **b.** for the 1.9 µm absorption feature (attributed to molecular water). Error bars for the CRC values are twice the standard error on each calculation. Grayed areas represent the areas of uncertainty separating hydrothermal opals and weathering opals thresholds.

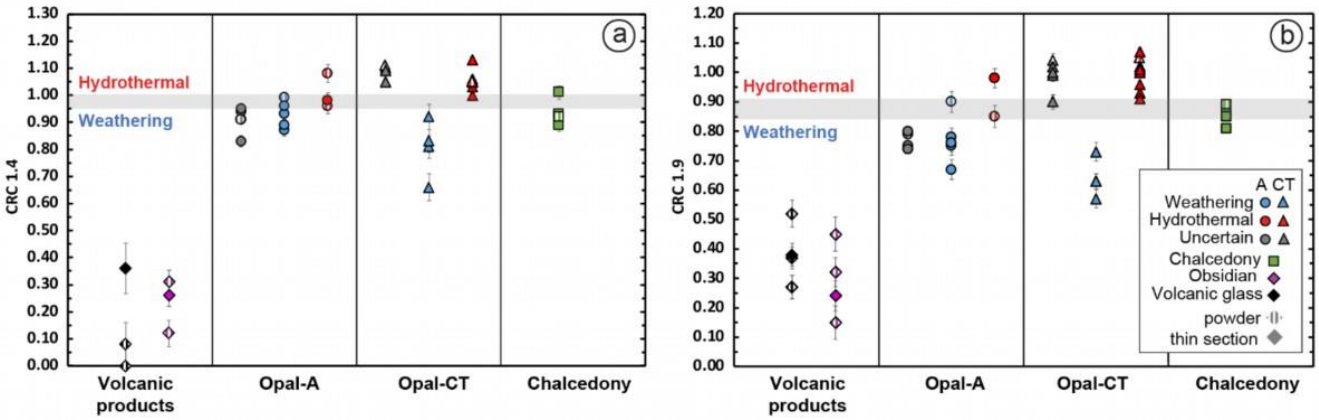

4.1.3. Graphic combinations of CRC calculations and reflectance minima positions

Graphic combinations of CRC calculations and reflectance minima positions for each absorption band provide an easy visual guide to discriminate the types of hydrated silica and the different geological origins. Figure 12a is a diagram of the $CRC_{2.2}$ as a function of the 2.2 µm band minimum position. As presented previously, these two spectral criteria do not permit distinguishing the type of hydrated silica nor the geological processes of formation. Thus, it is not surprising that this diagram does not show any field relative to the crystallinity of the hydrated silica or to its geological origin. Figures 12b,c are diagrams combining the CRC and the minimum position of the same band, respectively for 1.4 µm and 1.9 µm bands. When considering a single

absorption band, each diagram presents four fields bounded by the various thresholds discussed above: weathering opal-A and weathering opal-CT, hydrothermal opal-A and hydrothermal opal-CT. Diagrams plotting 1.4- and 1.9 µm absorption bands show that weathering and hydrothermal opal-CT are well discriminated with the $CRC_{1.4}$ and $CRC_{1.9}$ thresholds (Figure 12b,c). This distinction is less obvious when considering opal-A powders. On the 1.4 µm absorption band related plot, there is a great overlap between the two clusters, whereas this overlap is less prevalent on the 1.9 µm absorption band related plot, which makes the distinction between the two clusters easier. Whatever the considered band, chalcedony samples form an intermediate cluster between weathering opal-CT and hydrothermal opal-CT. Volcanic products (obsidians and volcanic glasses) are always distant from opals and chalcedony when considering CRC values. Furthermore, on the 1.4 µm related plot (Figure 12b), they are close to the weathering opal-A field which appears consistent with their amorphous structure. They are mostly located in the weathering opal-CT field on the 1.9 µm related-plot (Figure 12c), which is then inconsistent with their amorphous structure.

Figure 12 (single column size). Diagrams of the CRC calculations as function of the minima of reflectance for each absorption band for terrestrial hydrated silica varieties measured at ambient atmospheric pressure and resampled at the CRISM resolution. **a.** for the 2.2 µm absorption feature (attributed to silanol groups). **b.** for the 1.4 µm absorption feature (attributed to both OH and H_2O vibrations). **c.** for the 1.9 µm absorption feature (attributed to molecular water). Error bars for the position of the minimum of reflectance and for CRC values are twice the standard error on each spectral criteria. Black arrows indicate graphic migrations for powder samples and thin sections. Grayed areas represent the areas of uncertainty separating opal-A and opal-CT, and weathering-hydrothermal opals thresholds.

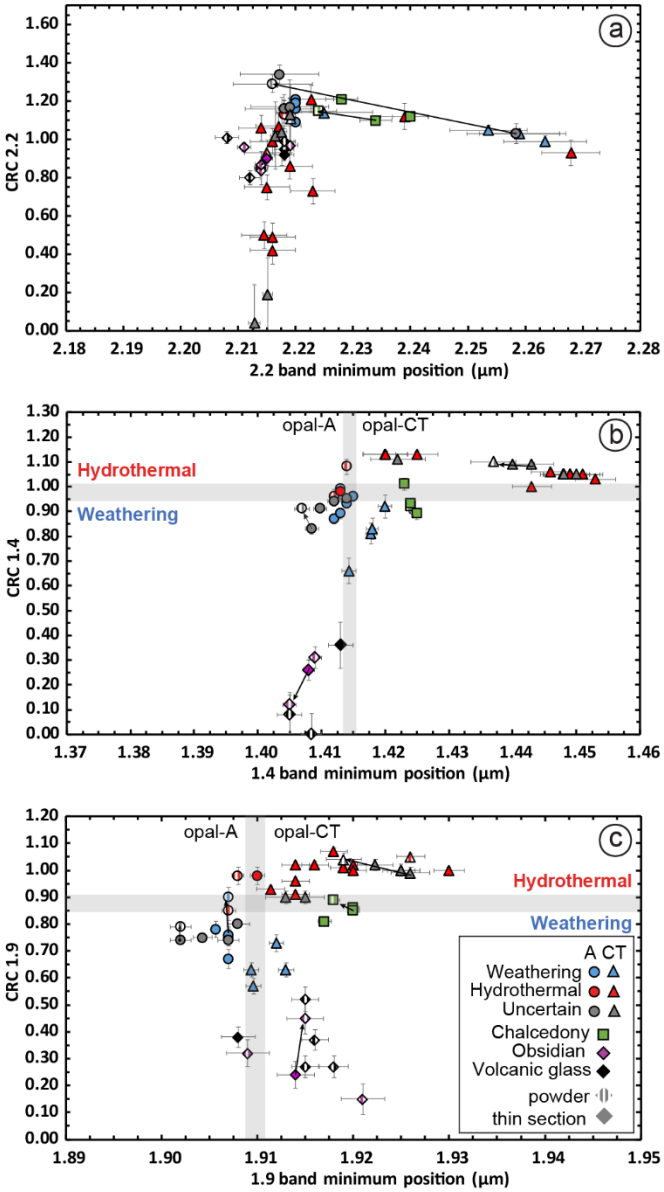

4.2. Spectral properties of terrestrial samples at CRISM resolution at Mars-relevant atmospheric pressure

For the investigation of the NIR spectra of terrestrial hydrated silica at Mars-relevant atmospheric pressure, we present and discuss the results of the spectral criteria obtained with the graphics that combine the CRC and band minima values. Spectra before and after low-pressure exposure of the samples are shown in Figure 13. The results for the terrestrial samples at CRISM resolution and Mars-relevant atmospheric pressure are given in Table 5. Results at the laboratory resolution at Mars-relevant atmospheric pressure are available in Annex 5.

Of the eight terrestrial opal samples selected for experiments in martian atmospheric conditions, only two (the two weathering opal-CT FT1111 and VTB) show significant lowering of their minima and CRC values on the 1.4 and 1.9 µm absorption bands. The 1.4 µm band minimum of the VTB sample shifts from 1.418 to 1.416 µm and the $CRC_{1.4}$ value shifts from 0.81 to 0.63. For the 1.9 µm absorption band, the band minimum shifts from 1.909 to 1.908 µm and the $CRC_{1.9}$ drops from 0.63 to 0.37. For the FT1111 sample, the 1.4 µm band minimum shifts from 1.414 to 1.411 µm, the 1.9 µm band minimum from 1.910 to 1.908 µm, and the CRC values drop from 0.66 to 0.45 and from 0.51 to 0.41 for the 1.4- and 1.9 µm absorptions bands respectively. Furthermore, their spectral criteria calculated on the 2.2 µm absorption band show large variations. At the beginning of the experiment, their band minima are at 2.264 and 2.254 µm, and they both drop to 2.191 and 2.192 µm for VTB and FT1111 respectively. However, their $CRC_{2.2}$ values do not evolve in the same way. For the VTB sample, the $CRC_{2.2}$ increases from 0.99 to 1.33, whereas it decreases from 1.05 to 0.75 for the FT1111 sample. Two other opal samples show moderate spectral changes, the hydrothermal opal-CT 1543b (only on the 1.4 µm absorption band minimum that slightly shifts from 1.448 to 1.441 µm), and the opal-A sample from uncertain origin 86.2 (on the 2.2 µm absorption band minimum that shifts from 2.258 to 2.219 µm). All other samples did not show any particular reaction to the Mars-relevant atmospheric pressure as their band minima and CRC values on the three absorption bands do not significantly change.

By taking into account all these evolutions of the CRC and band minima values, the thresholds developed in the terrestrial data at ambient pressure need to be modified to allow for the possible dehydration of hydrated silica under martian atmospheric pressure. Like for the measurements at ambient atmospheric pressure, the 2.2 µm absorption band still does not provide any information in terms of crystallinity or geological origin for the samples (Figure 14a). Both on the 1.4- and 1.9 µm absorption bands, the band minima and CRC thresholds need to be expanded towards lower values. Indeed, at the Mars-relevant atmospheric pressure, the opal-A/opal-CT thresholds are ranging from ~ 1.410-1.411 to ~ 1.415-1.416 µm and ~ 1.906-1.907 to ~ 1.910-1.911 µm (Figure 14b,c). In parallel, the weathering/hydrothermal thresholds are ranging from ~

0.88-0.89 to ~ 0.99-1.00 for the 1.4 µm absorption band, and from ~ 0.78-0.79 to ~ 0.90-0.91 for the 1.9 µm absorption (Figure 14b,c). The modifications of these limits have the effect of widening the intervals of uncertainty.

Figure 13 (single column size). NIR reflectance spectra (continuum removed ; Section 3.5) of the opal samples used for the low-pressure experiment at Mars-like atmospheric pressure resampled at the CRISM resolution. For each sample, two spectra are plotted: upper spectra were acquired at ambient atmospheric conditions, lower spectra were acquired after low-pressure exposure. Spectra in blue colors are for weathering opals, spectra in red are for hydrothermal opals, and spectra in black and gray are for opals of uncertain origin. Black arrows indicate absorption of silanol Si-OH vibrations at shorter wavelengths for reactive samples during dehydration experiment. The main absorption bands of hydrated silica described in Section 2.3 are labeled as vertical lines.

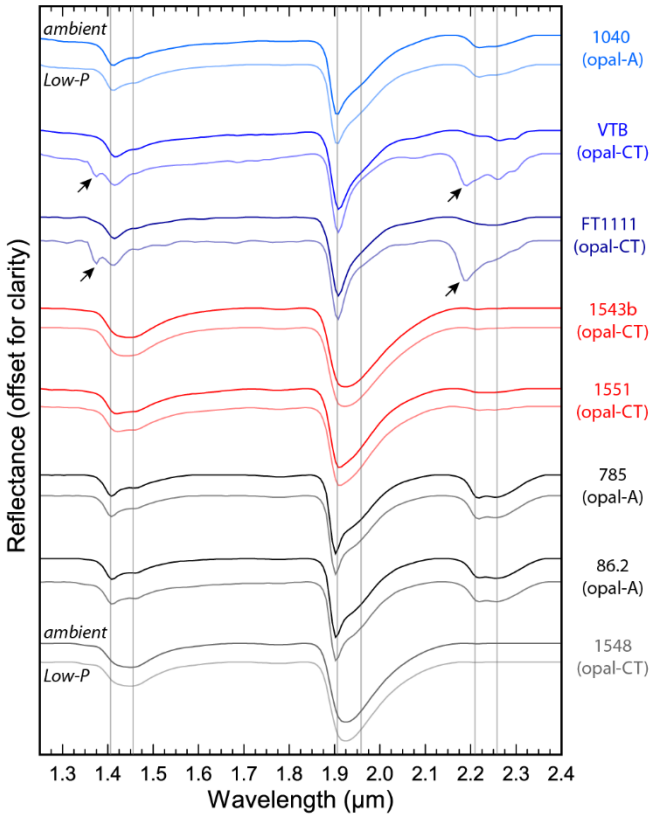

Table 5 (double column size). Results of the spectral criteria calculations on terrestrial data resampled at the CRISM resolution at Mars-relevant atmospheric pressure (all samples are thin sections).

Geological origin	Silica variety	Sample ID	1.4 µm absorption band						1.9 µm absorption band						2.2 µm absorption band						
			Min. Pos. (µm)	σ	CRC	σ	Rel. Area (%)	σ	Min. Pos. (µm)	σ	CRC	σ	Rel. Area (%)	σ	Min. Pos. (µm)	σ	CRC	σ	Rel. Area (%)	σ	Experiment duration and atmospheric pressure at the end of acquisition
Weathering (T < 50°C)	Opal-A	1040 (ambient)	1.412	*0.0001*	0.87	*0.003*	21	*0.9*	1.906	*0.0001*	0.78	*0.003*	68	*1.6*	2.220	*0.0004*	1.21	*0.017*	11	*0.7*	6h46 at 7.68 mbar
		1040 (low-pressure)	1.412	*0.0001*	0.88	*0.003*	21	*0.9*	1.906	*0.0001*	0.77	*0.003*	69	*1.6*	2.219	*0.0004*	1.16	*0.017*	11	*0.7*	
	Opal-CT	VTB (ambient)	1.418	*0.0007*	0.81	*0.0600*	24	*0.9*	1.909	*0.0004*	0.63	*0.0800*	66	*7.3*	2.264	*0.0241*	0.99	*0.1133*	10	*8.2*	14h42 at 7.24 mbar
		VTB (low-pressure)	1.416	*0.0007*	0.63	*0.0600*	21	*0.9*	1.908	*0.0004*	0.39	*0.0800*	44	*7.3*	2.191	*0.0241*	1.33	*0.1133*	35	*8.2*	
		FT1111 (ambient)	1.414	*0.0012*	0.66	*0.0700*	20	*0.4*	1.910	*0.0006*	0.57	*0.0533*	70	*8.1*	2.254	*0.0207*	1.05	*0.1000*	10	*7.7*	7h40 at 7.25 mbar
		FT1111 (low-pressure)	1.411	*0.0012*	0.45	*0.0700*	21	*0.4*	1.908	*0.0006*	0.41	*0.0533*	46	*8.1*	2.192	*0.0207*	0.75	*0.1000*	33	*7.7*	
Hydrothermal (T > 50-100°C)	Opal-CT	1543b (ambient)	1.448	*0.0025*	1.05	*0.0067*	24	*0.1*	1.918	*0.0001*	1.07	*0.0000*	76	*0.1*	2.215	*0.0003*	0.50	*0.0267*	0	*0.0*	4h00 at 7.36 mbar
		1543b (low-pressure)	1.441	*0.0025*	1.07	*0.0067*	24	*0.1*	1.918	*0.0001*	1.07	*0.0000*	76	*0.1*	2.216	*0.0003*	0.58	*0.0267*	1	*0.0*	
		1551 (ambient)	1.420	*0.0000*	1.13	*0.0067*	22	*0.0*	1.911	*0.0001*	0.93	*0.0033*	75	*0.1*	2.223	*0.0009*	1.21	*0.0333*	3	*0.1*	14h40 at 7.25 mbar
		1551 (low-pressure)	1.420	*0.0000*	1.15	*0.0067*	22	*0.0*	1.912	*0.0001*	0.94	*0.0033*	75	*0.1*	2.220	*0.0009*	1.11	*0.0333*	3	*0.1*	
Uncertain or Unclear	Opal-A	785 (ambient)	1.409	*0.0000*	0.83	*0.0033*	16	*0.1*	1.902	*0.0003*	0.74	*0.0000*	61	*0.0*	2.217	*0.0000*	1.34	*0.0033*	23	*0.0*	3h08 at 7.36 mbar
		785 (low-pressure)	1.409	*0.0000*	0.84	*0.0033*	16	*0.1*	1.903	*0.0003*	0.74	*0.0000*	61	*0.0*	2.217	*0.0000*	1.33	*0.0033*	23	*0.0*	
		86.2 (ambient)	1.410	*0.0001*	0.91	*0.0067*	17	*0.4*	1.904	*0.0000*	0.75	*0.0000*	62	*0.4*	2.258	*0.0131*	1.03	*0.1200*	21	*0.1*	4h18 at 7.21 mbar
		86.2 (low-pressure)	1.410	*0.0001*	0.93	*0.0067*	18	*0.4*	1.904	*0.0000*	0.75	*0.0000*	61	*0.4*	2.219	*0.0131*	1.39	*0.1200*	21	*0.1*	
	Opal-CT	1548 (ambient)	1.450	*0.0001*	1.05	*0.003*	22	*0.1*	1.922	*0.0002*	1.02	*0.000*	77	*0.1*	2.215	*0.0002*	0.19	*0.020*	1	*0.0*	3h52 at 7.17 mbar
		1548 (low-pressure)	1.450	*0.0001*	1.04	*0.003*	22	*0.1*	1.922	*0.0002*	1.02	*0.000*	77	*0.1*	2.215	*0.0002*	0.25	*0.020*	1	*0.0*	

σ = SEM for Standard Error

Figure 14 (single column size). Diagrams of the CRC calculations as function of the minima of reflectance for each absorption band for terrestrial hydrated silica varieties measured at Mars-relevant atmospheric pressure and resampled at CRISM resolution. **a.** for the 2.2 µm absorption feature (attributed to silanol groups). **b.** for the 1.4 µm absorption feature (attributed to both OH and H_2O vibrations). **c.** for the 1.9 µm absorption feature (attributed to molecular water). Error bars for the position of the minimum of reflectance and for CRC values are twice the standard error on each spectral criterion. Tie lines and black arrows indicate migrations for the selected samples from the ambient to low-pressure measurement spectral criteria calculation. Grayed areas represent the areas of uncertainty separating opal-A/opal-CT and hydrothermal/weathering opals. Dark grayed areas are the ones resulting from the spectral criteria calculations at ambient laboratory conditions. They expand to the boundaries of the light grayed areas during the low-pressure exposure as indicating by the doubled arrows

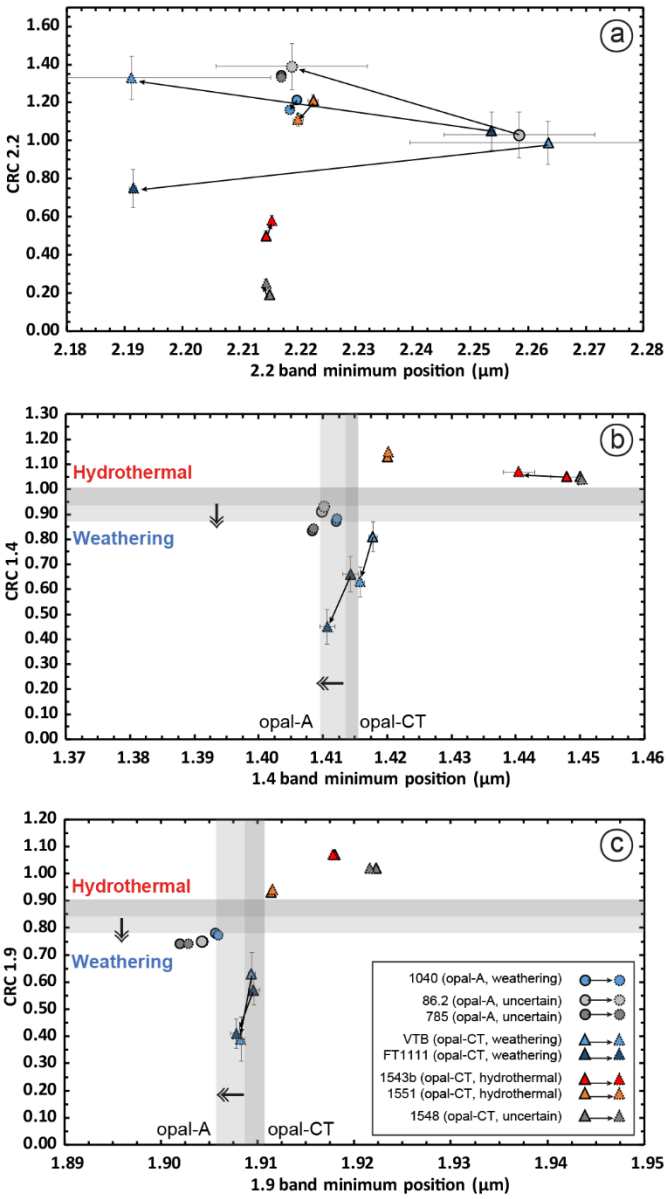

4.3. Spectral properties of martian hydrated silica

For the martian application of the spectral criteria developed on the terrestrial samples, we will mostly present and discuss the results obtained with the graphic combinations of the CRC with the minimum of each absorption bands. The CRISM related graphic combinations are based on the same graphic combinations obtained on the terrestrial data resampled at the CRISM resolution with the thresholds developed on the Mars-relevant atmospheric pressure experiment. The results for each CRISM detection of hydrated silica are listed in the Annex 6.

Figure 15a represents the spectral criteria applied to the 2.2 µm absorption feature. All CRISM detections have very similar values in terms of reflectance minima positions that range from 2.203 to 2.232 µm. We observe a similar trend when considering the $CRC_{2.2}$ values that are all close regardless of the considered sites with values ranging from 0.77 to 1.28. Therefore, CRISM detections have spectral criteria results that do not show significant variability compared to the terrestrial data on the 2.2 µm absorption band. Nevertheless, as in the case of terrestrial data, the 2.2 µm absorption feature does not permit distinguishing between potential weathering and hydrothermal silica detections nor between amorphous and more crystalline martian hydrated silica detections.

When considering the 1.4 µm absorption band (Figure 15b), the majority of the sites where hydrated silica is detected in bedrock deposits (i.e hydrated silica-bearing alluvial fans and fan delta in Aeolis Mensae and Camichel crater, hydrated silica-bearing stratified plateaus of Ius Chasma, hydrated silica in the bedrock of Nilosyrtis Mensae and Noctis Labyrinthus) are closer to the terrestrial weathering opal-A field. Their 1.4 µm band minima positions range from 1.377 to 1.407 µm, which are lower than for the terrestrial opal-A, and their $CRC_{1.4}$ values range from 0.09 to 1.06. There are only two points of these bedrock detections that tend to be close to hydrothermal terrestrial opal-A: one detection in the bedrock of Elorza crater (1.4 µm band minimum at 1.383 µm and $CRC_{1.4}$ equal to 1.06) and one detection around the Nili Tholus cone in the Nili Patera caldera (1.4 µm band minimum at 1.396 µm and $CRC_{1.4}$ value at 0.89). Hydrated silica detections in aeolian materials around central peaks of impact craters (i.e hydrated silica-bearing aeolian deposits in Iani Chaos, Antoniadi crater and Elorza crater) are closer to the hydrothermal opal-CT cluster with 1.4 µm band minima positions ranging from 1.415 to 1.449 µm and $CRC_{1.4}$ values ranging from 0.78 to 1.15 (except for two detections in Iani Chaos, three in the Antoniadi crater region and one detection in Elorza crater for which $CRC_{1.4}$ range from 0.78 to 0.91). These results show that the spectral criteria applied to the 1.4 µm absorption feature on the martian data do permit separating the two following clusters: hydrated silica-bearing bedrock deposits closer to the

terrestrial weathering opal-A field, and hydrated silica-bearing aeolian materials closer to the terrestrial hydrothermal opal-CT field.

In the case of the spectral criteria applied to the 1.9 µm absorption band (Figure 15c), similar results are obtained, although the two clusters, hydrated silica-bearing aeolian materials and hydrated silica-bearing bedrock deposits, are slightly overlapping. The hydrated silica-bearing aeolian deposits have 1.9 µm minima ranging from 1.917 to 1.941 µm and $CRC_{1.9}$ between 0.68 and 1.04. Most of these data (e.g. Antoniadi crater and Elorza crater) are closer to the terrestrial hydrothermal opal-CT field. The Iani Chaos detections have lower values of the $CRC_{1.9}$ that are ranging from 0.68 to 0.80, which place this hydrated silica in the terrestrial weathering opal-CT field. Hydrated silica-bearing bedrock deposits have 1.9 µm minima between 1.906 and 1.938 µm and $CRC_{1.9}$ values ranging from 0.14 to 1.00. Except for the Camichel crater detections, all detections in bedrock deposits (Aeolis Mensae, Ius Chasma, Nilosyrtis Mensae, Noctis Labyrinthus and Nili Patera) are located in the weathering opal-CT field with 1.9 µm minima ranging from 1.906 to 1.938 µm and $CRC_{1.9}$ values included between 0.54 and 0.97. Camichel crater detections have high $CRC_{1.9}$ values that can be caused by residual CO_2 atmospheric absorption that tend to artificially increase the $CRC_{1.9}$ values. This observation of different minima positions between the 1.4- and the 1.9 µm bands for these sites is relatively similar to the observations for the volcanic products on terrestrial data. In contrast to the application of the spectral criteria to the 1.4 µm absorption band, Camichel crater detections are located mostly in the hydrothermal opal-A field with high $CRC_{1.9}$ values ranging from 0.89 to 1.00 and low 1.9 µm band minima that range from 1.906 to 1.910 µm. In addition, one detection in the Nilosyrtis Mensae's bedrock is located in the terrestrial hydrothermal opal-CT field with 1.9 µm minimum at 1.938 µm and $CRC_{1.9}$ value at 0.97. Note that all detections in the Nili Patera caldera have the lowest $CRC_{1.9}$ values (ranging from 0.14 to 0.49), except for one point with a higher $CRC_{1.9}$ value equal to 0.83.

Overall, the hydrated silica-bearing aeolian deposits cluster is always closer to the hydrothermal opal-CT field whereas the hydrated silica-bearing bedrock cluster is always closer to the weathering opal-A and –CT fields, although subtle variations can be noted depending on the considered absorption band (1.4 or 1.9 µm absorption features) (Figure 15b,c).

Figure 15 (single column size). Diagrams of the CRC calculations as function of the minima of reflectance for each absorption band on CRISM data**. a.** for the 2.2 µm absorption feature (attributed to silanol groups). **b.** for the 1.4 µm absorption feature (attributed to both OH and H_2O vibrations). **c.** for the 1.9 µm absorption feature (attributed to molecular water). Opal-A/CT and hydrothermal/weathering thresholds on the 1.4- and 1.9 µm absorption features are those obtained on the terrestrial data resampled at the CRISM resolution and Mars-relevant atmospheric pressure (see Figure 14). Blue dots in c. surrounded by a black dashed line (Camichel crater hydrated silica detections) have high $CRC_{1.9}$ values that could be explained by residual CO_2 atmospheric absorptions that artificially increase the $CRC_{1.9}$ values. Error bars for the position of the minimum of reflectance and for CRC values are twice the standard error on each spectral criterion. Grayed areas represent the areas of uncertainty separating opal-A/opal-CT and hydrothermal/weathering opals developed on terrestrial samples at Mars-relevant atmospheric pressure

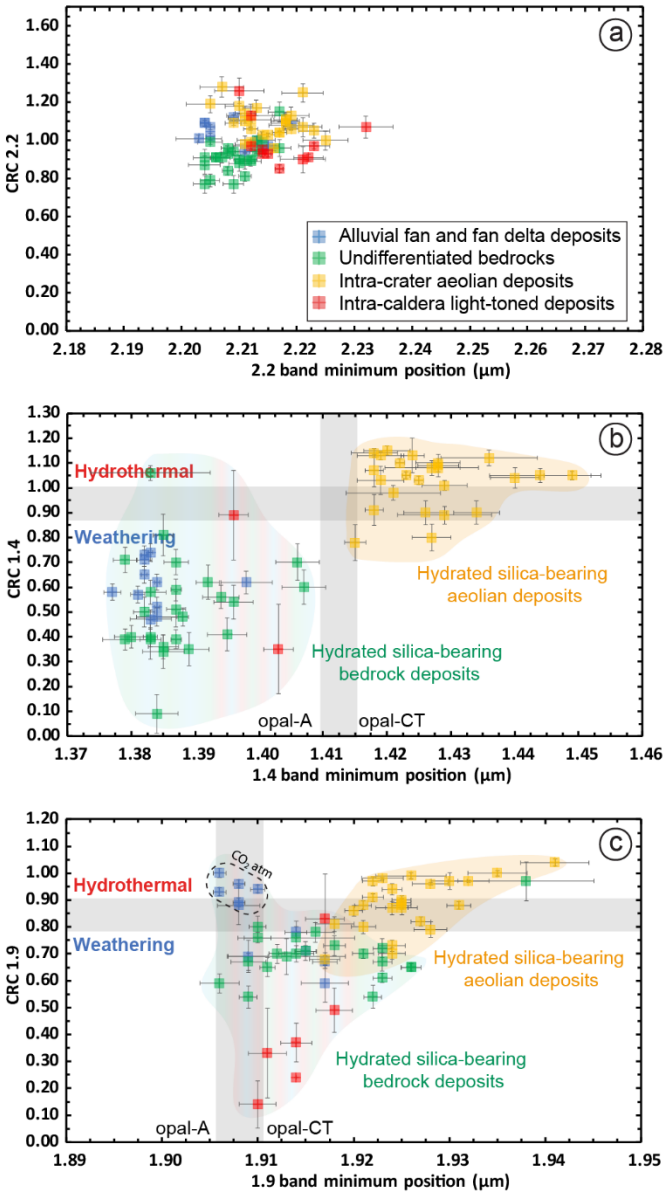

4.3. Absorption bands on both terrestrial and martian silica

The ternary diagram in the Figure 16 presents the relative contribution of the three absorption bands in terms of band areas (Table 5 and Annex 3,6). Terrestrial samples at ambient atmospheric pressures show low contributions and variations of the 1.4 µm absorption band with relative areas ranging from ~ 0 to 32 %. The greatest variations for the terrestrial data are due to the relative contributions of the 1.9 and 2.2 µm absorption bands, with ranges from 3 to 79 % and ~ 0 to 91 %, respectively. Several opal-CT samples exhibit 2.2 µm absorption bands that are weak. For these samples, the 2.2 µm absorption band is negligible compared to the two other absorption bands. The diagram in Figure 16 does not reveal any connection with the geological origin of hydrated silica (weathering vs hydrothermal). However, it seems that the relative area of the 2.2 µm band increases conjointly with a decrease in the relative contribution of the 1.9 µm absorption feature. Overall, a global trend can be established: the 2.2 µm band contributes more and more (and the 1.9 µm less and less) for opal-CT, then opal-A, then chalcedony and then volcanic glass. Furthermore, spectra measured on thin sections show less variability than those measured on powders but for a given sample, the spectra do not show the same relative area. In the case of opal and chalcedony samples, powders have lower contributions of the 1.9 µm absorption band. It remains difficult to give any interpretation about differences between thin sections and powders for volcanic products because only two samples were prepared in thin sections.

Among the eight terrestrial opal samples that were analyzed under a Mars-relevant atmospheric pressure, the only samples that show variations of their relative band areas are the same samples that exhibit variations in their band minima and CRC values, namely the weathering opal-CT samples VTB and FT1111. Although the relative areas of their 1.4 µm absorption bands does not vary significantly, their 1.9 µm absorption band relative areas decrease from 66 to 44% and from 70 to 46%, and their 2.2 µm absorption band relative areas increase from 10 to 35% and from 10 to 33% for the samples VTB and FT1111 respectively. These variations have the effect of shifting these two opal-CT samples within the chalcedony field on the ternary diagram of the Figure 16.

Martian data are aligned on the trend defined by the terrestrial data (both at ambient and Mars-relevant atmospheric pressures) and they are located in the gap between terrestrial opals/chalcedony and volcanic glasses (Figure 16). Variations of the relative contributions of the absorption bands are mainly affected by the relative areas of the 1.9 and 2.2 µm absorption bands that vary from 12 to 49 % and 34 to 87 % (the relative area of the 1.4 µm feature varying from 13 to 26 %). As in the case of terrestrial data, martian detections show an evolution of the different sites in parallel with the 1.9/2.2 relative area variations. From the right to the left of the ternary diagram, the sites with the highest contributions of the relative area of the

1.9 µm bands (lowest contributions of the 2.2 µm feature) are mostly the sites where hydrated silica is detected within aeolian deposits (Antoniadi crater, Elorza crater and Iani Chaos) with relative area of the 1.9 µm feature ranging from 29 to 49 % and 34 to 48 % for the 2.2 µm feature. The hydrated silica-bearing bedrocks (Noctis Labyrinthus, Camichel crater, Aeolis Mensae, Ius Chasma and Nili Patera) have a slight overlap with the hydrated silica-bearing aeolian deposits but have lower contributions of the 1.9 µm band and higher contributions of the 2.2 µm band with percentages between 12 to 40 % and 43 to 87 % respectively. These two clusters related to type of deposits are well defined and point to two kinds of terrestrial end-members. The hydrated silica-bearing aeolian deposits are closer to the terrestrial chalcedony and dehydrated opal-CT samples. Hydrated silica-bearing bedrock deposits tend to be closer in value to the terrestrial volcanic products.

Figure 16 (double column size). Contributions of each absorption band of terrestrial data resampled at the CRISM resolution and martian data displayed as a ternary diagram. Contributions of each absorption band are interpreted as the relative area of each absorption feature compared to all absorptions forming the spectra. Black arrows indicate migrations for powder samples and thin sections. Black dotted arrows indicate migrations for the selected samples for the Mars-relevant atmospheric pressure study from the beginning to the end of the experiment (only FT1111 and VTB samples).

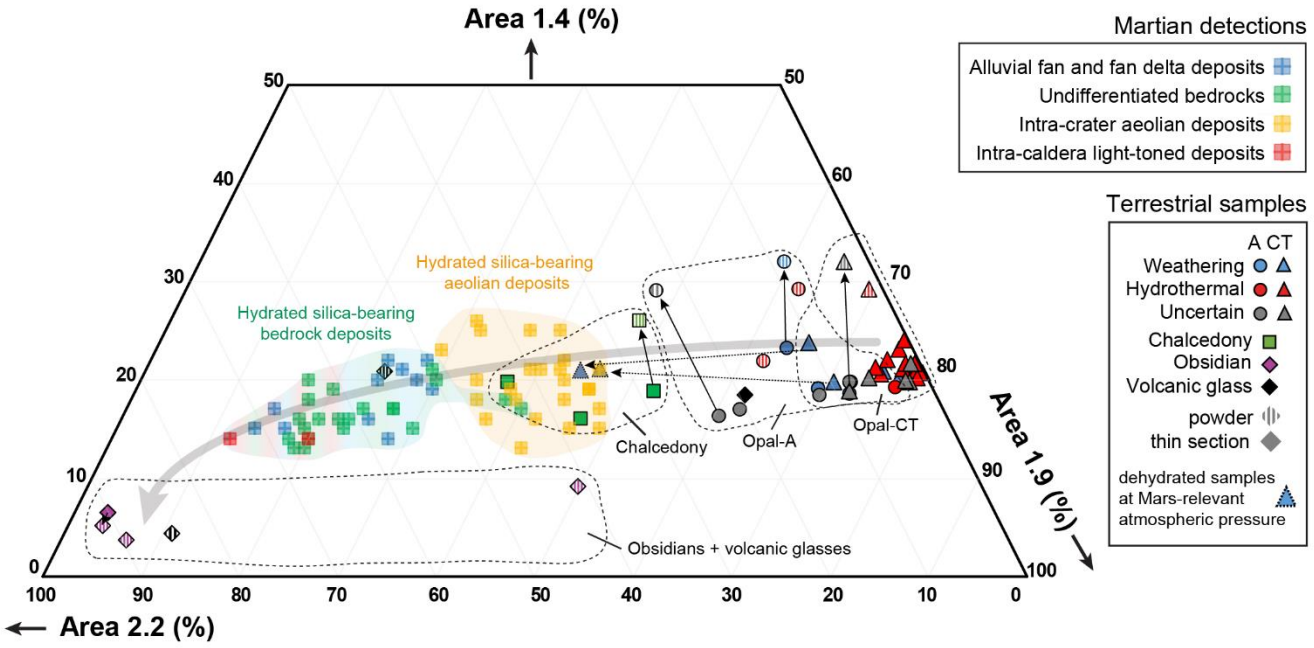

5. Discussion

5.1. Crystallinity and concavity criteria application on terrestrial data

5.1.1. Distinction of opal genesis with the CRC thresholds

For the terrestrial data, we obtained similar results both on the laboratory and CRISM resolutions. The CRISM resolution is therefore sufficient to apply these spectral criteria in order to discern between opal-A and opal-CT, and to discern hydrothermal and weathering opals. Our results obtained on reflectance measurements are also very similar to the results of Chauviré et al. (2017a) on transmission measurements. Compared to their results, we can observe some subtle differences, especially on the weathering/hydrothermal thresholds. Chauviré et al. (2017a) showed that weathering opals have $CRC_{1.9}$ values lower than 0.74 and hydrothermal opals have $CRC_{1.9}$ values higher than 0.82. In this study, we observe that we can define a corrected threshold ranging from ~ 0.78-0.79 to ~ 0.90-0.91 by trying to take into account the anomalous results obtained on terrestrial opal-A and powder samples and the results of the experiment at Mars-relevant atmospheric pressure (Figure 14c). Chauviré et al. (2017a) also observed that hydrothermal opals have $CRC_{1.4}$ higher than 1.03 and weathering opals have $CRC_{1.4}$ lower than 0.96. In our case, we place a threshold at a $CRC_{1.4}$ ranging from ~ 0.88-0.89 to ~ 0.99-1.00 (Figure 14b) which is slightly lower, but still within the gap identified by Chauviré et al. (2017a). Overall, these thresholds are very close and the little observed variations can be explained by the measurement methods (transmission versus reflection), the samples used (only thin sections in Chauviré et al. (2017a) versus thin sections and powders with new samples of geyserites and volcanic products here, and because it was decided here to exclude some of their samples presenting additional absorption bands) and, also, the spectral resolutions (laboratory versus CRISM).

5.1.2. Hydration state and absorption bands

The ternary diagram in Figure 16 shows that the relative area of the 2.2 µm band increases jointly with a decrease in the relative contribution of the 1.9 µm absorption feature and that terrestrial varieties of hydrated silica are segmented along this trend depending on the type of silica: opal-CT, opal-A, chalcedony, and finally volcanic products. First, the more a variety of silica has an important contribution of molecular water, the lower the contribution of silanols is. Following the models of Boboň et al. (2011) and Sun (2017), it can be assumed that the more loaded in molecular water the silica is, the more this water will interfere with the other water-related species like the underlying silanol groups. This can be verified by the segmentation of the different types of silica in the diagram. Generally, opal-CT is more likely to incorporate water molecules in its structure made of

lepispheres than opal-A which is made of disordered network of silica spheres (e.g. Langer and Florke, 1974; Chauviré et al., 2017a). Frequently, opal-A has 2.2 µm absorption features that are more pronounced than those of opal-CT that sometimes shows weak or almost absent 2.2 µm bands (Figure 1). Likewise, opals are also more hydrated than chalcedony with water content up to 15 %, against not more than 1-2 % for the latter (Flörke et al., 1982; Adams et al., 1991). Again, we observe that chalcedony samples have 2.2 µm absorption bands that are often more pronounced than opal-A (Figure 1). Volcanic glasses have highly variable water content (e.g. Di Genova et al., 2017), but generally lower than 1-2 % for obsidians if not too altered (e.g. Stevenson and Novak, 2011). In these samples, the 1.9 µm absorption band is often low or absent, while the 2.2 µm absorption band is well visible in the spectra. Ultimately, the trend that is observable in the ternary diagram could be considered as a continuum of hydration and/or dehydration. Silica species are distinguished by the contributions of their absorption bands according to hydration behavior, itself depending on the microcrystalline structure of the silica. This apparent (de)hydration trend is verified by the results of the NIR analysis at Mars-relevant atmospheric pressure. Indeed, the two samples FT1111 and VTB that dehydrate at low atmospheric pressure, have shifted in the ternary diagram along this trend. In addition, they have moved apart from the opal-CT cluster toward the chalcedony cluster, and hence, from highly hydrated silica varieties to species that are less hydrated (normally under ambient atmospheric pressure) (Figure 16).

5.2. Spectral investigation of the hydrated silica on Mars

5.2.1. Applicability of spectral criteria to CRISM data

Silica dehydration under the thin martian atmosphere may affect the silica spectra and the applied criteria. Laboratory experiments have shown that silica dehydration is marked by the loss of water molecules and a relative increase in silanol content (e.g. Milliken et al., 2008; Rice et al., 2013; Smith et al., 2013; Sun and Milliken, 2018). Spectrally, it causes the decrease of the 1.9 µm absorption band intensity, the disappearance of the 1.46-1.96-2.26 µm contributions related to hydrogen bonding, a shift shorter wavelength of the 1.4- and 1.9 µm minima, and a relative increase of the 2.2 µm absorption band related to silanol groups (e.g. Milliken et al., 2008; Rice et al., 2013; Sun and Milliken, 2018).

In the present NIR measurements under a Mars-like atmospheric pressure, we observed that the silica dehydration is not systematic, as only two opal-CT have dehydrated significantly. For these two, the dehydration involved spectral changes that have subsequently affected the spectral criteria calculations. These changes are evidenced by a decrease in the CRC values of the absorption features as the dehydration is followed by the weakening of the hydrogen bonding contributions. It is also represented by a shift to shorter

wavelengths of the band minima on the three absorption bands (Figure 13). These observations are in agreement with the previous studies that have investigated the impacts of silica dehydration on spectral features (e.g. Milliken et al., 2008; Rice et al., 2013; Sun, 2017; Sun and Milliken, 2018). Note that these previous studies observed dehydration in all type of opal (Rice et al., 2013; Sun, 2017; Sun and Milliken, 2018). The apparent increased dehydration in previous studies can be explained by the preparation of the samples. Here, we mainly analyzed samples as thin sections, whereas they were hand ground in others. The grinding affects the effective porosity and enhanced significantly the dehydration as shown by thermal analysis (Smallwood et al., 2008; Thomas et al., 2007) and the Curiosity rover observations (Rapin et al., 2018). Moreover, Sun (2017) and Sun and Milliken (2018) performed low-pressure experiments at a much lower atmospheric pressure (0.016 mbar) than the Mars' mean atmospheric pressure, which then can artificially increase the dehydration of hydrated silica.

Nevertheless, even if the spectral criteria are affected by the silica dehydration, this requires some modifications of the thresholds between opal-A/opal-CT and weathering/hydrothermal opals. The major fields defined in the figures 12,14 become narrower when the silica is affected by dehydration processes under a Mars-like atmospheric pressure. However, if we compare these major fields with the CRISM martian data, we observe that they are still plotted within the same fields and that only few CRISM detections are located in the areas of uncertainty discussed in section 4.2 (Figure 15). It can be noted that the sampling set for low-pressure experiment does not include hydrothermal opal-A sample (Table 5). However, the analyses of our samples at low-pressure shows that, even if their CRC values lower, it does not modify the geological field (weathering/hydrothermal) to which they are associated. This trend suggests that additional hydrothermal opal-A might behave similarly, or that they should end up in the areas of uncertainty in gray. This should be verified on a larger number of samples, but this first approach still validates the application of these criteria. Thus, the application of these spectral criteria to the martian data still remains valid and workable by looking at the main trends in order to obtain additional information on the type of silica, its hydration state and the putative geological origins.

5.2.2. Geomorphological contexts and spectral criteria

The combinations of the reflectance band minima criterion with the CRC applied to the martian CRISM data show that hydrated silica-bearing aeolian deposits are closer to the hydrothermal terrestrial opal-CT field both on the 1.4 and 1.9 µm absorption features, whereas these criteria mostly place the hydrated silica-bearing bedrock deposits closer to the weathering terrestrial opal-A field (but in the terrestrial weathering opal-CT field on the 1.9 µm absorption band) (Figure 15b,c). From these results, we can assume that the hydrated silica-

bearing aeolian deposits contain silica that is more crystalline and/or more hydrated than the silica detected in the hydrated silica-bearing bedrock (see hydration/crystallinity related shifts of their band minima in Figure 7) (Sun and Milliken, 2018). The relative area values of the martian hydrated silica-bearing aeolian deposits are close to the terrestrial chalcedony values, which confirms that these aeolian deposits consist of rather crystalline and hydrated silica. At the opposite, relative area values of the martian hydrated silica-bearing bedrock deposits are much closer to terrestrial volcanic product values, which confirms that these indurated bedrock deposits consist of rather amorphous and relatively dehydrated silica (see hydration/crystallinity related shifts of their band minima in Figure 7). Interestingly, terrestrial volcanic products and martian hydrated silica-bearing bedrock, in addition to being close in the ternary diagram (Figure 16), possess very similar CRC values and band minima on both the 1.4 and 1.9 µm absorption features. The fact that their minima on the 1.9 µm band are inconsistent with their minima on the 1.4 µm band is a significant observation to suggest that the hydrated silica-bearing bedrock deposits could be volcanic products, like altered volcanic glasses and/or altered ashes as it has been suggested by several authors (e.g. Milliken et al., 2008; Smith et al., 2013). However, this does not reject the possibility that these deposits are opal-A-rich.

Sun and Milliken (2018) also observed more crystalline hydrated silica in aeolian deposits and have suggested that these deposits likely experienced longer water-rock interactions compared to the bedrock deposits. They proposed two hypotheses to explain why the hydrated silica-bearing aeolian deposits are more crystalline and/or hydrated than the bedrock deposits. First, they proposed that the amorphous silica-bearing bedrock could have undergone diagenetic transformations into more crystalline silica but that subsequent erosion could have removed this more crystalline silica to leave a fresh surface enriched in amorphous silica. In this sense, silica in bedrock deposits could be younger silica exposures that have not had sufficient time to convert to more crystalline silica. Their second hypothesis suggests that the hydrated silica-bearing aeolian deposits are more crystalline and/or hydrated because of their particulate structure that involved a greater porosity. This available surface could have favored prolonged interactions with surface water and/or water vapor, which would explain why these aeolian deposits are more crystalline and/or hydrated than the bedrock deposits. By assuming that all martian hydrated silica was at first opal-A, Sun and Milliken (2018) hypothesized that this particulate structure of hydrated silica-bearing aeolian deposits has allowed them to be converted into opal-CT. Hydrated silica-bearing bedrocks, having a lower porosity, and therefore a lower surface of contact with the atmospheric agents, would have experienced less transformation to more crystalline silica.

Another possible explanation is to invoke impact-induced hydrothermal activity as a process involved in the formation of the hydrated silica in the aeolian deposits. In our study, these hydrated silica-bearing aeolian deposits (Antoniadi crater, Elorza crater and Iani Chaos silica) are always detected around central peaks and/or

within pits of impact craters with diameters of several tens of kilometers. Craters of this size can easily develop post-impact hydrothermal systems lasting thousands of years (Osinski et al., 2013 and reference therein). Therefore this hydrated silica could have been formed within these craters by impact-induced hydrothermal activity, which would be consistent with the high-CRC of these deposits that are close to CRC values of terrestrial hydrothermal opals. Finally, to justify that such materials are found in particulate aeolian deposits, it is possible that they are the erosional products of impact melts, uplifted bedrock or impact breccias that were previously altered by hydrothermal fluids (e.g. Smith and Bandfield, 2012).

5.2.3. Hydrothermal vs weathering martian hydrated silica

In the Aeolis Mensae and Camichel crater sites, hydrated silica is the only hydrous mineral detected within distal parts of intra-crater fan delta or alluvial fans which form the terminal parts of sapping valleys (Popa et al., 2010, 2012; Carter et al., 2012; Hauber et al., 2013; Pan et al., 2019) (Figure 3). This hydrated silica, possibly occurring as coatings or silcretes is likely to have formed *in-situ* by short-lived aqueous processes, mostly under superficial acidic conditions during the Hesperian period for the Aeolis Mensae fans and during the Amazonian period for the Camichel crater delta (Carter et al., 2012; Hauber et al., 2013; Pan et al., 2019). Our spectral criteria are in agreement with this hypothesis as hydrated silica spectra exhibit low CRC values that argue in favor of a weathering origin, and low band minima suggesting an amorphous structure. Also, one detection is located near the ejecta of a nearby crater, east of one of the two alluvial fans selected In the Aeolis Mensae region (Figure 3c). Thus, it is possible that this silica consists of impact glasses that were altered by similar surficial processes and at the same time the alluvial fan had formed. In the case of the Camichel crater fan delta, other studies suggest that this hydrated silica was formed by hydrothermal processes that have led to the formation of sinter-like structures (Popa et al., 2010, 2012). Because no mineral indicator of high-temperature alteration processes has been detected on these two sites, because the geomorphogical contexts are associated to surficial sedimentary processes, and according to the spectral criteria developed in this study, we do not favor a hydrothermal origin for the Aeolis Mensae and Camichel crater hydrated silica.

The hydrated silica of the Nilosyrtis Mensae region is present at the base of stratified deposits at the outlet of a valley (Amador and Bandfield, 2016). These stratified sedimentary deposits are part of a larger sedimentary complex. The Nilosyrtis Mensae hydrated silica has low CRC values suggesting a weathering origin. Other hydrous minerals such as Fe/Mg-smectites and Mg-carbonates are also detected in this site with hydrated silica, and are suggested to have formed through low temperature weathering processes (Amador and Bandfield, 2016). The geomorphological context and the ancillary detected minerals do not suggest high-

temperature processes. Our spectral criteria on Nilosyrtis Mensae hydrated silica are consistent with the hypotheses and observations described above, and hence with a weathering origin.

The Ius Chasma site is part of the Valles Marineris plateau region that hosts many regional alteration profiles where Mars Express and Mars Reconnaissance Orbiter spacecrafts have detected, bottom to top in stratigraphy, Fe/Mg-phyllosilicates, Al-phyllosilicates, sulfates and hydrated silica (e.g. Mangold et al., 2008; Milliken et al., 2008; Roach et al., 2010; Weitz et al., 2010; Le Deit et al., 2012; Carter et al., 2015; Loizeau et al., 2018). The Ius Chasma hydrated silica has low CRC values and low band minima suggesting weathering amorphous silica. Although studies suggest that hydrated silica of Valles Marineris could have been formed by hydrothermal processes during the Hesperian (Bishop et al., 2009; Flahaut et al., 2010), most of the studies suggest that they have formed mostly during the Hesperian or maybe during the Amazonian by low-temperature acidic weathering (Milliken et al., 2008; Roach et al., 2010; Weitz et al., 2010; Le Deit et al., 2010, 2012; Wendt et al., 2011; Smith et al., 2013; Weitz and Bishop, 2016). It has been suggested that the plateaus around Valles Marineris are constituted of pedogenetic profiles where Al-phyllosilicates, sulfates and hydrated silica overlie Fe/Mg-smectites (Le Deit et al., 2012; Carter et al., 2015; Weitz and Bishop, 2016; Loizeau et al., 2018). All these studies also suggest that this hydrated silica could be the product of surface weathering acidic alteration of volcanic ash or hydrated glass that possibly formed during the Hesperian or Amazonian periods, which is in accordance with the amorphous phase indicated by the low band minima (Milliken et al., 2008; Weitz et al., 2010; Le Deit et al., 2010, 2012; Wendt et al., 2011; Rice et al., 2013; Smith et al., 2013). Therefore, the calculated spectral criteria presented here support the previous interpretations of the weathering origin of the Valles Marineris' hydrated silica-bearing deposits.

The hydrated silica that is detected within the Antoniadi crater region is located in aeolian deposits in impact craters, mostly around their brecciated central peaks, where zeolites (analcime) and Fe/Mg-smectites or chlorites were also detected (Ehlmann et al., 2009; Smith and Bandfield, 2012). Previous studies suggest that these mineral assemblages are indicators of hydrothermal alteration processes under alkaline conditions, or other high-temperature geological processes in the subsurface (Ehlmann et al., 2009; Smith and Bandfield, 2012). Our CRC calculations are in agreement with the hydrothermal origin because Antoniadi crater hydrated silica detections display very high CRC values on both the 1.4 and 1.9 μm absorption features. The highly crystalline hydrated silica of Antoniadi crater could also be the product of diagenetic transformation of amorphous silica (Smith and Bandfield, 2012). This would be in agreement with the fact that these detections have relative areas of their absorption bands that are very close to the values of terrestrial chalcedony. In all cases, the spectral criteria suggest that the hydrated silica-bearing aeolian deposits of the Antoniadi crater region have experienced geological processes within the subsurface before the more recent processes of

erosion that remobilized them at the surface, which is in agreement with previous studies (Smith and Bandfield, 2012).

In the Elorza crater central uplift, hydrated silica is detected in two different geomorphological settings: as dehydrated silica in uplifted bedrock and as hydrated silica in aeolian deposits (Quantin et al., 2012; Sun and Milliken, 2015, 2018; Hopkins et al., 2017). All hypotheses concerning the hydrated silica genesis in Elorza crater involve impact-related processes at high temperatures like crater excavation of previous buried materials, post-impact hydrothermal alteration of silica-rich deposits or hydrated glass formed in relation with the crater impact event (Quantin et al., 2012; Sun and Milliken, 2015; Hopkins et al., 2017). The results of the concavity criteria applied on the hydrated silica detections of the Elorza crater uplift (both aeolian and bedrock silica) show high CRC values both on the 1.4 and 1.9 µm absorption bands, consistent with the previous assumptions made in the literature on its hydrothermal origin.

Thomas et al. (2017) reported the detection of hydrated silica signatures in the Iani Chaos area, but no interpretation about their origin has been proposed. Several studies have reported the detection of sulfates in light-toned layered deposits similar to the ones observed in Valles Marineris (Glotch and Rogers, 2007; Gilmore et al., 2010; Guallini et al., 2012; Sefton-Nash et al., 2012). These authors invoked cyclic sedimentary processes like evaporation of salty water in a lacustrine environment to explain the sulfates formation in Iani Chaos that possibly occurred during the Late Noachian or the Hesperian periods (Warner et al., 2011). Thus, it would seem reasonable to invoke a weathering origin for the hydrated silica detected by Thomas et al. (2017). However, The Iani Chaos detections are mostly associated with the spectral criteria values of the Antoniadi crater and Elorza crater detections with relatively high CRC values (though somewhat lower than Antoniadi and Elorza) and in association with terrestrial chalcedony in the ternary diagram, that represents the relative areas of the absorption bands. In addition, this hydrated silica detection is correlated with aeolian deposits that are located close to the central peak of an impact crater (Figure 4f,h). This geomorphological setting is reminiscent of the geomorphological context in which the Antoniadi hydrated silica is detected, which we interpreted as being of hydrothermal origin. Thus, our results suggest a hydrothermal origin for the Iani Chaos silica.

For the two Noctis Labyrinthus and Nili Patera sites, previous studies have proposed that the hydrated silica that is detected there was mainly formed through hydrothermal processes (e.g. Skok et al., 2010; Thollot et al., 2012). However, our spectral criteria mostly suggest that these deposits were formed in surface weathering contexts of alteration, which then contradicts the geomorphological contexts and the previous studies of these areas. The spectral criteria used here show that these silica deposits are amorphous and dehydrated as seen by the low minima and low CRC values both on the 1.4 and 1.9 µm absorption bands, which explains their spectral signatures that are close to terrestrial weathering opal-A. Also, the relative areas

calculations assimilate these hydrated silica deposits into terrestrial volcanic glasses like the other martian hydrated silica-bearing bedrock deposits.

Skok et al. (2010) presented hydrated silica detections in the Nili Patera caldera belonging to the Syrtis Major volcanic complex. This hydrated silica is located around the Nili Tholus cone, within light-toned patchy deposits with a domed geomorphologic shape (Figure 5). They are thought to represent remnants of a volcanically driven hydrothermal system (Skok et al., 2010). These sinter-like deposits probably had formed after the Hesperian and/or maybe during the Amazonian (Platz et al., 2014; Fawdon et al., 2015). The geomorphological observations predominantly favor that the hydrated silica-bearing Nili Patera deposits derived from geyser-like vent or fumaroles.

Several troughs in the Noctis Labyrinthus, region forming the western termination of Valles Marineris and located east of the Tharsis Mons, exhibit signatures of many classes of hydrated minerals including Fe/Mg-smectites, Al-phyllosilicates, sulfates and hydrated silica (Milliken et al., 2008; Weitz et al., 2010, 2011, 2013; Thollot et al., 2012). Those detections argue in favor of an intense aqueous activity through all the region during the Late Hesperian, and possibly during the Amazonian periods (Mangold et al., 2010a,b). Because Noctis Labyrinthus is close to volcanic provinces, the hypothesis that these hydrated minerals formed by hydrothermal alteration or volcanic ash-ice interactions was proposed (Mangold et al., 2010a). The association of hydrated silica and sulfates through the various depressions of Noctis Labyrinthus suggests that the hydrated silica formed by acid-sulfate solutions from heated groundwater and magmatic sulfurs that altered volcanic materials, possibly in the form of tephra or ash (Weitz et al., 2010, 2011; Thollot et al., 2012). However, occurrence of gypsum-bearing deposits above hydrated silica-bearing deposits have been suggested by Weitz et al. (2013) to have formed under acidic conditions at low temperature rather than in hydrothermal conditions.

Both for Nili Patera and Noctis Labyrinthus hydrated silica, the results of the spectral criteria suggest a weathering and/or “low temperature” origin and/or the occurrence of (highly?) dehydrated and/or amorphous silica, whereas all previous studies stated that these two sites have potentially encountered hydrothermal processes. To explain the inconsistencies between the spectral criteria and the hypothesized geological origins, several hypotheses are possible: (i) low-temperature hydrothermal processes like silica sinter precipitation, (ii) weathering of previously hydrothermally altered deposits, (iii) advanced dehydration of silica, (iv) low signal-to-noise ratio of the CRISM image in the Nili Patera case, and (v) occurrence of altered volcanic glasses only in the Noctis Labyrinthus case as the Nili Patera silica is likely to be a geyser-linked silica.

Post-depositional processes, like dehydration, surface leaching, reworking and/or early diagenesis could have changed the initial hydrothermal spectral signatures of the Nili Patera and Noctis Labyrinthus opal

deposits. The question of the thermal threshold between weathering and hydrothermal alteration needs to be further investigated on both Mars and Earth. Because geyserites and silica sinters are found within hydrothermal contexts, their CRC should have high values indicative of hydrothermal-like NIR signatures. However, fluid temperatures on geysers can vary temporally and spatially; generally warmer near the vents (> 80°C) and close to ambient temperatures near discharge aprons. Geyserites and silica sinters could thus experience variable temperature of formation that could influence their NIR signatures. Also, some opals can form under cryogenic conditions in contact with ice grains and/or snow, like in Iceland or within the Yellowstone Park, during the winter (Channing and Butler, 2007; Jones and Renaut, 2010; Fox-powell et al., 2018). We hypothesize that some geyserites and silica sinters may exhibit CRC values consistent with continental weathering or low-temperature hydrothermal processes (below 50°C) even if formed in hydrothermal setting. In this case, it is possible that some geyserites and silica sinters, consider as *sensu stricto* hydrothermal in origin, could have formed under low-temperature hydrothermal processes.

6. Conclusions and future work

This study demonstrates that spectral criteria [the Concavity-Ratio-Criterion (CRC) and band minimum position] developed on transmission measurements on terrestrial samples (Chauviré et al., 2017a) give comparable results when applied to reflectance measurements. We also observed that spectral measurements on terrestrial samples at martian-relevant atmospheric pressure give results slightly modified for some samples, but in such a manner that it does not change the interpretation of spectra on terrestrial samples. These spectral criteria can therefore be used on CRISM data in order to obtain additional information on the type of hydrated silica depositions on Mars and their geology.

On the terrestrial data resampled at CRISM resolution, band minimum positions are used to determine the type and the structure of silica (volcanic glasses, opal-A, opal-CT, chalcedony) both on the 1.4 and 1.9 µm absorption features (Langer and Florke, 1974; Boboň et al., 2011; Rice et al., 2013; Chauviré et al. 2017a; Sun, 2017; Sun and Milliken, 2018). Coupled to band shape measurements, quantified by the CRC (Chauviré et al., 2017a), spectral criteria distinguish between two main geological environments of formation: surface weathering alteration and hydrothermal alteration. Moreover, we emphasize that relative contributions (normalized areas) of each absorption band also allow distinguishing different types of silica (opal-CT, opal-A, chalcedony and volcanic glasses) according to their hydration behavior in a qualitative manner. Altogether, these criteria are able to give constraints on the origin and the variety of hydrated silica where the geological context is ambiguous.

The application of these spectral criteria to CRISM data coupled with HiRISE and CTX observations show that two main types of spectra can be distinguished, and these are consistent with two major geomorphological contexts on Mars proposed by Sun and Milliken (2018). First, hydrated silica-bearing bedrock deposits (e.g. alluvial fans, stratified deposits, etc.) consist of amorphous and/or dehydrated silica. Spectral criteria indicate that these detections correspond to dehydrated weathering opal-A or to altered volcanic glasses. Second, hydrated silica-bearing aeolian deposits (e.g. aeolian dunes and mega-ripples) are composed of more crystalline and/or hydrated silica that is associated with hydrothermal opal-CT or chalcedony. These hydrated silica-bearing aeolian deposits are often located around central peaks of impact craters. Therefore, impact-induced hydrothermal activity is likely the origin of hydrated silica formation in these aeolian deposits.

Overall, spectral criteria measured on our limited set of selected martian places are in agreement with most of the geological origins proposed in the literature (weathering sites: Aeolis Mensae, Camichel crater, Valles Marineris, Nilosyrtis Mensae; hydrothermal sites: Antoniadi crater, Elorza crater, Iani Chaos). Some differences between our results and the literature are however raised for sites like Noctis Labyrinthus and Nili Patera. These differences highlight that post-deposition processes may have modified the initial signature of these deposits or that they were formed by low-temperature hydrothermal activity. Further investigations will aim to better constrain the nature and origin of these hydrated silica detections, and the many other detections that we did not investigate yet. In addition, we plan to focus on additional terrestrial analogs to enlarge the dataset used as reference samples. NIR measurements, at terrestrial ambient and Mars-relevant conditions still need to be acquired on a larger suite of opal samples. These would include (not exhaustively): hydrated silica coatings from volcanically-derived acidic fluids at Kilauea Volcano, Hawaii (e.g. Minitti et al., 2007; Chemtob et al., 2010, Seelos et al., 2010), coatings in proglacial environments (e.g. Hallet, 1975; Rutledge et al., 2018), and more opal-A/CT samples of geyserites and silica sinters from various locations (from geyser vents to discharge aprons). One crucial point will be to examine carefully the effect of temperature of formation of hydrated silica on its spectroscopic properties in a single geological context. Do low temperature silica sinters or fumarolic acid alteration products show a hydrothermal-like or weathering-like NIR signature? Does the low temperature (< 50°C) diagenetic transformation of opal-A into opal-CT affect its NIR signature? How does early diagenesis affect spectral signature of opal? These are key questions that remain to be investigated in order to better constrain the use of such spectral criteria for geological interpretation of martian hydrated silica deposits.

The coming two in-situ space missions will send spectrometers to the surface of Mars: MicrOmega and Infrared Spectrometer for Mars (ISEM) for the ExoMars rover (ESA) and SuperCam for the Mars 2020 rover (NASA) (e.g. Fouchet et al., 2015; Pilorget and Bibring, 2013; Vago et al., 2017; Wiens et al., 2017). The application of our spectral criteria to the data collected by the rovers on hydrated silica, coupled with the

results of the other onboard instruments, will allow a better understanding of the geology in which in-situ detected silica formed (e.g. Pan et al., 2019; Tarnas et al., 2019). Altogether, in-situ and orbital analysis will provide a better understanding of Mars' aqueous geological history and hence better constraints on paleoclimatic and exobiological implications.

Acknowledgments

We thank the two reviewers of this manuscript, Steve Ruff and Vivian Z. Sun, for their numerous and constructive comments that helped strengthen this paper. We thank Laurent Lenta (LPG, Nantes) for his help in sample preparation. We thank Erwan Le Menn, Fabien Baron and Yann Morizet (LPG, Nantes) for their help and advice in NIR analysis of the samples. We also thank Eric Quirico, Olivier Brissaud and Pierre Beck (IPAGrenoble) for their help with FTIR analysis at Mars-relevant atmospheric pressure. We are grateful to Cristiano Ferraris (Muséum National d'Histoire Naturelle, Paris, France) for providing geyserites samples 104.258, 85.27, 46.170 and 24.349. We are also grateful to Antoine Bezos (LPG, Nantes) for providing volcanic glass and obsidian samples Gi1900, Obs_1, Obs_2, Obs_3, WD3, SO100-86DS, SO100-91DS, SO100-92DS, Shosho and the associated EMP data analysis. We acknowledge the support from the Agence Nationale de la Recherche (ANR, France) under the contract ANR-16-CE31-0012 entitled Mars-Prime, the Centre National d'Études Spatiales (CNES), and the Centre National de la Recherche Scientifique (CNRS, France).

References

Adams S.J. et al., (1991) A solid state 29Si nuclear magnetic resonance study of opal and other hydrous silicas, *Am. Mineral.* **76**, *1863–1871*,.

Amador E.S., Bandfield J.L., (2016) Elevated bulk-silica exposures and evidence for multiple aqueous alteration episodes in Nili Fossae, Mars, *Icarus* **276**, *39–51*,. https://doi.org/10.1016/j.icarus.2016.04.015

Anderson J.H., Wickersheim K.., (1964) Near infrared characterization of water and hydroxyl groups on silica surfaces, *Surf. Sci.* **2**, *252–260*,. https://doi.org/10.1016/0039-6028(64)90064-0

Arvidson R.E. et al., (2014) Ancient aqueous environments at endeavour crater, mars, *Science* **343**, *1–8*,. https://doi.org/10.1126/science.1248097

Bandfield J.L. et al., (2013) Extensive hydrated silica materials in western Hellas Basin, Mars, *Icarus* **226**, *1489–1498*,. https://doi.org/10.1016/j.icarus.2013.08.005

Bandfield J.L., (2008) High-silica deposits of an aqueous origin in western Hellas Basin, Mars, *Geophys. Res. Lett.* **35**, *1–5*,. https://doi.org/10.1029/2008GL033807

Banerjee A., Wenzel T., (1999) Black opal from Honduras, *Eur. J. Mineral.* **11**, *401–408*,. https://doi.org/10.1127/ejm/11/2/0401

Bibring J.P. et al., (2006) Global mineralogical and aqueous Mars history derived from OMEGA/Mars express data, *Science* **312**, *400–404*,. https://doi.org/10.1126/science.1122659

Bibring J.P. et al., (2005) Mars surface diversity as revealed by the OMEGA/Mars express observations, *Science* **307**, *1576–1581*,. https://doi.org/10.1126/science.1108806

Bishop J.L. et al., (2009) Mineralogy of Juventae Chasma: Sulfates in the light-toned mounds, mafic minerals in the bedrock, and hydrated silica and hydroxylated ferric sulfate on the plateau, *J. Geophys. Res. E Planets* **114**, *1–23*,. https://doi.org/10.1029/2009JE003352

Bishop J.L. et al., (2008) Phyllosilicate Diversity and Past Aqueous Activity Revealed at Mawrth Vallis, Mars, *Science* **321**, *830–833*,. https://doi.org/10.1126/science.1159699

Boboň M. et al., (2011) State of water molecules and silanol groups in opal minerals: A near infrared spectroscopic study of opals from Slovakia, *Phys. Chem. Miner.* **38**, *809–818*,. https://doi.org/10.1007/s00269-011-0453-0

Bohrmann G. et al., (1998) Hydrothermal activity at Hook Ridge in the Central Bransfield Basin, Antarctica, *Geo-Marine Lett.* **18**, *277–284*,. https://doi.org/10.1007/s003670050080

Botz R., Bohrmann G., (1991) Low-temperature opal-CT precipitation in Antarctic deep-sea sediments: evidence from oxygen isotopes, *Earth Planet. Sci. Lett.* **107**, *612–617*,. https://doi.org/10.1016/0012-821X(91)90105-Q

Buback M. et al., (2015) Near Infrared Absorption of Pure Carbon Dioxide up to 3100 bar and 500 K. II. Wavenumber Range 5600 cm-1 to 7400 cm-1, *Zeitschrift für Naturforsch. A* **41**, *505–511*,. https://doi.org/10.1515/zna-1986-0309

Carter J. et al., (2015) Widespread surface weathering on early Mars: A case for a warmer and wetter climate, *Icarus* **248**, *373–382*,. https://doi.org/10.1016/j.icarus.2014.11.011

Carter J. et al., (2013a) Hydrous minerals on Mars as seen by the CRISM and OMEGA imaging spectrometers: Updated global view, *J. Geophys. Res. E Planets* **118**, *831–858*,. https://doi.org/10.1029/2012JE004145

Carter J. et al., (2013b) Automated processing of planetary hyperspectral datasets for the extraction of weak mineral signatures and applications to CRISM observations of hydrated silicates on Mars, *Planet. Sp. Sci.* **76**, *53–67*,. https://doi.org/10.1016/j.pss.2012.11.007

Carter J. et al., (2012) Composition of alluvial fans and deltas on Mars, , in: 43rd Lunar Planet. Sci. Conf. p. 2.

Channing A., Butler I.B., (2007) Cryogenic opal-A deposition from Yellowstone hot springs, *Earth Planet. Sci. Lett.* **257**, *121–131*,. https://doi.org/10.1016/j.epsl.2007.02.026

Chauviré B. et al., (2019) Pedogenic origin of precious opals from Wegel Tena (Ethiopia): Evidence from trace elements and oxygen isotopes, *Appl. Geochemistry* **101**, *127–139*,. https://doi.org/10.1016/j.apgeochem.2018.12.028

Chauviré B. et al., (2017a) Near infrared signature of opal and chalcedony as a proxy for their structure and formation conditions, *Eur. J. Miner.* **29**, *409–421*,. https://doi.org/10.1127/ejm/2017/0029-2614

Chauviré B. et al., (2017b) The precious opal deposit at Wegel Tena, Ethiopia: Formation via successive pedogenesis events, *Can. Mineral.* **55**, *701–723*,. https://doi.org/10.3749/canmin.1700010

Chemtob S.M. et al., (2010) Silica coatings in the Ka'u Desert , Hawaii , a Mars analog terrain : A micromorphological, spectral, chemical, and isotopic study, *J. Geophys. Res.* **115**, *1–19*,. https://doi.org/10.1029/2009JE003473

Christy A.A., (2011) Near infrared spectroscopic characterisation of surface hydroxyl groups on hydrothermally treated silica gel, *Int. J. Chem. Environ. Eng.* **2**, *27 – 32*,.

Christy A.A., (2010) New insights into the surface functionalities and adsorption evolution of water molecules on silica gel surface: A study by second derivative near infrared spectroscopy, *Vib. Spectrosc.* **54**, *42–49*,. https://doi.org/10.1016/j.vibspec.2010.06.003

Clark B.C. et al., (2016) Esperance: Multiple episodes of aqueous alteration involving fracture fills and coatings at Matijevic Hill, Mars, *Am. Miner.* **101**, *1515–1526*,. https://doi.org/10.2138/am-2016-5575

Clark R.N. et al., (1987) Automatic Continuum Analysis of Reflectance Spectra, *JPL Proc. 3rd Airborne Imaging Spectrom. Data Anal. Work. 138–142*,.

Courtoy C.-P., (1957) Spectres de vibration-rotation de molecules simples diatomiques ou polyatomiques avec long parcours d'absorption. XII. Le spectre de C12O162 entre 3500 et 8000 cm-1 et les constantes moléculaires de cette molécule, *Can. J. Phys.* **35**, *608–648*,. https://doi.org/https://doi.org/10.1139/p57-068

Day R., Jones B., (2008) Variations in Water Content in Opal-A and Opal-CT from Geyser Discharge Aprons, *J. Sediment. Res.* **78**, *301–315*,. https://doi.org/10.2110/jsr.2008.030

Di Genova D. et al., (2017) Effect of iron and nanolites on Raman spectra of volcanic glasses: A reassessment of existing strategies to estimate the water content, *Chem. Geol.* **475**, *76–86*,. https://doi.org/10.1016/j.chemgeo.2017.10.035

Ehlmann B.L. et al., (2013) Geochemical consequences of widespread clay mineral formation in Mars' ancient crust, *Sp. Sci. Rev.* **174**, *329–364*,. https://doi.org/10.1007/s11214-012-9930-0

Ehlmann B.L. et al., (2011) Subsurface water and clay mineral formation during the early history of Mars, *Nature* **479**, *53–60*,. https://doi.org/10.1038/nature10582

Ehlmann B.L. et al., (2009) Identification of hydrated silicate minerals on Mars using MRO-CRISM: Geologic context near Nili Fossae and implications for aqueous alteration, *J. Geophys. Res. E Planets* **114**, *1–33*,. https://doi.org/10.1029/2009JE003339

Ehlmann B.L., Edwards C.S., (2014) Mineralogy of the Martian Surface, *Annu. Rev. Earth Planet. Sci.* **42**, *291–315*,. https://doi.org/10.1146/annurev-earth-060313-055024

Elmas N., Bentli I., (2013) Environmental and depositional characteristics of diatomite deposit, Alayunt Neogene Basin (Kutahya), West Anatolia, Turkey, *Environ. Earth Sci.* **68**, *395–412*,. https://doi.org/10.1007/s12665-012-1745-5

Elzea J.M., Rice S.B., (1996) TEM and X-ray diffraction evidence for cristobalite and tridymite stacking sequences in opal, *Clays Clay Miner.* **44**, *492–500*,. https://doi.org/10.1346/CCMN.1996.0440407

Fassett C.I., Head J.W., (2008) The timing of martian valley network activity: Constraints from buffered crater counting, *Icarus* **195**, *61–89*,. https://doi.org/10.1016/j.icarus.2007.12.009

Fawdon P. et al., (2015) The geological history of Nili Patera, Mars, *J. Geophys. Res. E Planets*. https://doi.org/10.1002/2015JE004795

Flahaut J. et al., (2010) Identification, distribution and possible origins of sulfates in Capri Chasma (Mars), inferred from CRISM data, *J. Geophys. Res. E Planets* **115**, *1–10*,. https://doi.org/10.1029/2009JE003566

Flörke O.W. et al., (1991) Nomenclature of mico- and non-crystalline silica minerals, based on structure and microstructure, *Neues Jahrb. für Mineral. - Abhandlungen* **163**, *19–42*,.

Flörke O.W. et al., (1982) Water in microcrystalline quartz of volcanic origin: Agates, *Contrib. to Mineral. Petrol.* **80**, *324–333*,. https://doi.org/10.1007/BF00378005

Fouchet T. et al., (2015) The Infrared Investigation on the SuperCam Instrument for the Mars2020 Rover, *46th Lunar Planet. Sci. Conf.* **2**, *2–3*,.

Fox-powell M.G. et al., (2018) Cryogenic silicification of microorganisms in hydrothermal fluids, *Earth Planet. Sci. Lett.* **498**, *1–8*,. https://doi.org/10.1016/j.epsl.2018.06.026

Freund S. et al., (2013) Oxygen isotope evidence for the formation of andesitic-dacitic magmas from the fast-spreading Pacific-Antarctic Rise by assimilation-fractional crystallisation, *Chem. Geol.* **347**, *271–283*,. https://doi.org/10.1016/j.chemgeo.2013.04.013

Friedman I., Long W., (1984) Volcanic glasses, their origins and alteration processes, *J. Non. Cryst. Solids* **67**, *127–133*,. https://doi.org/10.1016/0022-3093(84)90144-3

Frydenvang J. et al., (2017) Diagenetic silica enrichment and late-stage groundwater activity in Gale crater, Mars, *Geophys. Res. Lett.* **44**, *4716–4724*,. https://doi.org/10.1002/2017GL073323

Gaudin A. et al., (2011) Evidence for weathering on early Mars from a comparison with terrestrial weathering profiles, *Icarus* **216**, *257–268*,. https://doi.org/10.1016/j.icarus.2011.09.004

Geilert S. et al., (2016) Effect of diagenetic phase transformation on the silicon isotope composition of opaline sinter deposits of Geysir, Iceland, *Chem. Geol.* **433**, *57–67*,. https://doi.org/10.1016/j.chemgeo.2016.04.008

Giachetti T. et al., (2015) Discriminating secondary from magmatic water in rhyolitic matrix-glass of volcanic pyroclasts using thermogravimetric analysis, *Geochim. Cosmochim. Acta* **148**, *457–476*,. https://doi.org/10.1016/j.gca.2014.10.017

Gilmore M.S. et al., (2010) Sulfates in Iani Chaos, Mars, , in: 41st Lunar Planet. Sci. Conf. p. 2.

Glotch T.D., Rogers A.D., (2007) Evidence for aqueous deposition of hematite- and sulfate-rich light-toned layered deposits in Aureum and Iani Chaos, Mars, *J. Geophys. Res. E Planets* **112**, *1–11*,. https://doi.org/10.1029/2006JE002863

Goryniuk M.C. et al., (2004) The reflectance spectra of opal-A (0.5-25 μm) from the Taupo Volcanic Zone: Spectra that may identify hydrothermal systems on planetary surfaces, *Geophys. Res. Lett.* **31**, *1–4*,. https://doi.org/10.1029/2004GL021481

Graetsch H. et al., (1994) NMR, XRD and IR study on microcrystalline opals, *Phys. Chem. Miner.* **21**, *166–175*,. https://doi.org/10.1007/BF00203147

Graetsch H. et al., (1985) The nature of water in chalcedony and opal-C from brazilian agate geodes, *Phys. Chem. Miner.* **12**, *300–306*,. https://doi.org/10.1007/BF00310343

Greshake A. et al., (2010) Brownish inclusions and dark streaks in Libyan Desert Glass: Evidence for high-temperature melting of the target rock, *Meteorit. Planet. Sci.* **45**, *973–989*,. https://doi.org/10.1111/j.1945-5100.2010.01079.x

Guallini L. et al., (2012) Geologic and geomorphologic map of Iani Chaos (Mars), , in: 43rd Lunar Planet. Sci. Conf. p. 2.

Guidry S.A., Chafetz H.S., (2003) Anatomy of siliceous hot springs: Examples from Yellowstone National Park, Wyoming, USA, *Sediment. Geol.* **157**, *71–106*,. https://doi.org/10.1016/S0037-0738(02)00195-1

Haberle R.M. et al., (2017) The Atmosphere and Climate of Mars, *Cambridge University Press*, *Cambridge*, . https://doi.org/10.1017/9781139060172

Hallet B., (1975) Subglacial silica deposits, *Nature* **254**, *682–683*,.

Hauber E. et al., (2013) Asynchronous formation of Hesperian and Amazonian-aged deltas on Mars and implications for climate, *J. Geophys. Res. E Planets* **118**, *1529–1544*,. https://doi.org/10.1002/jgre.20107

Hein J.R. et al., (1978) Diagenesis of late Cenozoic diatomaceous deposits and formation of the bottom simulating reflector in the southern Bering Sea, *Sedimentology* **25**, *155–181*,. https://doi.org/10.1111/j.1365-3091.1978.tb00307.x

Herzig P.M. et al., (1988) Hydrothermal silica chimney fields in the Galapagos Spreading Center at 86°W, *Earth Planet. Sci. Lett.* **89**, *261–272*,. https://doi.org/10.1016/0012-821X(88)90115-X

Hopkins R.T. et al., (2017) The central uplift of Elorza Crater: Insights into its geology and possible relationships to the Valles Marineris and Tharsis regions, *Icarus* **284**, *284–304*,. https://doi.org/10.1016/j.icarus.2016.11.033

Hunt G.R., (1977) Spectral Signatures of Particulate Minerals in the Visible and Near Infrared, *Geophysics* **42**, *501–513*,. https://doi.org/10.1190/1.1440721

Hunt G.R., Salisbury J.W., (1970) Visible and near-infrared spectra of minerals and rocks: I. Silicate Minerals, *Mod. Geol.* **1**, *282–300*,.

Jones B. et al., (2007) The geological history of Geysir, Iceland: a tephrochronological approach to the dating of sinter, *J. Geol. Soc. London.* **164**, *1241–1252*,. https://doi.org/10.1144/0016-76492006-178

Jones B., Renaut R.W., (2010) Impact of Seasonal Changes on the Formation and Accumulation of Soft Siliceous Sediments on the Discharge Apron of Geysir, Iceland, *J. Sediment. Res.* **80**, *17–35*,.

https://doi.org/10.2110/jsr.2010.008

Jones B., Renaut R.W., (2007) Microstructural changes accompanying the opal-A to opal-CT transition: New evidence from the siliceous sinters of Geysir, Haukadalur, Iceland, *Sedimentology* **54**, *921–948*,. https://doi.org/10.1111/j.1365-3091.2007.00866.x

Jones B., Renaut R.W., (2003) Hot spring and geyser sinters: the integrated product of precipitation, replacement, and deposition, *Can. J. Earth Sci.* **40**, *1549–1569*,. https://doi.org/10.1139/e03-078

Jones J.B., Segnit E.R., (1971) The Nature of Opal. I. Nomenclature and Constituent Phases, *J. Geol. Soc. Aust.* **18**, *57–68*,. https://doi.org/https://doi.org/10.1080/00167617108728743

Jones J.B., Segnit E.R., (1969) Water in sphere-type opal, *Miner. Mag.* **37**, *357–361*,. https://doi.org/10.1180/minmag.1969.037.287.07

Kano K., (1983) Ordering of Opal-CT in diagenesis, *Geochem. J.* **17**, *87–93*,. https://doi.org/10.2343/geochemj.17.87

Kelloway S.J. et al., (2010) Assessing the viability of portable Raman spectroscopy for determining the geological source of obsidian, *Vib. Spectrosc.* **53**, *88–96*,. https://doi.org/10.1016/j.vibspec.2010.02.006

Lalou C. et al., (1984) Les dépôts hydrothermaux de la Dorsale Est-Pacifique: radiochronologie des sulfures et géochimie isotopique des dépôts de silice, *Bull. la Soc. Geol. Fr.* **S7**-**XXVI**, *9–14*,. https://doi.org/10.2113/gssgfbull.S7-XXVI.1.9

Langer K., Florke O.W., (1974) Near infrared absorption spectra (4000-9000 cm-1) of opals and the role of “water” in these SiO2.nH2O minerals, *Fortschritte der Mineral.* **52**, *17–51*,.

Le Deit L. et al., (2012) Extensive surface pedogenic alteration of the Martian Noachian crust suggested by plateau phyllosilicates around Valles Marineris, *J. Geophys. Res. E Planets* **117**, *1–25*,. https://doi.org/10.1029/2011JE003983

Le Deit L. et al., (2010) Morphology, stratigraphy, and mineralogical composition of a layered formation covering the plateaus around Valles Marineris, Mars: Implications for its geological history, *Icarus* **208**, *684–703*,. https://doi.org/10.1016/j.icarus.2010.03.012

Loizeau D. et al., (2018) Quantifying widespread aqueous surface weathering on Mars: The plateaus south of Coprates Chasma, *Icarus* **302**, *451–469*,. https://doi.org/10.1016/j.icarus.2017.11.002

Loizeau D. et al., (2012) Chronology of deposition and alteration in the Mawrth Vallis region, Mars, *Planet. Sp. Sci.* **72**, *31–43*,. https://doi.org/10.1016/j.pss.2012.06.023

Loizeau D. et al., (2007) Phyllosilicates in the Mawrth Vallis region of Mars, *J. Geophys. Res. E Planets* **112**, *1–20*,. https://doi.org/10.1029/2006JE002877

Maia M. et al., (2001) Contrasted interactions between plume, upper mantle, and lithosphere: Foundation chain case, *Geochemistry, Geophys. Geosystems* **2**, *29*,. https://doi.org/10.1029/2000GC000117

Malin M.C. et al., (2007) Context Camera Investigation on board the Mars Reconnaissance Orbiter, *J. Geophys. Res. E Planets* **112**, *1–25*,. https://doi.org/10.1029/2006JE002808

Mangold N. et al., (2012) The origin and timing of fluvial activity at Eberswalde crater, Mars, *Icarus* **220**, *530–551*,. https://doi.org/10.1016/j.icarus.2012.05.026

Mangold N. et al., (2010) A Late Amazonian alteration layer related to local volcanism on Mars, *Icarus* **207**, *265–276*,. https://doi.org/10.1016/j.icarus.2009.10.015

Mangold N. et al., (2008) Spectral and geological study of the sulfate-rich region of West Candor Chasma, Mars, *Icarus* **194**, *519–543*,. https://doi.org/10.1016/j.icarus.2007.10.021

Mangold N. et al., (2007) Mineralogy of the Nili Fossae region with OMEGA/Mars Express data: 2. Aqueous alteration of the crust, *J. Geophys. Res. E Planets* **112**, *1–25*,. https://doi.org/10.1029/2006JE002835

Marzo G.A. et al., (2010) Evidence for Hesperian impact-induced hydrothermalism on Mars, *Icarus* **208**, *667–683*,. https://doi.org/10.1016/j.icarus.2010.03.013

McEwen A.S. et al., (2007) Mars reconnaissance orbiter's high resolution imaging science experiment (HiRISE), *J. Geophys. Res. E Planets* **112**, *1–40*,. https://doi.org/10.1029/2005JE002605

McGuire P.C. et al., (2009) An improvement to the volcano-scan algorithm for atmospheric correction of CRISM and OMEGA spectral data, *Planet. Sp. Sci.* **57**, *809–815*,. https://doi.org/10.1016/j.pss.2009.03.007

McKeown N.K. et al., (2011) Interpretation of reflectance spectra of clay mineral-silica mixtures:Implications for Martian clay mineralogy at Mawrth Vallis, *Clays Clay Miner.* **59**, *400–415*,. https://doi.org/10.1346/CCMN.2011.0590404

McKeown N.K. et al., (2009) Characterization of phyllosilicates observed in the central Mawrth Vallis region, Mars, their potential formational processes, and implications for past climate, *J. Geophys. Res. E Planets* **114**, *1–20*,. https://doi.org/10.1029/2008JE003301

Miehe G. et al., (1984) Crystal structure and growth fabric of length-fast chalcedony, *Phys. Chem. Miner.* **10**, *197–199*,. https://doi.org/10.1007/BF00309311

Milliken R.E. et al., (2014) Wind-blown sandstones cemented by sulfate and clay minerals in Gale Crater, Mars, *Geophys. Res. Lett.* **41**, *1149–1154*,. https://doi.org/10.1002/2013GL059097

Milliken R.E. et al., (2008) Opaline silica in young deposits on Mars, *Geology* **36**, *847–850*,. https://doi.org/10.1130/G24967A.1

Minitti M.E. et al., (2007) Morphology, chemistry, and spectral properties of Hawaiian rock coatings and implications for Mars, *J. Geophys. Res. E Planets* **112**, *1–24*,. https://doi.org/10.1029/2006JE002839

Morris R. V et al., (2016) Silicic volcanism on Mars evidenced by tridymite in high-SiO2 sedimentary rock at Gale crater, *Proc. Natl. Acad. Sci.* **113**, *7071–7076*,. https://doi.org/10.1073/pnas.1607098113

Morrison G.W., (1980) Characteristics and tectonic setting of the shoshonite rock association, *Lithos* **13**, *97–108*,. https://doi.org/https://doi.org/10.1016/0024-4937(80)90067-5

Murata K.J., Randall R.G., (1975) Silica mineralogy and structure of the Monterey Shale, Temblor Range, California, *J. Res. U.S. Geol. Surv.* **3**, *567–572*,.

Murchie S. et al., (2007) Compact Connaissance Imaging Spectrometer for Mars (CRISM) on Mars Reconnaissance Orbiter (MRO), *J. Geophys. Res. E Planets* **112**, *1–57*,. https://doi.org/10.1029/2006JE002682

Murchie S.L. et al., (2009) Compact Reconnaissance Imaging Spectrometer for Mars investigation and data set from the Mars Reconnaissance Orbiter's primary science phase, *J. Geophys. Res. E Planets* **114**, *1–15*,. https://doi.org/10.1029/2009JE003344

Mustard J.F. et al., (2008) Hydrated silicate minerals on Mars observed by the Mars Reconnaissance Orbiter CRISM instrument, *Nature* **454**, *305–309*,. https://doi.org/10.1038/nature07097

Nagase T., Akizuki M., (1997) Texture and Structure of Opal-Ctand in Volcanic Rocks, *Can. Mineral.* **35**, *947–958*,.

Noe Dobrea E.Z. et al., (2010) Mineralogy and stratigraphy of phyllosilicate-bearing and dark mantling units in the greater Mawrth Vallis/west Arabia Terra area: Constraints on geological origin, *J. Geophys. Res.* **115**, *E00D19*,. https://doi.org/10.1029/2009JE003351

Osinski G.R. et al., (2013) Impact-generated hydrothermal systems on Earth and Mars, *Icarus* **224**, *347–363*,. https://doi.org/10.1016/j.icarus.2012.08.030

Ostrooumov M. et al., (1999) Spectres Raman des opales: aspect diagnostique et aide à la classification, *Eur. J. Miner.* **11**, *899–908*,.

Pan L. et al., (2019) Hydrated Silica in Martian Alluvial Fans and Deltas, , in: Ninth International Conference on Mars 2019.

Pilorget C., Bibring J.P., (2013) NIR reflectance hyperspectral microscopy for planetary science: Application to the MicrOmega instrument, *Planet. Space Sci.* **76**, *42–52*,. https://doi.org/10.1016/j.pss.2012.11.004

Pirajno F., (2009) Hydrothermal Processes and Mineral Systems, *Springer*, *Berlin*, . https://doi.org/10.1007/978-1-4020-8613-7

Platz T. et al., (2014) Amazonian volcanic activity at the Syrtis Major volcanic province, Mars, *45th Lunar Planet. Sci. Conf. 2*,.

Popa C. et al., (2012) Evidences of possible hydrothermal alteration in Xanthe Terra: Implications for surface water on Early Mars, *43rd Lunar Planet. Sci. Conf. 2*,.

Popa C. et al., (2010) New landing site proposal for Mars Science Laboratory (MSL) in Xanthe Terra, , in: 41st Lunar Planet. Sci. Conf. p. 2.

Quantin C. et al., (2012) Composition and structures of the subsurface in the vicinity of Valles Marineris as revealed by central uplifts of impact craters, *Icarus* **221**, *436–452*,. https://doi.org/10.1016/j.icarus.2012.07.031

Rapin W. et al., (2018) In situ analysis of opal in Gale crater, Mars, *J. Geophys. Res. Planets* **123**, *1–18*,. https://doi.org/10.1029/2017JE005483

Rey P.F., (2013) Opalisation of the Great Artesian Basin (central Australia): an Australian story with a Martian twist, *Aust. J. Earth Sci.* **60**, *291–314*,. https://doi.org/https://doi.org/10.1080/08120099.2013.784219

Rice M.S. et al., (2013) Reflectance spectra diversity of silica-rich materials: Sensitivity to environment and implications for detections on Mars, *Icarus* **223**, *499–533*,. https://doi.org/10.1016/j.icarus.2012.09.021

Roach L.H. et al., (2010) Hydrated mineral stratigraphy of Ius Chasma, Valles Marineris, *Icarus* **206**, *253–268*,. https://doi.org/10.1016/j.icarus.2009.09.003

Rodgers K.A. et al., (2004) Silica phases in sinters and residues from geothermal fields of New Zealand, *Earth-Science Rev.* **66**, *1–61*,. https://doi.org/10.1016/j.earscirev.2003.10.001

Rondeau B. et al., (2012) Geochemical and petrological characterization of gem opals from Wegel Tena, Wollo, Ethiopia: opal formation in an Oligocene soil, *Geochemistry Explor. Environ. Anal.* **12**, *93–104*,. https://doi.org/10.1144/1467-7873/10-MINDEP-058

Ruff S.W. et al., (2011) Characteristics, distribution, origin, and significance of opaline silica observed by the Spirit rover in Gusev crater, Mars, *J. Geophys. Res. E Planets* **116**. https://doi.org/10.1029/2010JE003767

Ruff S.W., Farmer J.D., (2016) Silica deposits on Mars with features resembling hot spring biosignatures at El Tatio in Chile, *Nat. Commun.* **7**, *1–10*,. https://doi.org/10.1038/ncomms13554

Rutledge A.M. et al., (2018) Silica Dissolution and Precipitation in Glaciated Volcanic Environments and Implications for Mars, *Geophys. Res. Lett.* **45**, *1–11*,. https://doi.org/10.1029/2018GL078105

Savitzky A., Golay M.J.E., (1964) Smoothing and Differenciation of Data by Simplified Least Squares Procedures, *Anal. Chem.* **36**, *1627–1639*,. https://doi.org/10.1021/ac60214a047

Seelos F.P. et al., (2011) CRISM data processing and analysis products update - Calibration, correction and visualization, *42nd Lunar Planet. Sci. Conf. 1–2*,.

Seelos K.D. et al., (2010) Silica in a Mars analog environment : Ka'u Desert , Kilauea Volcano , Hawaii, *J. Geophys. Res.* **115**, *1–18*,. https://doi.org/10.1029/2009JE003347

Sefton-Nash E. et al., (2012) Topographic, spectral and thermal inertia analysis of interior layered deposits in Iani Chaos, Mars, *Icarus* **221**, *20–42*,. https://doi.org/10.1016/j.icarus.2012.06.036

Sharp R.P., Malin M.C., (1975) Channels on Mars, *Bull. Geol. Soc. Am.* **86**, *593–609*,. https://doi.org/10.1130/0016-7606(1975)86<593:COM>2.0.CO;2

Skok J.R. et al., (2010) Silica deposits in the Nili Patera caldera on the Syrtis Major volcanic complex on Mars, *Nat. Geosci.* **3**, *838–841*,. https://doi.org/10.1038/ngeo990

Smallwood A.G. et al., (2008) Characterisation of the dehydration of australian sedimentary and volcanic previous opal by thermal methods, *J. Therm. Anal. Calorim.* **92**, *91–95*,. https://doi.org/10.1007/s10973-007-8742-z

Smallwood A.G. et al., (1997) Characterisation of sedimentary opals by Fourier transform Raman spectroscopy, *Spectrochim. Acta Part A Mol. Biomol. Spectrosc.* **53**, *2341–2345*,. https://doi.org/10.1016/S1386-1425(97)00174-1

Smith M.R. et al., (2013) Hydrated silica on Mars: Combined analysis with near-infrared and thermal-infrared spectroscopy, *Icarus* **223**, *633–648*,. https://doi.org/10.1016/j.icarus.2013.01.024

Smith M.R., Bandfield J.L., (2012) Geology of quartz and hydrated silica-bearing deposits near Antoniadi Crater, Mars, *J. Geophys. Res. E Planets* **117**, *1–24*,. https://doi.org/10.1029/2011JE004038

Squyres S.W. et al., (2008) Detection of Silica-Rich Deposits on Mars, *Science* **320**, *1063–1067*,. https://doi.org/10.1126/science.1155429

Stamatakis M.G., (1989) Authigenic silicates and silica polymorphs in the Miocene saline- alkaline deposits of the Karlovassi Basin, Samos, Greece, *Econ. Geol.* **84**, *788–798*,. https://doi.org/10.2113/gsecongeo.84.4.788

Steinier J. et al., (1972) Comments on Smoothing and Differentiation of Data by Simplified Least Square Procedure, *Anal. Chem.* **44**, *1906–1909*,. https://doi.org/10.1021/ac60319a045

Stevenson C.M., Novak S.W., (2011) Obsidian hydration dating by infrared spectroscopy: Method and calibration, *J. Archaeol. Sci.* **38**, *1716–1726*,. https://doi.org/10.1016/j.jas.2011.03.003

Sun V.Z., (2017) Clays and Opals on Mars : Implications for Water-Rock Interactions Through Time, *Brown University*, . https://doi.org/10.7301/Z08G8J58

Sun V.Z. et al., (2016) Hydrated silica on Mars: Relating geologic setting to degree of hydration, crystallinity, and maturity through coupled orbital and laboratory studies, *47th Lunar Planet. Sci. Conf. 2*,.

Sun V.Z., Milliken R.E., (2018) Distinct Geologic Settings of Opal-A and More Crystalline Hydrated Silica on Mars, *Geophys. Res. Lett.* https://doi.org/10.1029/2018GL078494

Sun V.Z., Milliken R.E., (2015) Ancient and recent clay formation on Mars as revealed from a global survey of hydrous minerals in crater central peaks, *J. Geophys. Res. Planets* **120**, *2293–2332*,. https://doi.org/10.1002/2015JE004918

Tarnas J.D. et al., (2019) Orbital Identification of Hydrated Silica in Jezero Crater, Mars, *Geophys. Res. Lett.* **46**, *1–12*,. https://doi.org/10.1029/2019GL085584

Thiry M. et al., (2006) Interpretation of palaeoweathering features and successive silicifications in the Tertiary regolith of inland Australia, *J. Geol. Soc. London.* **163**, *723–736*,. https://doi.org/10.1144/0014-764905-020

Thiry M., Millot G., (1987) Mineralogical Forms of Silica and their Sequence of Formation in Silcretes, *SEPM J. Sediment. Res.* **Vol. 57**, *343–352*,. https://doi.org/10.1306/212F8B25-2B24-11D7-8648000102C1865D

Thiry M., Milnes A.R., (1991) Pedogenic and Groundwater Silcretes at Stuart Creek Opal Field, South Australia, *J. Sediment. Res.* **61**, *111–127*,. https://doi.org/10.1306/D426769F-2B26-11D7-8648000102C1865D

Thollot P. et al., (2012) Most Mars minerals in a nutshell: Various alteration phases formed in a single environment in Noctis Labyrinthus, *J. Geophys. Res. E Planets* **117**, *1–28*,. https://doi.org/10.1029/2011JE004028

Thomas P.S. et al., (2013) Low temperature DSC characterisation of water in opal, *J. Therm. Anal. Calorim.* **113**, *1255–1260*,. https://doi.org/10.1007/s10973-012-2911-4

Thomas P.S. et al., (2007) Estimation of the diffusion coefficient of water evolved during the non-isothermal dehydration of Australian sedimentary opal, *J. Therm. Anal. Calorim.* **88**, *231–235*,. https://doi.org/10.1007/s10973-006-8133-x

Thomas R.J. et al., (2017) Widespread exposure of Noachian phyllosilicates in the Margaritifer region of Mars: Implications for paleohydrology and astrobiological detection, *J. Geophys. Res. Planets* **122**, *483–500*,. https://doi.org/10.1002/2016JE005183

Tobler D.J. et al., (2008) In-situ grown silica sinters in Icelandic geothermal areas, *Geobiology* **6**, *481–502*,. https://doi.org/10.1111/j.1472-4669.2008.00179.x

Tosca N.J., Knoll A.H., (2009) Juvenile chemical sediments and the long term persistence of water at the surface of Mars, *Earth Planet. Sci. Lett.* **286**, *379–386*,. https://doi.org/10.1016/j.epsl.2009.07.004

Vago J.L. et al., (2017) Habitability on Early Mars and the Search for Biosignatures with the ExoMars Rover, *Astrobiology* **17**, *471–510*,. https://doi.org/10.1089/ast.2016.1533

Warner N.H. et al., (2011) Constraints on the origin and evolution of Iani Chaos, Mars, *J. Geophys. Res. E Planets* **116**, *1–29*,. https://doi.org/10.1029/2010JE003787

Weitz C.M. et al., (2013) Gypsum, opal, and fluvial channels within a trough of noctis labyrinthus, mars: Implications for aqueous activity during the late hesperian to amazonian, *Planet. Sp. Sci.* **87**, *130–145*,. https://doi.org/10.1016/j.pss.2013.08.007

Weitz C.M. et al., (2011) Diverse mineralogies in two troughs of Noctis Labyrinthus, Mars, *Geology* **39**, *899–902*,. https://doi.org/10.1130/G32045.1

Weitz C.M. et al., (2010) Mars Reconnaissance Orbiter observations of light-toned layered deposits and associated fluvial landforms on the plateaus adjacent to Valles Marineris, *Icarus* **205**, *73–102*,. https://doi.org/10.1016/j.icarus.2009.04.017

Weitz C.M., Bishop J.L., (2016) Stratigraphy and formation of clays, sulfates, and hydrated silica within a depression in Coprates Catena, Mars, *J. Geophys. Res. E Planets* **121**, *805–835*,.

https://doi.org/10.1002/2015JE004954

Wendt L. et al., (2011) Sulfates and iron oxides in Ophir Chasma, Mars, based on OMEGA and CRISM observations, *Icarus* **213**, *86–103*,. https://doi.org/10.1016/j.icarus.2011.02.013

Wetherbee R. et al., (2005) The Nanostructure and Development of Diatom Biosilica, *Biominer. Prog. Biol. Mol. Biol. Appl. 177–194*,. https://doi.org/10.1002/3527604138.ch11

Wiens R.C. et al., (2017) The SuperCam remote sensing instrument suite for the Mars 2020 rover: a preview, *Spectroscopy* **32**, *50*,.

Williams L.A.N.N., Crerar D.A., (1985) Silica diagenesis: II. General mechanisms, *Deep Sea Res. Part B. Oceanogr. Lit. Rev.* **32**, *1021*,. https://doi.org/10.1016/0198-0254(85)93827-0

Wray J.J. et al., (2013) Prolonged magmatic activity on Mars inferred from the detection of felsic rocks, *Nat. Geosci.* **6**, *1013–1017*,. https://doi.org/10.1038/ngeo1994

Appendices

Annex 1. Chemical composition of some terrestrial volcanic samples used in this study (EMP analysis).

Wt. %	Obsidian	Glasses			
	Obs_3	SO100-86DS Freund et al. (2013)	SO100-91DS Freund et al. (2013)	SO100-92DS Freund et al. (2013)	Shosho
SiO_2	75.66	59.94	60.19	55.70	76.11
TiO_2	0.14	1.30	1.28	1.51	0.02
Al_2O_3	12.98	13.56	13.48	14.19	13.84
FeO_{tot} [a]	1.05	9.42	8.94	10.05	0.79
MnO	0.07	0.16	0.14	0.17	0.11
MgO	0.15	1.86	1.88	3.55	0.01
CaO	0.68	5.26	5.12	7.38	0.53
Na_2O	3.72	4.67	4.35	4.11	3.39
K_2O	5.26	1.10	1.10	0.72	5.50
P_2O_5	0.00	0.40	0.38	0.41	0.00
SO_2	*n.c*	0.05	0.05	0.09	*n.c*
Cl	*n.c*	0.98	0.90	0.81	*n.c*
Total [a]	99.71	98.70	97.73	98.69	100.30

n.c = not calculated

[a] Total expressed with all Fe expressed as FeO_{tot}

Annex 2. Processing of NIR spectra.

First, spectra were smoothed using the Savitzky-Golay method with the OriginPro 8.5 data analysis software. This smoothing method consists of a least square polynomial regression of adjacent data points (Savitzky and Golay, 1964; Steinier et al., 1972). Regression was performed using third-degree polynomial functions and a moving average windows of about ~ 7 to 9 points/spectels for data at CRISM resolution (laboratory data resampled at CRISM resolution and martian data) and ~ 18 to 20 points/spectels for data at laboratory resolution. This method was preferred to the common-used mean-average methods that do not smooth enough the data without shifting local minima of the spectra. Indeed, the Savitzky-Golay method is able to take into account points of inflection when polynomial functions of degree greater than two are used, so local minima can be kept while maintaining a good signal-to-noise ratio after smoothing.

Next, we performed a continuum removing of the smoothed spectra using the Segmented-Upper-Hull-Method (SUH method) implemented in the ENVI® software (Clark et al., 1987). This automated method uses tie-points on spectral local maxima and draw linear functions between them. Other methods of continuum removing were also tested (e.g. continuum removing using tie-points and linear functions or polynomial functions between absorption bands) but we did not observe great differences in the results of these different methods compared to the SUH method results. The SUH method was then preferred compared to these other methods because of low-time calculation and good approximation of the baseline correction.

Then, each absorption feature (near 1.4-, 1.9-, and 2.2 µm) of the hydrated silica spectrum are isolated from the rest of the spectrum by truncation using two anchors points (Table 4). Using OriginPro 8.5 data analysis software, each isolated absorption feature is then fitted using several gaussian functions depending on spectral absorptions produced by the presence of isolated or H-bonded silanols and water molecules in the opal structure (e.g. Anderson and Wickersheim, 1964; Langer and Flörke, 1974; Graetsch et al., 1994; Christy, 2010, 2011; Boboň et al., 2011; Rice et al., 2013; Smith et al., 2013; Chauviré et al., 2017a; Sun, 2017; Sun and Milliken, 2018) (Figure 1) (Table 1). Following Day and Jones (2008), we used four gaussian functions to fit the 1.9 µm absorption feature at ~ 1.91, ~ 1.935, ~ 1.96 and ~ 2.00 µm. As well, we used four gaussian functions to fit the 2.2 µm absorption feature at ~ 2.21, ~ 2.235, ~ 2.26 and ~ 2.29 µm. Day and Jones (2008) used only three gaussian functions for this absorption band, but we found that an additional gaussian function allowed us to obtain a better fitting percentage and to better accommodate subtle variations in the 2.2 µm-band. For the absorption feature near 1.4 µm, we used five gaussian functions located at ~ 1.38, ~ 1.41, ~ 1.435, ~ 1.46 and ~ 1.49 µm. Compared to the two other absorptions bands, the use of a short-wavelength gaussian function at ~ 1.38 µm was used to prevent absorption features of martian hydrated silica spectra that, when dehydrated, show reflectance minima below ~ 1.39-1.40 µm. This additional ~ 1.38 µm-gaussian function does

permit us to not shift the other absorption bands when considering martian hydrated silica spectra. The addition of this gaussian function is also in agreement with NIR vibrational species in hydrated silica as isolated hydroxyl groups show a sharp and clear absorption band at 1.38 µm (e.g. Rice et al., 2013; Smith et al., 2013; Sun, 2017).

Finally, the area of each absorption feature is calculated as the sum of the areas of the gaussian functions contained in each of these. These areas are then converted into relative areas where the area of a single absorption band is normalized to the sum of the areas of all absorption bands (1.4-, 1.9- and 2.2 µm absorption features) in the spectra. These relative area contributions are given in percent. Eventually, spectral criteria are calculated on the simulated spectra of each absorption band after their deconvolution by gaussian functions.

Annex 3. Results of the spectral criteria calculations for terrestrial data measured at atmospheric ambient pressure resampled at CRISM resolution.

Geological origin	Silica variety	Sample ID	1.4 µm absorption band						1.9 µm absorption band						2.2 µm absorption band					
			Min. Pos. (µm)	σ	CRC	σ	Rel. Area (%)	σ	Min. Pos. (µm)	σ	CRC	σ	Rel. Area (%)	σ	Min. Pos. (µm)	σ	CRC	σ	Rel. Area (%)	σ
Weathering (T < 50°C)	Opal-A	1040 ^{P}	1.413	*0.0004*	0.99	*0.021*	32	*2.6*	1.907	*0.0002*	0.90	*0.037*	59	*2.5*	2.218	*0.0004*	1.13	*0.018*	9	*0.8*
		1040 ^{S}	1.412	*0.0005*	0.87	*0.020*	21	*2.0*	1.906	*0.0003*	0.78	*0.030*	67	*2.2*	2.220	*0.0003*	1.21	*0.020*	11	*0.9*
		1039 ^{S}	1.414	*0.0004*	0.93	*0.018*	19	*2.1*	1.907	*0.0002*	0.75	*0.030*	73	*2.3*	2.220	*0.0003*	1.09	*0.021*	9	*0.8*
		MTB01 ^{S}	1.415	*0.0005*	0.96	*0.019*	20	*2.1*	1.907	*0.0002*	0.76	*0.030*	72	*2.3*	2.220	*0.0003*	1.16	*0.017*	8	*0.8*
		MTB02 ^{S}	1.413	*0.0004*	0.89	*0.019*	19	*2.1*	1.907	*0.0002*	0.67	*0.035*	69	*2.1*	2.220	*0.0003*	1.19	*0.018*	12	*0.8*
	Opal-CT	VTB ^{S}	1.418	*0.0009*	0.81	*0.042*	24	*0.9*	1.909	*0.0008*	0.63	*0.026*	66	*2.3*	2.264	*0.0072*	0.99	*0.028*	10	*1.6*
		FT1111 ^{S}	1.414	*0.0011*	0.66	*0.051*	20	*0.7*	1.910	*0.0007*	0.57	*0.029*	70	*1.9*	2.254	*0.0067*	1.05	*0.025*	10	*1.6*
		WT86 ^{S}	1.420	*0.0010*	0.92	*0.048*	20	*0.7*	1.912	*0.0007*	0.73	*0.031*	77	*2.1*	2.225	*0.0084*	1.14	*0.030*	3	*1.7*
		208 ^{S}	1.418	*0.0009*	0.83	*0.042*	21	*0.7*	1.913	*0.0008*	0.63	*0.026*	75	*2.0*	2.259	*0.0069*	1.03	*0.025*	4	*1.6*
Hydrothermal (T > 50-100°C)	Opal-A	104.258 ^{S}	1.413	*0.0004*	0.98	*0.027*	19	*2.4*	1.910	*0.0007*	0.98	*0.033*	77	*4.3*	2.214	*0.0012*	0.85	*0.085*	4	*2.9*
		85.27 ^{P}	1.414	*0.0005*	1.08	*0.032*	29	*2.6*	1.908	*0.0006*	0.98	*0.033*	62	*3.7*	2.218	*0.0010*	1.13	*0.073*	9	*2.5*
		46.170 ^{P}	1.412	*0.0005*	0.96	*0.029*	22	*2.2*	1.907	*0.0007*	0.85	*0.038*	62	*3.7*	2.218	*0.0010*	1.16	*0.075*	16	*3.0*
	Opal-CT	493 ^{S}	1.451	*0.0031*	1.05	*0.010*	21	*0.6*	1.925	*0.0015*	1.00	*0.011*	79	*0.7*	2.216	*0.0039*	0.49	*0.071*	0	*0.4*
		1543a ^{S}	1.453	*0.0032*	1.03	*0.011*	23	*0.6*	1.930	*0.0016*	1.00	*0.011*	75	*0.7*	2.216	*0.0039*	0.42	*0.073*	1	*0.4*
		1543b ^{S}	1.448	*0.0031*	1.05	*0.010*	24	*0.6*	1.918	*0.0014*	1.07	*0.012*	76	*0.7*	2.215	*0.0039*	0.50	*0.070*	0	*0.4*
		1543c ^{S}	1.448	*0.0031*	1.05	*0.010*	21	*0.6*	1.920	*0.0014*	1.02	*0.011*	78	*0.7*	2.214	*0.0039*	1.06	*0.068*	1	*0.4*
		1543d ^{S}	1.448	*0.0031*	1.05	*0.010*	21	*0.6*	1.920	*0.0014*	1.00	*0.011*	77	*0.7*	2.217	*0.0039*	1.07	*0.068*	2	*0.4*
		1552a ^{S}	1.446	*0.0031*	1.06	*0.010*	22	*0.6*	1.916	*0.0014*	1.02	*0.011*	77	*0.7*	2.216	*0.0039*	0.99	*0.067*	2	*0.4*
		1552b ^{S}	1.443	*0.0031*	1.00	*0.011*	21	*0.6*	1.914	*0.0014*	1.02	*0.011*	75	*0.7*	2.268	*0.0051*	0.93	*0.066*	5	*0.4*
		1552c ^{S}	1.449	*0.0031*	1.05	*0.010*	21	*0.6*	1.919	*0.0014*	1.01	*0.011*	78	*0.7*	2.215	*0.0039*	0.75	*0.066*	1	*0.4*

		1552d^{S}	1.449	*0.0031*	1.05	*0.010*	20	*0.6*	1.919	*0.0014*	1.01	*0.011*	79	*0.7*	2.219	*0.0039*	0.86	*0.066*	1	*0.4*
		521^{S}	1.420	*0.0035*	1.13	*0.011*	21	*0.6*	1.914	*0.0014*	0.96	*0.012*	74	*0.7*	2.239	*0.0041*	1.12	*0.069*	5	*0.4*
		1551^{S}	1.420	*0.0035*	1.13	*0.011*	22	*0.6*	1.911	*0.0015*	0.93	*0.012*	75	*0.7*	2.223	*0.0039*	1.21	*0.071*	3	*0.4*
		YM12^{S}	1.425	*0.0033*	1.13	*0.011*	22	*0.6*	1.914	*0.0014*	0.91	*0.013*	78	*0.7*	2.223	*0.0039*	0.73	*0.066*	1	*0.4*
		24.349^{P}	1.449	*0.0031*	1.05	*0.010*	29	*0.8*	1.926	*0.0015*	1.05	*0.012*	69	*0.8*	2.215	*0.0039*	0.93	*0.066*	2	*0.4*
Volcanic (very-high temperature)	Obsidian	Gi1900^{P}	n.c	*n.c*	n.c	*n.c*	n.c	*n.c*	n.c	*n.c*	n.c	*n.c*	n.c	*n.c*	2.211	*0.0012*	0.96	*0.022*	n.c	*n.c*
		Obs_3^{P}	1.409	*0.0009*	0.31	*0.045*	9	*1.1*	1.909	*0.0022*	0.32	*0.050*	50	*11.1*	2.219	*0.0013*	0.97	*0.023*	41	*12.1*
		Obs_1^{P}	1.405	*0.0010*	0.12	*0.049*	5	*0.9*	1.915	*0.0019*	0.45	*0.059*	4	*9.1*	2.214	*0.0011*	0.84	*0.023*	91	*9.9*
		Obs_1^{S}	1.408	*0.0009*	0.26	*0.041*	7	*0.9*	1.914	*0.0019*	0.24	*0.050*	3	*9.1*	2.215	*0.0011*	0.90	*0.021*	90	*9.9*
		Obs_2^{P}	n.c	*n.c*	n.c	*n.c*	4	*1.0*	1.921	*0.0023*	0.15	*0.057*	7	*9.0*	2.214	*0.0011*	0.87	*0.022*	90	*9.8*
	Glass	WD3^{S}	1.413	*0.0019*	0.36	*0.094*	18	*4.3*	1.908	*0.0017*	0.38	*0.038*	62	*8.6*	2.218	*0.0018*	0.92	*0.030*	19	*11.5*
		SO100-86DS$_{P}$	1.408	*0.0016*	0.00	*0.085*	21	*4.5*	1.916	*0.0014*	0.37	*0.038*	24	*7.0*	2.218	*0.0018*	0.95	*0.030*	55	*9.3*
		SO100-91DS$_{P}$	n.c	*n.c*	n.c	*n.c*	0	*n.c*	1.915	*0.0014*	0.52	*0.046*	26	*7.0*	2.218	*0.0018*	0.99	*0.032*	74	*9.5*
		SO100-92DS$_{P}$	n.c	*n.c*	n.c	*n.c*	n.c	*n.c*	1.915	*0.0014*	0.27	*0.041*	31	*6.9*	2.208	*0.0020*	1.01	*0.033*	69	*9.3*
		Shosho^{P}	1.405	*0.0019*	0.08	*0.079*	4	*4.2*	1.918	*0.0015*	0.27	*0.041*	11	*7.7*	2.212	*0.0017*	0.80	*0.038*	85	*10.1*
Uncertain or Unclear	Chalcedony	Gi526^{P}	1.424	*0.0003*	0.92	*0.020*	26	*2.0*	1.918	*0.0006*	0.89	*0.015*	48	*2.5*	2.224	*0.0031*	1.15	*0.019*	26	*3.3*
		Gi526^{S}	1.425	*0.0004*	0.89	*0.022*	19	*1.6*	1.920	*0.0006*	0.86	*0.013*	53	*2.8*	2.234	*0.0028*	1.10	*0.021*	29	*3.2*
		1542^{S}	1.424	*0.0003*	0.93	*0.020*	16	*1.8*	1.920	*0.0006*	0.85	*0.013*	47	*2.5*	2.240	*0.0032*	1.12	*0.019*	37	*3.1*
		1553^{S}	1.423	*0.0004*	1.01	*0.025*	20	*1.6*	1.917	*0.0007*	0.81	*0.015*	37	*3.0*	2.228	*0.0028*	1.21	*0.023*	43	*3.5*
	Opal-A	785^{P}	1.407	*0.0012*	0.91	*0.017*	29	*2.4*	1.902	*0.0011*	0.79	*0.011*	48	*4.3*	2.216	*0.0069*	1.29	*0.047*	23	*2.7*
		785^{S}	1.409	*0.0011*	0.83	*0.022*	16	*2.0*	1.902	*0.0011*	0.74	*0.011*	61	*3.5*	2.217	*0.0068*	1.34	*0.050*	23	*2.7*
		86.2^{S}	1.410	*0.0010*	0.91	*0.017*	17	*2.0*	1.904	*0.0010*	0.75	*0.011*	62	*3.5*	2.258	*0.0086*	1.03	*0.052*	21	*2.6*
		766^{S}	1.412	*0.0011*	0.94	*0.018*	18	*1.9*	1.907	*0.0011*	0.74	*0.011*	70	*3.7*	2.218	*0.0068*	1.16	*0.045*	12	*2.7*
		BR08^{S}	1.414	*0.0012*	0.95	*0.019*	20	*1.9*	1.908	*0.0012*	0.80	*0.012*	72	*3.8*	2.219	*0.0068*	1.17	*0.045*	8	*3.0*

Opal-CT	928 [S]	1.422	*0.0043*	1.11	*0.010*	20	*1.7*	1.913	*0.0021*	0.90	*0.023*	74	*1.7*	2.219	*0.0009*	1.13	*0.181*	6	*1.1*
	1085 [P]	1.437	*0.0035*	1.10	*0.009*	32	*2.2*	1.919	*0.0018*	1.04	*0.023*	65	*2.1*	2.219	*0.0009*	1.11	*0.180*	3	*1.0*
	1085 [S]	1.443	*0.0035*	1.09	*0.009*	19	*1.8*	1.926	*0.0020*	0.99	*0.021*	72	*1.7*	2.213	*0.0010*	0.04	*0.200*	9	*1.2*
	1548 [S]	1.450	*0.0038*	1.05	*0.010*	22	*1.7*	1.922	*0.0019*	1.02	*0.022*	77	*1.7*	2.215	*0.0009*	0.19	*0.190*	1	*1.1*
	Gi848 [S]	1.448	*0.0037*	1.05	*0.010*	20	*1.7*	1.925	*0.0020*	1.00	*0.021*	78	*1.8*	2.217	*0.0008*	1.02	*0.177*	2	*1.0*
	1547 [S]	1.440	*0.0035*	1.09	*0.009*	20	*1.7*	1.915	*0.0020*	0.90	*0.023*	78	*1.7*	2.218	*0.0009*	1.04	*0.177*	3	*1.0*

[S] for thin sections, [P] for powders

n.c = not calculated (absorption embed in the spectral noise or at the same order of magnitude as the spectral noise for example)

σ = SEM for Standard Error

Annex 4. Results of the spectral criteria calculations for terrestrial data measured at atmospheric ambient pressure and sampled at laboratory resolution.

Geological origin	Silica variety	Sample ID	1.4 µm absorption band						1.9 µm absorption band						2.2 µm absorption band					
			Min. Pos. (µm)	σ	CRC	σ	Rel. Area (%)	σ	Min. Pos. (µm)	σ	CRC	σ	Rel. Area (%)	σ	Min. Pos. (µm)	σ	CRC	σ	Rel. Area (%)	σ
Weathering (T < 50°C)	Opal-A	1040 P	1.413	*0.0003*	0.98	*0.021*	31	*2.6*	1.907	*0.0005*	0.90	*0.040*	60	*2.4*	2.217	*0.0005*	1.11	*0.022*	9	*0.7*
		1040 S	1.412	*0.0002*	0.87	*0.020*	20	*2.0*	1.905	*0.0004*	0.78	*0.033*	68	*1.9*	2.219	*0.0004*	1.23	*0.024*	12	*0.7*
		1039 S	1.412	*0.0002*	0.91	*0.019*	19	*2.1*	1.905	*0.0004*	0.74	*0.033*	73	*2.1*	2.219	*0.0004*	1.09	*0.023*	9	*0.7*
		MTB01 S	1.412	*0.0002*	0.96	*0.020*	19	*2.0*	1.905	*0.0004*	0.75	*0.033*	73	*2.1*	2.219	*0.0004*	1.14	*0.021*	8	*0.7*
		MTB02 S	1.411	*0.0003*	0.87	*0.020*	19	*2.0*	1.904	*0.0004*	0.65	*0.038*	69	*1.9*	2.219	*0.0004*	1.18	*0.021*	12	*0.7*
	Opal-CT	VTB S	1.418	*0.0007*	0.80	*0.046*	21	*0.5*	1.909	*0.0005*	0.65	*0.026*	69	*1.8*	2.263	*0.0076*	0.99	*0.030*	10	*1.5*
		FT1111 S	1.414	*0.0008*	0.65	*0.055*	20	*0.4*	1.909	*0.0006*	0.56	*0.030*	70	*1.7*	2.252	*0.0071*	1.06	*0.026*	10	*1.5*
		WT86 S	1.418	*0.0007*	0.94	*0.054*	20	*0.4*	1.910	*0.0005*	0.72	*0.031*	77	*1.8*	2.222	*0.0089*	1.15	*0.032*	3	*1.6*
		208 S	1.417	*0.0006*	0.81	*0.046*	19	*0.5*	1.912	*0.0006*	0.61	*0.027*	77	*1.8*	2.258	*0.0073*	1.03	*0.027*	4	*1.4*
Hydrothermal (T > 50-100°C)	Opal-A	104.258 S	1.413	*0.0003*	0.96	*0.033*	19	*2.3*	1.908	*0.0009*	0.98	*0.035*	77	*4.3*	2.214	*0.0008*	0.76	*0.110*	4	*2.9*
		85.27 P	1.412	*0.0003*	1.09	*0.039*	29	*2.5*	1.906	*0.0008*	0.98	*0.035*	63	*3.7*	2.217	*0.0007*	1.13	*0.094*	9	*2.5*
		46.170 P	1.411	*0.0003*	0.95	*0.034*	22	*2.1*	1.904	*0.0009*	0.84	*0.040*	62	*3.7*	2.217	*0.0007*	1.15	*0.096*	16	*3.0*
	Opal-CT	493 S	1.449	*0.0032*	1.05	*0.012*	20	*0.6*	1.930	*0.0022*	0.99	*0.010*	79	*0.8*	2.215	*0.0039*	0.43	*0.077*	0	*0.4*
		1543a S	1.453	*0.0033*	1.03	*0.012*	23	*0.6*	1.932	*0.0023*	0.98	*0.010*	75	*0.7*	2.215	*0.0039*	0.40	*0.078*	1	*0.4*
		1543b S	1.446	*0.0032*	1.06	*0.012*	24	*0.6*	1.928	*0.0022*	1.04	*0.011*	76	*0.7*	2.213	*0.0039*	0.44	*0.077*	1	*0.4*
		1543c S	1.447	*0.0032*	1.06	*0.012*	21	*0.6*	1.929	*0.0022*	0.98	*0.010*	78	*0.7*	2.214	*0.0039*	1.03	*0.072*	1	*0.4*
		1543d S	1.449	*0.0032*	1.04	*0.012*	21	*0.6*	1.928	*0.0022*	0.96	*0.010*	77	*0.7*	2.216	*0.0039*	1.05	*0.073*	2	*0.4*
		1552a S	1.441	*0.0032*	1.10	*0.012*	21	*0.6*	1.927	*0.0022*	0.98	*0.010*	77	*0.7*	2.216	*0.0039*	0.93	*0.071*	2	*0.4*
		1552b S	1.443	*0.0032*	1.00	*0.013*	23	*0.6*	1.910	*0.0024*	1.05	*0.011*	72	*0.8*	2.265	*0.0050*	0.97	*0.072*	5	*0.5*

		1552c[S]	1.449	*0.0032*	1.05	*0.012*	20	*0.6*	1.929	*0.0022*	0.96	*0.010*	78	*0.8*	2.213	*0.0039*	0.66	*0.072*	1	*0.4*
		1552d[S]	1.447	*0.0032*	1.06	*0.012*	20	*0.6*	1.928	*0.0022*	0.97	*0.010*	79	*0.8*	2.216	*0.0039*	0.87	*0.071*	1	*0.4*
		521[S]	1.418	*0.0036*	1.14	*0.013*	21	*0.6*	1.912	*0.0024*	0.97	*0.010*	74	*0.8*	2.242	*0.0042*	1.13	*0.074*	5	*0.5*
		1551[S]	1.419	*0.0035*	1.14	*0.013*	22	*0.6*	1.911	*0.0024*	0.94	*0.011*	75	*0.7*	2.223	*0.0039*	1.23	*0.077*	3	*0.4*
		YM12[S]	1.423	*0.0034*	1.14	*0.013*	21	*0.6*	1.913	*0.0023*	0.91	*0.011*	78	*0.7*	2.219	*0.0039*	0.75	*0.071*	1	*0.4*
		24.349[P]	1.448	*0.0032*	1.06	*0.012*	29	*0.7*	1.930	*0.0022*	1.03	*0.011*	70	*0.9*	2.214	*0.0039*	0.97	*0.072*	2	*0.4*
Volcanic (very-high temperature)	Obsidian	Gi1900[P]	n.c	*n.c*	n.c	*n.c*	n.c	*n.c*	n.c	*n.c*	n.c	*n.c*	n.c	*n.c*	2.215	*0.0009*	0.99	*0.027*	n.c	*n.c*
		Obs_3[P]	1.412	*0.0021*	0.30	*0.062*	9	*1.3*	1.906	*0.0022*	0.32	*0.053*	50	*11.4*	2.220	*0.0010*	0.94	*0.024*	41	*11.9*
		Obs_1[P]	1.405	*0.0018*	0.13	*0.059*	5	*1.3*	1.908	*0.0021*	0.35	*0.052*	3	*9.4*	2.214	*0.0009*	0.84	*0.025*	92	*9.9*
		Obs_1[S]	1.402	*0.0020*	0.33	*0.064*	11	*1.5*	1.918	*0.0027*	0.51	*0.062*	3	*9.3*	2.216	*0.0008*	0.91	*0.023*	86	*9.6*
		Obs_2[P]	1.406	*0.0018*	0.01	*0.069*	4	*1.4*	1.907	*0.0022*	0.18	*0.061*	6	*9.2*	2.215	*0.0008*	0.85	*0.025*	90	*9.8*
	Glass	WD3[S]	1.413	*0.0014*	0.36	*0.135*	20	*3.3*	1.905	*0.0022*	0.37	*0.044*	59	*8.2*	2.222	*0.0018*	0.98	*0.024*	21	*11.1*
		SO100-86DS[P]	1.407	*0.0012*	0.13	*0.141*	5	*2.9*	1.913	*0.0020*	0.36	*0.044*	29	*6.7*	2.219	*0.0017*	0.91	*0.022*	67	*8.8*
		SO100-91DS[P]	1.407	*0.0012*	0.83	*0.166*	9	*2.7*	1.913	*0.0020*	0.40	*0.045*	23	*6.8*	2.218	*0.0017*	0.97	*0.023*	68	*8.8*
		SO100-92DS[P]	n.c	n.c	n.c	n.c	n.c	n.c	1.918	*0.0023*	0.47	*0.048*	31	*6.7*	2.224	*0.0019*	0.94	*0.022*	69	*8.8*
		Shosho[P]	1.407	*0.0012*	0.06	*0.146*	6	*2.8*	1.906	*0.0022*	0.15	*0.055*	10	*7.5*	2.212	*0.0020*	0.83	*0.027*	84	*9.5*
Uncertain or Unclear	Chalcedony	Gi526[P]	1.424	*0.0004*	0.91	*0.023*	25	*1.7*	1.917	*0.0004*	0.90	*0.015*	49	*2.5*	2.227	*0.0050*	1.13	*0.023*	27	*3.2*
		Gi526[S]	1.424	*0.0004*	0.86	*0.026*	18	*1.4*	1.918	*0.0005*	0.87	*0.013*	53	*2.8*	2.226	*0.0051*	1.17	*0.026*	29	*3.0*
		1542[S]	1.422	*0.0005*	0.91	*0.023*	16	*1.6*	1.916	*0.0004*	0.87	*0.013*	47	*2.5*	2.247	*0.0050*	1.06	*0.024*	37	*2.9*
		1553[S]	1.422	*0.0004*	1.00	*0.028*	19	*1.4*	1.916	*0.0004*	0.82	*0.016*	38	*3.0*	2.247	*0.0050*	1.05	*0.025*	43	*3.4*
	Opal-A	785[P]	1.408	*0.0008*	0.90	*0.018*	29	*2.3*	1.901	*0.0006*	0.78	*0.010*	48	*4.2*	2.216	*0.0071*	1.29	*0.048*	24	*2.7*
		785[S]	1.407	*0.0008*	0.82	*0.022*	16	*1.9*	1.902	*0.0006*	0.73	*0.011*	60	*3.5*	2.217	*0.0071*	1.33	*0.051*	23	*2.7*
		86.2[S]	1.410	*0.0007*	0.91	*0.018*	17	*1.9*	1.903	*0.0006*	0.75	*0.010*	62	*3.5*	2.259	*0.0089*	1.02	*0.053*	21	*2.6*
		766[S]	1.411	*0.0008*	0.92	*0.018*	18	*1.8*	1.904	*0.0006*	0.74	*0.010*	70	*3.7*	2.216	*0.0071*	1.15	*0.046*	12	*2.7*

Opal-CT	BR08 ^{S}	1.412	*0.0009*	0.95	*0.020*	19	*1.8*	1.905	*0.0007*	0.79	*0.011*	72	*3.8*	2.218	*0.0070*	1.16	*0.045*	8	*3.0*
	928 ^{S}	1.420	*0.0050*	1.12	*0.017*	20	*1.6*	1.910	*0.0034*	0.91	*0.021*	74	*2.1*	2.217	*0.0006*	1.12	*0.179*	6	*2.2*
	1085 ^{P}	1.444	*0.0042*	1.07	*0.017*	31	*2.1*	1.916	*0.0031*	1.06	*0.023*	67	*2.3*	2.217	*0.0006*	1.09	*0.177*	3	*2.2*
	1085 ^{S}	1.445	*0.0042*	1.08	*0.017*	20	*1.6*	1.930	*0.0033*	0.97	*0.020*	78	*2.2*	2.213	*0.0007*	0.03	*0.200*	1	*2.3*
	1548 ^{S}	1.450	*0.0044*	1.05	*0.018*	22	*1.6*	1.928	*0.0032*	1.00	*0.020*	78	*2.2*	2.215	*0.0006*	0.21	*0.188*	0	*2.3*
	Gi848 ^{S}	1.447	*0.0043*	1.06	*0.018*	17	*1.7*	1.930	*0.0033*	0.97	*0.020*	65	*2.4*	2.215	*0.0006*	1.03	*0.175*	17	*2.8*
	1547 ^{S}	1.429	*0.0043*	1.18	*0.021*	19	*1.6*	1.914	*0.0032*	0.91	*0.021*	78	*2.2*	2.216	*0.0006*	1.04	*0.176*	2	*2.2*

^{S} for thin sections, ^{P} for powders

n.c = not calculated (absorption embed in the spectral noise or at the same order of magnitude as the spectral noise for example)

σ = SEM for Standard Error

Annex 5. Results of the spectral criteria calculations for terrestrial data measured at Mars-relevant atmospheric pressure sampled at laboratory resolution (all samples are thin sections).

Geological origin	Silica variety	Sample ID	1.4 µm absorption band						1.9 µm absorption band						2.2 µm absorption band						Experiment duration and atmospheric pressure at the end of acquisition
			Min. Pos. (µm)	σ	CRC	σ	Rel. Area (%)	σ	Min. Pos. (µm)	σ	CRC	σ	Rel. Area (%)	σ	Min. Pos. (µm)	σ	CRC	σ	Rel. Area (%)	σ	
Weathering (T < 50°C)	Opal-A	1040 (initial)	1.412	*0.0001*	0.87	*0.003*	20	*0.2*	1.905	*0.0001*	0.78	*0.003*	68	*0.5*	2.219	*0.0004*	1.23	*0.017*	12	*0.3*	6h46 at 7.68 mbar
		1040 (final)	1.412	*0.0001*	0.88	*0.003*	20	*0.2*	1.905	*0.0001*	0.77	*0.003*	70	*0.5*	2.218	*0.0004*	1.18	*0.017*	11	*0.3*	
	Opal-CT	VTB (initial)	1.418	*0.0006*	0.80	*0.0533*	21	*0.1*	1.909	*0.0003*	0.65	*0.0867*	69	*7.7*	2.263	*0.0243*	0.99	*0.1133*	10	*7.6*	14h42 at 7.24 mbar
		VTB (final)	1.416	*0.0006*	0.64	*0.0533*	22	*0.1*	1.908	*0.0003*	0.39	*0.0867*	46	*7.7*	2.190	*0.0243*	1.33	*0.1133*	32	*7.6*	
		FT1111 (initial)	1.414	*0.0015*	0.65	*0.0667*	20	*0.9*	1.909	*0.0008*	0.56	*0.0600*	70	*8.9*	2.252	*0.0203*	1.06	*0.1033*	10	*8.1*	7h40 at 7.25 mbar
		FT1111 (final)	1.410	*0.0015*	0.45	*0.0667*	22	*0.9*	1.907	*0.0008*	0.38	*0.0600*	44	*8.9*	2.191	*0.0203*	0.75	*0.1033*	34	*8.1*	
Hydrothermal (T > 50-100°C)	Opal-CT	1543b (initial)	1.446	*0.0019*	1.06	*0.0133*	24	*0.1*	1.928	*0.0004*	1.04	*0.0000*	76	*0.1*	2.213	*0.0001*	0.44	*0.0400*	1	*0.0*	4h00 at 7.36 mbar
		1543b (final)	1.440	*0.0019*	1.10	*0.0133*	23	*0.1*	1.927	*0.0004*	1.04	*0.0000*	76	*0.1*	2.214	*0.0001*	0.56	*0.0400*	1	*0.0*	
		1551 (initial)	1.419	*0.0000*	1.14	*0.0067*	22	*0.0*	1.911	*0.0001*	0.94	*0.0033*	75	*0.1*	2.223	*0.0002*	1.23	*0.0100*	3	*0.2*	14h40 at 7.25 mbar
		1551 (final)	1.419	*0.0000*	1.16	*0.0067*	22	*0.0*	1.911	*0.0001*	0.95	*0.0033*	75	*0.1*	2.223	*0.0002*	1.20	*0.0100*	3	*0.2*	
Uncertain or Unclear	Opal-A	785 (initial)	1.407	*0.0000*	0.82	*0.0000*	16	*0.1*	1.902	*0.0000*	0.73	*0.0000*	60	*0.1*	2.217	*0.0001*	1.33	*0.0067*	23	*0.0*	3h08 at 7.36 mbar
		785 (final)	1.407	*0.0000*	0.82	*0.0000*	16	*0.1*	1.902	*0.0000*	0.73	*0.0000*	61	*0.1*	2.217	*0.0001*	1.31	*0.0067*	23	*0.0*	
		86.2 (initial)	1.410	*0.0001*	0.91	*0.0033*	17	*0.4*	1.903	*0.0001*	0.75	*0.0000*	62	*0.4*	2.259	*0.0138*	1.02	*0.1233*	21	*0.0*	4h18 at 7.21 mbar
		86.2 (final)	1.410	*0.0001*	0.92	*0.0033*	18	*0.4*	1.902	*0.0001*	0.75	*0.0000*	61	*0.4*	2.218	*0.0138*	1.39	*0.1233*	21	*0.0*	
	Opal-CT	1548 (initial)	1.450	*0.0001*	1.05	*0.000*	22	*0.0*	1.928	*0.0003*	1.00	*0.000*	78	*0.0*	2.215	*0.0001*	0.21	*0.017*	0	*0.0*	3h52 at 7.17 mbar
		1548 (final)	1.449	*0.0001*	1.05	*0.000*	22	*0.0*	1.927	*0.0003*	1.00	*0.000*	78	*0.0*	2.214	*0.0001*	0.26	*0.017*	0	*0.0*	

σ = SEM for Standard Error

Annex 6. Results of the spectral criteria calculations on martian CRISM detections.

Region	ID CRISM (ROI n°)	1.4 µm absorption band						1.9 µm absorption band						2.2 µm absorption band					
		Min. Pos. (µm)	σ	CRC	σ	Rel. Area (%)	σ	Min. Pos. (µm)	σ	CRC	σ	Rel. Area (%)	σ	Min. Pos. (µm)	σ	CRC	σ	Rel. Area (%)	σ
Aeolis Mensae	C549 (1)	1.381	*0.0012*	0.57	*0.034*	20	*1.6*	1.909	*0.0022*	0.69	*0.061*	24	*1.1*	2.219	*0.0037*	1.08	*0.022*	56	*0.7*
	C549 (2)	1.382	*0.0013*	0.71	*0.039*	14	*1.5*	1.908	*0.0023*	0.88	*0.072*	28	*1.2*	2.203	*0.0038*	1.01	*0.018*	58	*0.6*
	C549 (3)	1.377	*0.0014*	0.58	*0.033*	16	*1.3*	1.917	*0.0026*	0.59	*0.068*	25	*1.0*	2.213	*0.0032*	1.00	*0.019*	59	*0.7*
	86B7 (1)[a]	1.398	*0.0040*	0.62	*0.045*	15	*0.7*	1.914	*0.0012*	0.78	*0.022*	17	*0.9*	2.214	*0.0019*	0.95	*0.009*	68	*0.7*
	86B7 (2)[b]	1.383	*0.0033*	0.47	*0.037*	15	*0.7*	1.917	*0.0013*	0.67	*0.023*	14	*1.0*	2.211	*0.0018*	0.94	*0.010*	71	*0.8*
	86B7 (3)[c]	1.384	*0.0032*	0.48	*0.037*	17	*0.9*	1.915	*0.0012*	0.71	*0.020*	15	*0.9*	2.215	*0.0019*	0.97	*0.009*	68	*0.7*
	86B7 (4)	1.379	*0.0035*	0.39	*0.042*	13	*0.9*	1.910	*0.0014*	0.76	*0.020*	19	*1.0*	2.205	*0.0022*	0.99	*0.010*	69	*0.6*
Camichel crater	985E (1)	1.384	*0.0004*	0.52	*0.039*	22	*0.5*	1.908	*0.0006*	0.89	*0.017*	24	*1.0*	2.204	*0.0009*	1.09	*0.014*	54	*0.6*
	985E (2)	1.382	*0.0004*	0.65	*0.033*	22	*0.5*	1.906	*0.0007*	1.00	*0.017*	28	*0.8*	2.204	*0.0009*	1.09	*0.014*	51	*0.6*
	985E (3)	1.382	*0.0004*	0.73	*0.035*	21	*0.5*	1.910	*0.0007*	0.94	*0.015*	26	*0.8*	2.205	*0.0008*	1.02	*0.017*	53	*0.5*
	985E (4)	1.383	*0.0004*	0.74	*0.036*	20	*0.5*	1.906	*0.0006*	0.93	*0.015*	28	*0.8*	2.205	*0.0008*	1.07	*0.014*	52	*0.5*
	985E (5)	1.384	*0.0004*	0.62	*0.033*	19	*0.5*	1.908	*0.0006*	0.96	*0.015*	30	*0.9*	2.209	*0.0011*	1.12	*0.015*	51	*0.5*
Ius Chasma	7F68 (1)	1.392	*0.0019*	0.62	*0.069*	18	*1.1*	1.923	*0.0011*	0.61	*0.017*	18	*0.4*	2.213	*0.0009*	1.00	*0.020*	63	*0.8*
	7F68 (2)	1.387	*0.0015*	0.51	*0.071*	15	*0.9*	1.926	*0.0012*	0.65	*0.014*	19	*0.4*	2.214	*0.0010*	0.99	*0.019*	65	*0.7*
	7F68 (3)	1.385	*0.0015*	0.81	*0.083*	13	*1.1*	1.926	*0.0012*	0.65	*0.014*	20	*0.4*	2.209	*0.0010*	0.94	*0.018*	68	*0.8*
	7F68 (4)	1.383	*0.0017*	0.39	*0.079*	16	*0.9*	1.921	*0.0013*	0.70	*0.017*	18	*0.4*	2.210	*0.0009*	0.90	*0.021*	66	*0.7*
	44AC (1)	1.387	*0.0010*	0.39	*0.039*	16	*0.8*	1.923	*0.0010*	0.67	*0.034*	20	*0.7*	2.212	*0.0011*	0.90	*0.012*	64	*1.3*
	44AC (2)	1.388	*0.0010*	0.48	*0.036*	16	*0.8*	1.923	*0.0010*	0.72	*0.036*	22	*0.8*	2.208	*0.0011*	0.93	*0.010*	62	*1.3*
	44AC (3)	1.383	*0.0012*	0.40	*0.038*	14	*0.9*	1.918	*0.0012*	0.73	*0.036*	18	*0.8*	2.208	*0.0011*	0.96	*0.011*	68	*1.6*
	44AC (4)	1.387	*0.0010*	0.59	*0.044*	19	*0.9*	1.922	*0.0010*	0.54	*0.042*	20	*0.7*	2.213	*0.0012*	0.94	*0.010*	61	*1.4*
Nilosyrtis Mensae	D452 (1)[d]	1.382	*0.0017*	0.50	*0.059*	14	*1.4*	1.914	*0.0062*	0.76	*0.061*	20	*1.4*	2.207	*0.0016*	0.91	*0.029*	67	*1.7*
	D452 (2)	1.379	*0.0020*	0.71	*0.052*	20	*1.4*	1.913	*0.0064*	0.69	*0.066*	17	*1.6*	2.205	*0.0018*	0.79	*0.032*	63	*1.5*
	D452 (3)	1.387	*0.0020*	0.70	*0.051*	17	*1.2*	1.938	*0.0073*	0.97	*0.072*	24	*1.7*	2.212	*0.0019*	0.89	*0.027*	59	*1.7*
Antoniadi crater	A2B3 (1)	1.423	*0.0007*	1.05	*0.015*	25	*1.8*	1.920	*0.0010*	0.86	*0.019*	40	*1.8*	2.214	*0.0008*	1.03	*0.017*	34	*2.3*
	A2B3 (2)	1.422	*0.0008*	1.10	*0.018*	19	*1.5*	1.921	*0.0009*	0.88	*0.017*	46	*2.2*	2.212	*0.0009*	0.99	*0.014*	34	*2.3*
	A2B3 (3)	1.425	*0.0009*	1.03	*0.017*	19	*1.6*	1.924	*0.0011*	0.94	*0.021*	38	*2.0*	2.216	*0.0009*	0.96	*0.017*	43	*2.7*
	7CBB (1)	1.419	*0.0037*	1.03	*0.056*	21	*2.0*	1.926	*0.0037*	0.99	*0.012*	42	*1.0*	2.207	*0.0038*	1.28	*0.053*	37	*1.9*
	7CBB (2)	1.434	*0.0037*	0.90	*0.047*	15	*1.7*	1.941	*0.0036*	1.04	*0.013*	46	*1.2*	2.219	*0.0032*	1.13	*0.045*	39	*1.7*
	7CBB (3)	1.427	*0.0031*	0.80	*0.055*	13	*1.8*	1.935	*0.0031*	1.00	*0.011*	42	*1.0*	2.221	*0.0034*	1.07	*0.050*	45	*2.0*
	9BCE (1)	1.428	*0.0032*	1.09	*0.045*	21	*1.4*	1.928	*0.0018*	0.96	*0.005*	39	*2.7*	2.211	*0.0018*	0.98	*0.042*	40	*1.4*
	9BCE (2)	1.440	*0.0037*	1.04	*0.041*	17	*1.1*	1.923	*0.0022*	0.98	*0.005*	48	*2.3*	2.211	*0.0018*	1.14	*0.038*	35	*1.2*

	9BCE (3)	1.426	*0.0033*	0.90	*0.049*	15	*1.2*	1.932	*0.0021*	0.97	*0.004*	49	*2.4*	2.218	*0.0021*	1.11	*0.036*	36	*1.2*
	9312 (1)	1.429	*0.0036*	1.01	*0.020*	18	*0.5*	1.922	*0.0010*	0.97	*0.018*	44	*0.8*	2.209	*0.0015*	1.09	*0.009*	38	*0.9*
	9312 (2)	1.419	*0.0037*	1.13	*0.017*	16	*0.6*	1.931	*0.0012*	0.88	*0.015*	42	*0.8*	2.217	*0.0013*	1.04	*0.009*	42	*1.1*
	9312 (3)	1.428	*0.0036*	1.10	*0.017*	19	*0.5*	1.925	*0.0010*	0.90	*0.015*	46	*0.8*	2.215	*0.0013*	1.03	*0.009*	35	*1.0*
	9312 (4)	1.418	*0.0037*	1.14	*0.018*	19	*0.5*	1.925	*0.0010*	0.89	*0.015*	46	*0.8*	2.211	*0.0014*	1.10	*0.010*	35	*1.0*
	9312 (5)	1.449	*0.0045*	1.05	*0.018*	21	*0.5*	1.922	*0.0010*	0.91	*0.015*	46	*0.8*	2.212	*0.0013*	1.06	*0.009*	34	*1.0*
	9312 (6)	1.420	*0.0037*	1.15	*0.018*	21	*0.5*	1.927	*0.0010*	0.82	*0.017*	40	*0.9*	2.217	*0.0013*	1.04	*0.009*	39	*1.0*
	9312 (7)	1.428	*0.0036*	1.08	*0.017*	20	*0.5*	1.925	*0.0010*	0.88	*0.015*	43	*0.8*	2.219	*0.0014*	1.06	*0.009*	37	*0.9*
Elorza crater	8236 (1)	1.421	*0.0073*	0.98	*0.029*	18	*1.4*	1.928	*0.0017*	0.79	*0.028*	35	*1.2*	2.218	*0.0024*	1.10	*0.039*	47	*4.7*
	8236 (2)	1.436	*0.0075*	1.12	*0.031*	25	*1.3*	1.925	*0.0016*	0.87	*0.026*	37	*1.2*	2.218	*0.0024*	1.09	*0.039*	38	*4.9*
	8236 (3)	1.429	*0.0073*	0.89	*0.035*	18	*1.4*	1.924	*0.0016*	0.87	*0.026*	39	*1.3*	2.210	*0.0024*	1.18	*0.042*	43	*4.7*
	8236 (4)	1.427	*0.0073*	1.08	*0.029*	20	*1.3*	1.918	*0.0020*	0.81	*0.027*	34	*1.2*	2.213	*0.0023*	1.17	*0.041*	46	*4.7*
	8236 (5)	1.383	*0.0092*	1.06	*0.029*	24	*1.3*	n.c	*n.c*	n.c	*n.c*	n.c	*n.c*	2.204	*0.0027*	0.87	*0.049*	76	*6.0*
	8236 (6)	1.444	*0.0078*	1.05	*0.029*	26	*1.4*	1.930	*0.0018*	0.97	*0.031*	31	*1.4*	2.223	*0.0026*	1.05	*0.039*	43	*4.7*
Nili Patera	10628 (1)	1.403	*0.0024*	0.35	*0.180*	14	*0.1*	1.918	*0.0020*	0.49	*0.082*	20	*2.3*	2.212	*0.0041*	1.13	*0.058*	66	*4.9*
	10628 (2)	n.c	*n.c*	n.c	*n.c*	n.c	*n.c*	n.c	*n.c*	n.c	*n.c*	n.c	*n.c*	2.210	*0.0042*	1.26	*0.067*	n.c	*n.c*
	10628 (3)	1.396	*0.0024*	0.89	*0.180*	14	*0.1*	1.914	*0.0017*	0.37	*0.073*	12	*2.1*	2.232	*0.0047*	1.07	*0.058*	75	*4.2*
	10628 (4)	n.c	*n.c*	n.c	*n.c*	n.c	*n.c*	1.910	*0.0020*	0.14	*0.087*	14	*1.9*	2.221	*0.0039*	0.90	*0.069*	86	*5.0*
	4185 (1)	n.c	*n.c*	n.c	*n.c*	n.c	*n.c*	1.911	*0.0018*	0.33	*0.167*	16	*7.7*	2.223	*0.0020*	0.97	*0.028*	84	*7.7*
	4185 (2)	n.c	*n.c*	n.c	*n.c*	n.c	*n.c*	1.917	*0.0018*	0.83	*0.167*	39	*7.7*	2.222	*0.0020*	0.91	*0.026*	61	*7.7*
	4185 (3)	n.c	*n.c*	n.c	*n.c*	n.c	*n.c*	n.c	*n.c*	n.c	*n.c*	n.c	*n.c*	2.212	*0.0023*	0.97	*0.028*	n.c	*n.c*
	82EE (1)	n.c	*n.c*	n.c	*n.c*	n.c	*n.c*	1.914	*n.c*	0.24	*n.c*	13	*n.c*	2.214	*0.0007*	0.95	*0.019*	87	*n.c*
	82EE (2)	n.c	*n.c*	n.c	*n.c*	n.c	*n.c*	n.c	*n.c*	n.c	*n.c*	n.c	*n.c*	2.217	*0.0008*	0.85	*0.022*	n.c	*n.c*
	82EE (3)	n.c	*n.c*	n.c	*n.c*	n.c	*n.c*	n.c	*n.c*	n.c	*n.c*	n.c	*n.c*	2.215	*0.0007*	0.93	*0.017*	n.c	*n.c*
	82EE (4)	n.c	*n.c*	n.c	*n.c*	n.c	*n.c*	n.c	*n.c*	n.c	*n.c*	n.c	*n.c*	2.214	*0.0007*	0.93	*0.017*	n.c	*n.c*
Noctis Labyrinthus	96EE (1)	1.395	*0.0031*	0.41	*0.066*	17	*0.7*	1.909	*0.0009*	0.54	*0.042*	27	*2.3*	2.211	*0.0018*	0.89	*0.042*	56	*6.0*
	96EE (2)	1.389	*0.0032*	0.35	*0.067*	15	*0.7*	1.915	*0.0010*	0.71	*0.035*	30	*2.1*	2.210	*0.0018*	0.88	*0.042*	55	*6.0*
	96EE (3)	1.407	*0.0035*	0.60	*0.069*	18	*0.7*	1.912	*0.0008*	0.70	*0.035*	38	*2.2*	2.209	*0.0018*	0.77	*0.046*	44	*6.3*
	96EE (4)	1.396	*0.0031*	0.54	*0.067*	20	*0.8*	1.911	*0.0008*	0.65	*0.035*	30	*2.1*	2.204	*0.0019*	0.91	*0.042*	50	*6.1*
	96EE (5)	1.406	*0.0034*	0.70	*0.074*	17	*0.7*	1.910	*0.0008*	0.80	*0.040*	40	*2.3*	2.204	*0.0020*	0.77	*0.046*	43	*6.3*
	96EE (6)	1.384	*0.0034*	0.09	*0.079*	15	*0.7*	n.c	*n.c*	n.c	*n.c*	n.c	*n.c*	2.217	*0.0020*	0.96	*0.043*	85	*6.8*
	96EE (7)	1.385	*0.0034*	0.34	*0.067*	14	*0.7*	n.c	*n.c*	n.c	*n.c*	n.c	*n.c*	2.217	*0.0020*	1.15	*0.052*	86	*6.8*
	7E28 (1)	1.385	*0.0024*	0.36	*0.049*	16	*1.2*	1.906	*0.0021*	0.59	*0.036*	23	*1.4*	2.206	*0.0010*	0.91	*0.021*	62	*2.5*
	7E28 (2)	1.380	*0.0026*	0.40	*0.046*	15	*1.3*	1.909	*0.0018*	0.67	*0.031*	23	*1.3*	2.206	*0.0011*	0.91	*0.021*	62	*2.6*
	7E28 (3)	1.383	*0.0025*	0.58	*0.048*	21	*1.4*	1.916	*0.0020*	0.78	*0.036*	29	*1.4*	2.208	*0.0010*	0.84	*0.020*	50	*2.8*
	7E28 (4)	1.394	*0.0030*	0.56	*0.046*	17	*1.1*	1.914	*0.0018*	0.70	*0.031*	27	*1.3*	2.211	*0.0012*	0.81	*0.023*	55	*2.4*
Iani Chaos	134D2 (1)	1.418	*0.0015*	0.91	*0.063*	23	*1.5*	1.921	*0.0013*	0.80	*0.025*	29	*2.5*	2.221	*0.0036*	1.25	*0.048*	48	*2.2*

134D2 (2)	1.424	*0.0019*	1.13	*0.069*	22	*1.5*	1.924	*0.0014*	0.73	*0.020*	42	*2.5*	2.225	*0.0039*	1.00	*0.050*	36	*2.5*
134D2 (3)	1.415	*0.0017*	0.78	*0.072*	16	*1.8*	1.924	*0.0014*	0.70	*0.021*	37	*2.2*	2.212	*0.0035*	1.11	*0.042*	47	*2.1*
134D2 (4)	1.418	*0.0015*	1.07	*0.064*	25	*1.6*	1.917	*0.0016*	0.68	*0.022*	32	*2.2*	2.205	*0.0041*	1.19	*0.043*	43	*2.0*

n.c = not calculated (absorption embed in the spectral noise or at the same order of magnitude as the spectral noise for example)

σ = SEM for Standard Error

For the following spectra, several spectels in the 2.2 µm absorption band were subject to spectral artifacts. These spectels were deleted and then re-interpolated using spline-cubic interpolation on several points:

[a] for this spectrum (Aeolis Mensae, FRT_86B7, first spectrum), seven spectels were deleted (at 2.1855, 2.1922, 2.1988, 2.2054, 2.2120, 2.2186 and 2.2252 µm) and were re-interpolated on the Origin software using a spline-cubic interpolation on seven points.

[b] for this spectrum (Aeolis Mensae, FRT_86B7, second spectrum), six spectels were deleted (at 2.1855, 2.1922, 2.1988, 2.2054, 2.2120 and 2.2186 µm) and were re-interpolated on the Origin software using a spline-cubic interpolation on six points.

[c] for this spectrum (Aeolis Mensae, FRT_86B7, third spectrum), five spectels were deleted (at 2.1922, 2.1988, 2.2054, 2.2120 and 2.2186 µm) and were re-interpolated on the Origin software using a spline-cubic interpolation on five points.

[d] for this spectrum (Nilosyrtis Mensae, FRT_D452, first spectrum), five spectels were deleted (at 2.1922, 2.1988, 2.2054, 2.2120 and 2.2186 µm) and were re-interpolated on the Origin software using a spline-cubic interpolation on five points.

Highlights

- Geological origin of hydrated silica on Mars is investigated.
- Spectral criteria developed on terrestrial silica minerals are applied to CRISM data.
- CRISM spectral results are consistent with the geomorphologic distinction between hydrated silica-bearing bedrock and aeolian deposits
- Discrimination between weathering and hydrothermal processes on Mars is discussed.